

## ABSTRACT

LI, SHULI. Preparation and Integration of Composite Nanofiber Anodes in Advanced Lithium-Ion Batteries. (Under the direction of Dr.Xiangwu Zhang).

Lithium-ion batteries are receiving considerable attention for use in portable electronics, electric vehicles and large-scale smart grids due to their superior energy storage capability over other rechargeable batteries. To achieve super-high energy density, advanced electrode materials with high energy storage capacities must be developed to replace traditional  $\text{LiCoO}_2$  cathode and graphite anode materials. For cathode materials, lithium metal oxides with a layered structure or a spinel structure, polyanion-based compounds and special organic materials have been investigated and reported in the past few years. They show inherent advantages of good structure stability, low cost, and high rate capability, etc. For anode materials, carbonaceous materials, lithium alloys and transition metal oxides are among the most promising alternatives and dominate current research. They show intriguing advantages of good environment compatibility, large specific capacities, and high safety, etc. Anode materials with capacities far beyond that of graphite are recently studied in order to satisfy the continuous demands for lithium-ion batteries that power advanced electronic devices. Among various types of anode materials with different elements and structures, carbon nanofiberous materials with controllable surface areas have attracted significant attention in recent years and are considered to be promising candidates for high-performance electrode materials. Carbon nanofibers can be produced by many techniques, among which electrospinning is a particularly efficient, simple and inexpensive method. In this work, we focused on fabricating various nanoparticle-loaded carbon nanofiber composite anodes and explore their potential applications as anode materials for advanced lithium-ion batteries.

These alternative anode materials were prepared by carbonizing electrospun metal salt- or nanoparticle-filled polymer nanofibers. The prepared composite nanofibers combine the properties of both metal or metal oxide nanoparticles (large Li storage capability) and carbon matrices (long cycle life), and can be used in practical rechargeable lithium-ion battery applications.

© Copyright 2012 by Shuli Li

All Rights Reserved

Preparation and Integration of Composite Nanofiber Anodes in Advanced Lithium-ion  
Batteries

by  
Shuli Li

A dissertation submitted to the Graduate Faculty of  
North Carolina State University  
in partial fulfillment of the  
requirements for the degree of  
Doctor of Philosophy

Fiber and Polymer Science

Raleigh, North Carolina

2013

APPROVED BY:

---

Dr. Xiangwu Zhang  
Committee Chair

---

Dr. Philip Bradford

---

Dr. Subhashish Bhattacharya

---

Dr. Wendy E. Krause

## **DEDICATION**

*To my beloved mother, father and all my family members,  
without whose love, guidance and support, this would not have been possible.*

*I appreciate to have you all in my life.*

## **BIOGRAPHY**

Shuli Li was born on June 22<sup>th</sup>, 1986 in Anshan, Liaoning, P. R. China. She completed her high school education in Anshan No.1 High School, and then attended Donghua University in September 2003, and graduated with a bachelor's degree in Textile International Trade in July 2007.

After graduation, she worked in Anshan Huangfang Textile Mill in Anshan, where she did one year of fieldwork on antistatic fibers for military industry. During that time, she participated in the new processing design of the antistatic fibers.

In August 2008, Shuli Li came to the U.S. and started working toward her Ph.D. degree majoring in Fiber and Polymer Science in the Department of Textile Engineering, Chemistry and Science at North Carolina State University. Her research activities ranged from the preparation and characterization of nanostructured carbon or carbon-composite materials and their application in energy conversion and storage systems, to the fabrication and functionalization of polymer or polymer composite materials for specific utilization.

## ACKNOWLEDGMENTS

The author would like to offer her sincerest appreciation to respected advisor: Professor Xiangwu Zhang, for supervising, supporting, and helping her grow during her Ph.D. studies; to her other committee members: Professors Subhashish Bhattacharya, Philip Bradford and Wendy E. Krause, for their wise counsel, advice, and support; and also to the Graduate School representative Professor Subhashish Bhattacharya, for his encouragement and communication.

The author also acknowledges funding supports from the FREEDM Center.

Moreover, the author would like to thank Dr. Liwen Ji, Dr. Zhan Lin, Dr. Mataz Alcoutlabi, Dr. Quan Shi, Dr. Kyung-Hye Jung, Dr. Bingkun Guo, Dr. Yingfang Yao, Dr. Narendiran Vitchuli, Dr. Ozan Toprakci, Dr. Hun Lee, Dr. Yinzheng Liang, Dr. Lan Zhou, Dr. Shu Zhang, Mr. Kun Fu, Mr. Guanjie Xu, Mr. Yao Lu, Mr. Chen Chen, Mr. Han Jiang, Mr. Liangqu Chen, Ms. Ying Li, Ms. Xin Xia, Ms. Xin Wang, Ms. Meltem Yanilmaz, Ms. Ying Ji and Ms. Shaghayegh Faraji at North Carolina State University for their earnest cooperation and warmhearted help during her Ph.D. study.

The author also deeply appreciates Mr. Chuck Mooney, Mr. Roberto Garcia and Dr. Ryan White in Analytical Instrumentation Facility for their help in sample characterization.

## TABLE OF CONTENTS

<b>LIST OF FIGURES</b> .....	ix
<b>CHAPTER 1 INTRODUCTION</b> .....	1
1. Lithium-ion battery .....	1
1.1 Applications.....	1
1.2 Advantages .....	3
1.3 Limitations.....	5
1.4 Working principle.....	5
1.5 Cathode materials .....	7
1.6 Anode materials.....	14
1.7 Electrolytes .....	44
2. Electrospinning technology .....	45
2.1 Working principle.....	46
2.2 Applications.....	48
2.3 Polyacrylonitrile as a precursor to carbon fibers .....	49
<b>CHAPTER 2 OBJECTIVES</b> .....	53
1. High-performance Sn/Carbon Composite Anodes Derived from Sn(II) Acetate/Polyacrylonitrile Precursor by Electrospinning.....	53

2. Comparison of Si/Carbon, Ge/Carbon and Sn/Carbon Composite Nanofiber Anodes used in New-generation Lithium-ion Batteries.....	54
3. Co <sub>3</sub> O <sub>4</sub> /Carbon Composite Nanofibers for Use as Anode Material in Advanced Lithium-ion Batteries.....	54
4. Nanosized Ge@C@CNF and Ge@CNF@C composites via CVD method for use in advanced lithium-ion batteries.....	55
CHAPTER 3 OVERALL EXPERIMENTAL SECTION .....	56
1. Chemicals.....	56
2. Nanofiber preparations.....	56
3. Nanofiber characterizations .....	57
4. Electrochemical evaluations .....	58
CHAPTER 4 HIGH-PERFORMANCE TIN/CARBON COMPOSITE ANODES DERIVED FROM TIN(II) ACETATE/POLYACRYLONITRILE PRECURSORS BY ELECTROSPINNING TECHNOLOGY.....	60
1. Introduction.....	61
2. Experimental.....	62
3. Results and discussion .....	63
3.1 Morphology .....	63
3.2 Electrochemical performance.....	70

4. Conclusion .....	75
CHAPTER 5 COMPARISON OF SILICON/CARBON, GERMANIUM/CARBON AND TIN/CARBON COMPOSITE NANOFIBER ANODES USED IN NEW-GENERATION LITHIUM-ION BATTERIES.....	
	77
1. Introduction.....	78
2. Experimental .....	80
3. Results and discussion .....	81
3.1 Morphology .....	81
3.2 Electrochemical performance .....	90
4. Conclusion .....	98
CHAPTER 6 COBALT OXIDE/CARBON COMPOSITE NANOFIBERS FOR USE AS ANODE MATERIAL IN ADVANCED LITHIUM-ION BATTERIES .....	
	99
1. Introduction.....	100
2. Experimental .....	101
3. Results and discussion .....	102
3.1 Morphology .....	102
3.2 Electrochemical performance .....	108
4. Conclusion .....	113

CHAPTER 7 NANOSIZED Ge@CNF, Ge@C@CNF AND Ge@CNF@C COMPOSITES VIA CVD METHOD FOR USE IN ADVANCED LITHIUM-ION BATTERIES .....	115
1. Introduction.....	117
2. Experimental .....	119
3. Results and discussion .....	121
3.1 Morphology .....	121
3.2 Electrochemical performance .....	129
4. Conclusion .....	135
CHAPTER 8 CONCLUSIONS .....	137
CHAPTER 9 RECOMMENDATION WORK.....	141
1. Carry out Cyclic Voltammetry (CV) measurements to identify the microstructure changes and the reactions on the electrode surfaces. ....	141
2. Prepare Ge <sub>x</sub> Sn <sub>1-x</sub> /C anodes and evaluate their electrochemical performance in lithium- ion batteries. ....	142
3. Prepare Si@SiO <sub>2</sub> /C anodes and evaluate their electrochemical performance in lithium- ion batteries. ....	142
REFERENCES .....	144

## LIST OF FIGURES

Figure 1.1. Representative applications for rechargeable batteries. ....	3
Figure 1.2. Comparison of the different battery technologies in terms of volumetric and gravimetric energy density.....	4
Figure 1.3. Illustration of a lithium-ion battery in a charging process with graphite as the anode and $\text{Li}_y\text{MO}_2$ as the cathode (M=metal). SEI is the abbreviation for Solid-Electrolyte-Interphase.....	7
Figure 1.4. Structure of layered lithiated transition metal oxides, $\text{LiMO}_2$ (M = Ni, Co, Mn)..	9
Figure 1.5. Structure of the spinel $\text{LiMn}_2\text{O}_4$ .....	10
Figure 1.6. Structure of olivine $\text{LiFePO}_4$ .....	13
Figure 1.7. Molecular structure, X-ray diffraction (XRD) pattern, and scanning electron microscope (SEM) image of organic cathode material $\text{Li}_4\text{C}_6\text{O}_6$ . ....	14
Figure 1.8. Schematic of lithium intercalation in graphite: (A) Lithium is inserted in every the second carbon hexagon and (B) between the graphite layers. ....	16
Figure 1.9. a) SEM image of SiNPs. b) HRTEM image of SiNWs. A layer of $\text{SiO}_x$ covers the surface of the SiNWs. c) Discharge/charging curves of SiNPs (weight ratio of SiNPs/carbon black = 1: 1) and SiNWs (no conductive additive).....	18
Figure 1.10. (a) SEM and (b) TEM images of Si/carbon composite nanofibers, (c) Galvanostatic charge-discharge curves, and (d) cycling performance of Si/carbon nanofibers. ....	20
Figure 1.11. (a) SEM images of the 3D porous C-Si particles after etching, (b) cross-sectioned image of (c), (c) TEM image of the cross-sectioned 3D porous c-Si particle (the	

inset shows a selected area diffraction pattern (SADP), and (d) charge capacities versus cycle number of the 3D porous c-Si particles cycled at different rates (0.2 C and 1 C) between 0 and 1.5 V in coin-type half cells. X=charge capacity, N=cycle number, Q=coulombic efficiency..... 21

Figure 1.12. a) TEM image of the Si@SiO<sub>x</sub>/C nanocomposites. Inset: TEM image at a higher magnification. b) High-resolution TEM image of the Si nanoparticles coated with SiO<sub>x</sub> and carbon. c) Galvanostatic discharge-charge curves of pure Si nanoparticles (I, II) and Si@SiO<sub>x</sub>/C nanocomposite (III, IV) electrodes cycled at a current density of 150 mA g<sup>-1</sup> between voltage limits of 0.05 - 1.0 V in VC-free (I, III) and VC-containing (II, IV) 1m LiPF<sub>6</sub> in EC/DMC solutions. .... 23

Figure 1.13. (a) Bright-field (Inset: the electron diffraction pattern), (b) dark-field TEM images of ballistically deposited germanium showing an agglomeration of nanocrystals, (c) bright-field (Inset: the electron diffraction pattern), (d) dark-field TEM images of evaporated germanium showing a uniform amorphous thin film, and (e) cycle life of germanium from ballistically deposited nanocrystals, an evaporated amorphous nanofilm, and the control sample of bulk crystalline germanium. The light and shaded markers represent the charge and discharge cycles, respectively..... 26

Figure 1.14. (a) SEM image of GeNWs with carbon coating, (b) TEM image of GeNWs with carbon coating, (c) voltage profiles of GeNW with carbon coating at the 0.5 C rate, and (d) cycle performance of uncoated and carbon sheathed GeNWs at a rate of 0.5 C between 0 and 1.5 V..... 28

Figure 1.15. SEM images of (a) GeNW, (b) PC-GeNW, (c) TEM image of PC-GeNW and (d) cycling performance of GeNW and PC-GeNW anodes..... 30

Figure 1.16. HR-TEM images of (a) Ge/C composite powders, (b) Ge/Cu<sub>3</sub>Ge/C composite powders, (c) XRD patterns of the Ge/Cu<sub>3</sub>Ge/C and Ge/C composite powders, and (d) the charge and discharge capacities as a function of cycle number for two electrodes. Current density = 100mA g<sup>-1</sup>, voltage cut-off range = 0.001 - 2.0 V. .... 32

Figure 1.17. (a and b) SEM images of Sn films: (a) coarse particles (2 - 4 μm), (b) fine particles (0.2 - 0.4 μm), (c) cycling performance of coarse Sn and fine Sn materials, (d-g) SEM images of the discharged Sn at different cycle numbers: (d and f) coarse Sn, (e and g) fine Sn particles..... 34

Figure 1.18. SEM images and diameter distribution of (A) as-received carbon nanofibers carbonized at 850 °C and Sn/C nanofibers carbonized at (B) 700, (C) 850, (D) 1000 °C, and (E) reversible capacities versus cycle numbers of as-received carbon nanofibers and Sn/C nanofibers carbonized at different temperatures..... 36

Figure 1.19. (a) TEM micrograph of the converted Sn encapsulated in multichannel carbon microtubes after heat treatment under an Ar/H<sub>2</sub> atmosphere. (b) HRTEM image confirming the porous multichannel walls. (c) HRTEM micrograph and SAED pattern of an isolated Sn nanoparticle, revealing the presence of single-crystalline metallic tin and amorphous carbon. (d) Cyclability of Sn particles encapsulated in porous multichannel carbon microtubes and commercial Sn nanopowder with similar sizes (~200 nm) at a cycling rate of 0.5 C (current density 100 mA g<sup>-1</sup>); the inset displays the discharge capacities of Sn particles encapsulated

in porous multichannel carbon microtube electrodes as a function of discharge rate at 2 and 10 C. All of the batteries were cycled in a voltage window of 5 mV to 2 V.....	38
Figure 1.20. (A) SEM image of $\text{Co}_3\text{O}_4$ microspheres calcined at 200 °C. (B) The initial three-cycle charge–discharge curves of $\text{Co}_3\text{O}_4$ electrode at a current density of 15 mA g <sup>-1</sup> between 0.01 and 3.0 V.....	41
Figure 1.21. a) SEM image and b) high-resolution TEM image of the carbon/cobalt oxide nanocomposite. c) Galvanostatic discharge/charge curves of carbon/cobalt oxide nanocomposite, and d) comparison of the cycling performance of the nanocomposite (OCMCs) and nanometer-sized $\text{Co}_3\text{O}_4$ electrodes.....	43
Figure 1.22. A) Schematic diagram showing a laboratory setup for electrospinning. B) Photograph of an electrospinning jet captured by a high-speed video showing the bending instability of the jet.....	47
Figure 1.23. Different electrospun fiber morphologies: (A) beaded, (B) ribbon, (C) porous, and (D) core-shell fibers. ....	48
Figure 1.24. Molecular structure of PAN. ....	50
Figure 1.25. Stabilized PAN structure.....	51
Figure 1.26. Structure changes for PAN precursor during carbonization.....	52
Figure 4.1. SEM images of (A) 6%, (B) 10%, (C) 20%, and (D) 30% Sn(II) acetate/PAN nanofibers.....	64
Figure 4.2. Nanofiber diameter distributions of (A) 6%, (B) 10%, (C) 20%, and (D) 30% Sn(II) acetate/PAN nanofibers.....	65

Figure 4.3. SEM images of Sn/C nanofibers derived from (A) 6%, (B) 10%, (C) 20%, and (D) 30% precursors. ....	66
Figure 4.4. Nanofiber diameter distributions of Sn/C nanofibers derived from (A) 6%, (B) 10%, (C) 20%, and (D) 30% precursors. ....	67
Figure 4.5. Dark Field TEM images of Sn/C composite nanofibers derived from 20% precursor. ....	68
Figure 4.6. XRD pattern of Sn/C composite nanofibers derived from 20% precursor.....	69
Figure 4.7. Galvanostatic charge-discharge curves of (A) the first cycle, (B) the second cycle and (C) twentieth cycle of Sn/C nanofiber anodes derived from 6%, 10%, 20%, and 30% precursors. Current density: 100 mA g <sup>-1</sup> . Carbonization temperature: 800 °C.....	72
Figure 4.8. Cycling performance of Sn/C nanofiber anodes derived from 6%, 10%, 20%, and 30% precursors. Current density: 100 mA g <sup>-1</sup> . Carbonization temperature: 800 °C. ....	74
Figure 4.9. Coulombic efficiencies of the first, second and twentieth cycles of Sn/C composite nanofiber anodes derived from 6%, 10%, 20%, and 30% precursors. ....	75
Figure 5.1. SEM images and fiber diameter distributions of (A, B) Si/C, (C, D) Ge/C, and (E, F) Sn/C nanofibers prepared from 10 wt% Si/PAN, Ge/PAN, and Sn/PAN precursors, respectively. ....	82
Figure 5.2. SEM images and fiber diameter distributions of (A, B) Si/C, (C, D) Ge/C, and (E, F) Sn/C nanofibers prepared from 30 wt% Si/PAN, Ge/PAN, and Sn/PAN precursors, respectively. ....	84

Figure 5.3. SEM images and fiber diameter distributions of (A, B) Si/C, (C, D) Ge/C, and (E, F) Sn/C nanofibers prepared from 50 wt% Si/PAN, Ge/PAN, and Sn/PAN precursors, respectively. ....	86
Figure 5.4. TEM images of (A) Si/C, (B) Ge/C, and (C) Sn/C nanofibers prepared from 30 wt% Si/PAN, Ge/PAN, and Sn/PAN precursors, respectively. ....	88
Figure 5.5. Raman spectra of Si/C, Ge/C, and Sn/C nanofibers prepared from 30 wt% precursors, respectively.....	89
Figure 5.6. Galvanostatic charge-discharge curves of the first, second and twentieth cycles of (A) Si/C, (B) Ge/C, and (C) Sn/C nanofibers prepared from 10 wt% precursors. ....	91
Figure 5.7. Galvanostatic charge-discharge curves of the first, second and twentieth cycles of (A) Si/C, (B) Ge/C, and (C) Sn/C nanofibers prepared from 30 wt% precursors. ....	93
Figure 5.8. Galvanostatic charge-discharge curves of the first, second and twentieth cycles of (A) Si/C, (B) Ge/C, and (C) Sn/C nanofibers prepared from 50 wt% precursors. ....	94
Figure 5.9. Coulombic efficiencies of Si/C, Ge/C, and Sn/C nanofiber anodes prepared from (A) 10, (B) 30, and (C) 50 wt% precursors.....	96
Figure 5.10. Cycling performance of Si/C, Ge/C, and Sn/C nanofiber anodes prepared from (A) 10, (B) 30, and (C) 50 wt% precursors.....	97
Figure 6.1. SEM images of Co <sub>3</sub> O <sub>4</sub> /C composite nanofibers. Co <sub>3</sub> O <sub>4</sub> particle size: (A,B) 10 - 30 nm, and (C,D) 30 - 50 nm. ....	103
Figure 6.2. TEM images of Co <sub>3</sub> O <sub>4</sub> /C composite nanofibers. Co <sub>3</sub> O <sub>4</sub> particle size: (A) 10 - 30 nm, and (B) 30 - 50 nm. ....	105

Figure 6.3. Fiber diameter distributions of Co <sub>3</sub> O <sub>4</sub> /C composite nanofibers. Co <sub>3</sub> O <sub>4</sub> particle size: (A) 10 - 30 nm, and (B) 30 - 50 nm.....	106
Figure 6.4. XRD pattern of Co <sub>3</sub> O <sub>4</sub> /C composite nanofibers. Co <sub>3</sub> O <sub>4</sub> particle size: 30 - 50 nm. ....	107
Figure 6.5. Galvanostatic charge-discharge curves of Co <sub>3</sub> O <sub>4</sub> /C composite nanofibers with different Co <sub>3</sub> O <sub>4</sub> particle sizes. (A) The first cycle, (B) the second cycle, and (C) the twentieth cycle. ....	110
Figure 6.6. Cycling performance of Co <sub>3</sub> O <sub>4</sub> /C composite nanofibers with different Co <sub>3</sub> O <sub>4</sub> particle sizes.....	112
Figure 6.7. Coulombic efficiencies of Co <sub>3</sub> O <sub>4</sub> /C composite nanofibers with different Co <sub>3</sub> O <sub>4</sub> particle sizes.....	113
Figure 7.1. Schematics illustrating the fabrication processes of (A) Ge@CNF, (B) Ge@C@CNF, and (C) Ge@CNF@C. ....	119
Figure 7.2. SEM images of (A) Ge@CNF, (B) Ge@C@CNF, and (C) Ge@CNF@C. ....	123
Figure 7.3. TEM images of (A) Ge@CNF, (B) Ge@C@CNF, and (C) Ge@CNF@C. ....	125
Figure 7.4. (A) High-resolution STEM image, (B) atomic resolution elemental map and (C) EDX spectrum of Ge@CNF@C. In the atomic resolution elemental map, Ge and carbon elements are colored with light green and red, respectively. ....	127
Figure 7.5. Raman spectra of Ge@C, Ge@CNF, Ge@C@CNF, and Ge@CNF@C. ....	128
Figure 7.6. Galvanostatic charge-discharge curves of the first, second and twentieth cycles of (A) Ge@CNF, (B) Ge@C@CNF, and (C) Ge@CNF@C. ....	131

Figure 7.7. Differential capacity plots of the first and second cycles of (A) Ge@CNF, (B) Ge@C@CNF, and (C) Ge@CNF@C. .... 133

Figure 7.8. Cycling performances of Ge@CNF, Ge@C@CNF, and Ge@CNF@C. .... 135

## CHAPTER 1 INTRODUCTION

### 1. Lithium-ion battery

The demand for renewable energy resources and reliable energy storage devices is growing rapidly to combat global warming, create a low carbon economy, replace the traditional fossil fuels, etc<sup>1, 2</sup>. Among all energy storage devices, rechargeable (or secondary) batteries such as lithium-ion, nickel-metal hydride (Ni-MH), lead acid, redox flow, and sodium–sulfur (Na-S) batteries are reversible and highly durable that can repeatedly store eco-friendly electricity and deliver stored chemical energy back into electrical energy<sup>2, 3</sup>. Particularly, rechargeable lithium-ion batteries prevail in various applications, such as laptops, digital cameras, and hybrid vehicles due to their lower environmental impact, high energy density, fast charging and stable cyclability. With further increasing energy densities, lithium-ion batteries will continue dominating the energy storage market<sup>4</sup>.

#### 1.1 Applications

Different design configurations (e.g., coin, cylindrical or prismatic shape and stack)<sup>4</sup> of rechargeable batteries have been developed for high-end consumer electronics. They are mainly classified into two categories: i) portable electronic consumer devices and electric vehicles, and ii) large-scale electricity storage in smart or intelligent grids (Figure 1.1). In the application of telecommunication, nearly 5 billion cellular phones are powered by rechargeable batteries till the end of 2009, and the number is increasing very rapidly in recent

years with the emerging 3-Generation (3G) and 4G technologies implemented in the electronics<sup>4</sup>. In the field of electric vehicles, it is reported that plug-in hybrid electric vehicles with high performance lithium-ion batteries can provide a specific energy of 200Wh kg<sup>-1</sup>, which is more than twice of that of Ni/MH batteries in 2000s<sup>5</sup>. With respect to the expanded use of rechargeable batteries, such as smart grids used in large-scale electricity generation from solar cells and wind power, the batteries will play an important role in improving the grid stability<sup>6</sup>.

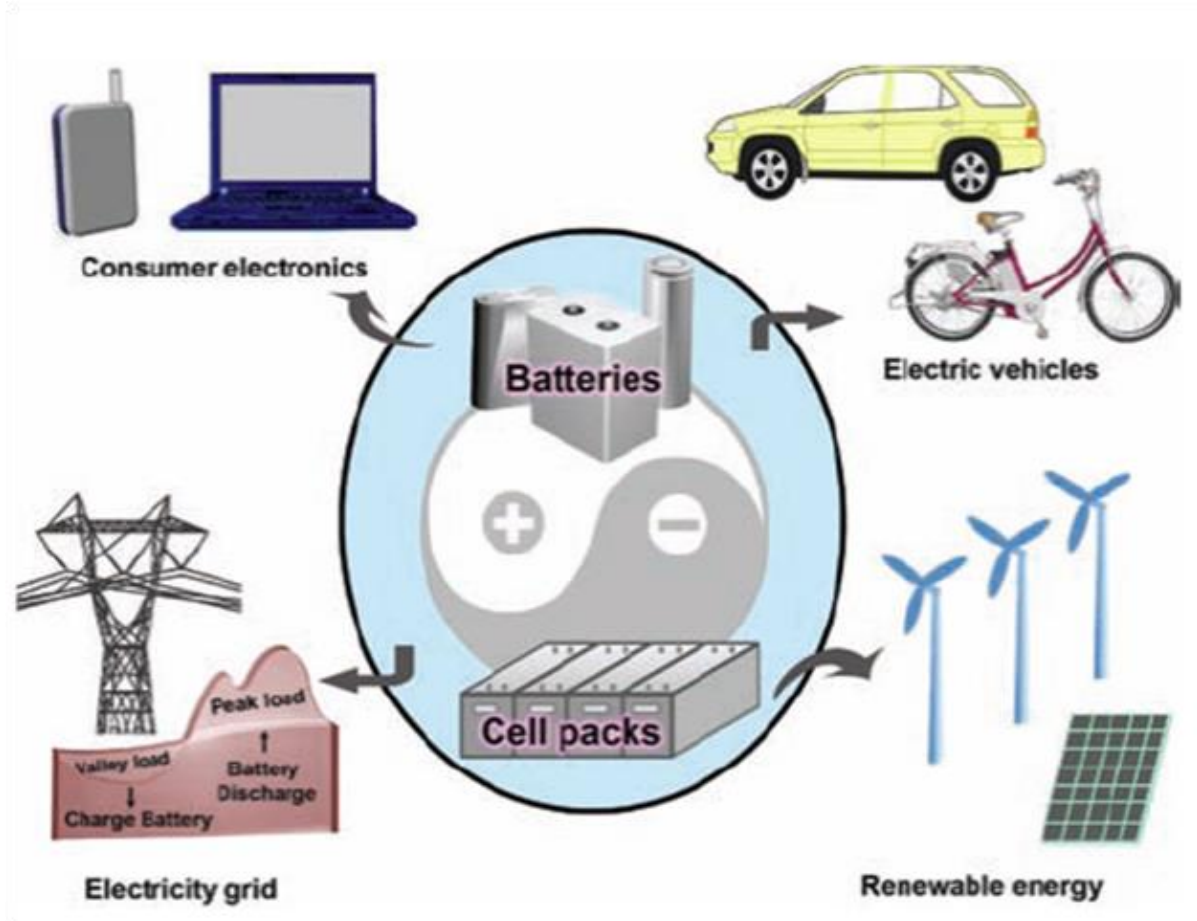


**Figure 1.1. Representative applications for rechargeable batteries<sup>4</sup>.**

## 1.2 Advantages

Lithium-ion batteries have long been considered as a dominant power source of electronic devices and smart grids based on many essential features<sup>7-9</sup>. As shown in Figure 1.2, first, lithium-ion batteries offer specific energy 2-4 times and power densities 2-3 times higher than Ni-Cd and lead acid batteries. Second, their life span and energy density are both twice as much as Ni-Cd batteries with half the weight and 30-50% smaller in volume. Third, lithium-ion batteries feature fast charging ability with an 80% charge in an hour, and full

charge within 2.5 hours. Fourth, lithium-ion batteries present environmental safety and eco-friendliness without the use of harmful metals (e.g. lead, cadmium or mercury). Last and most importantly, compared with other traditional rechargeable batteries, lithium-ion batteries have no memory effect, which refers to a change in crystalline formation from the desirable small size to a large size that leads to reversible capacity loss.

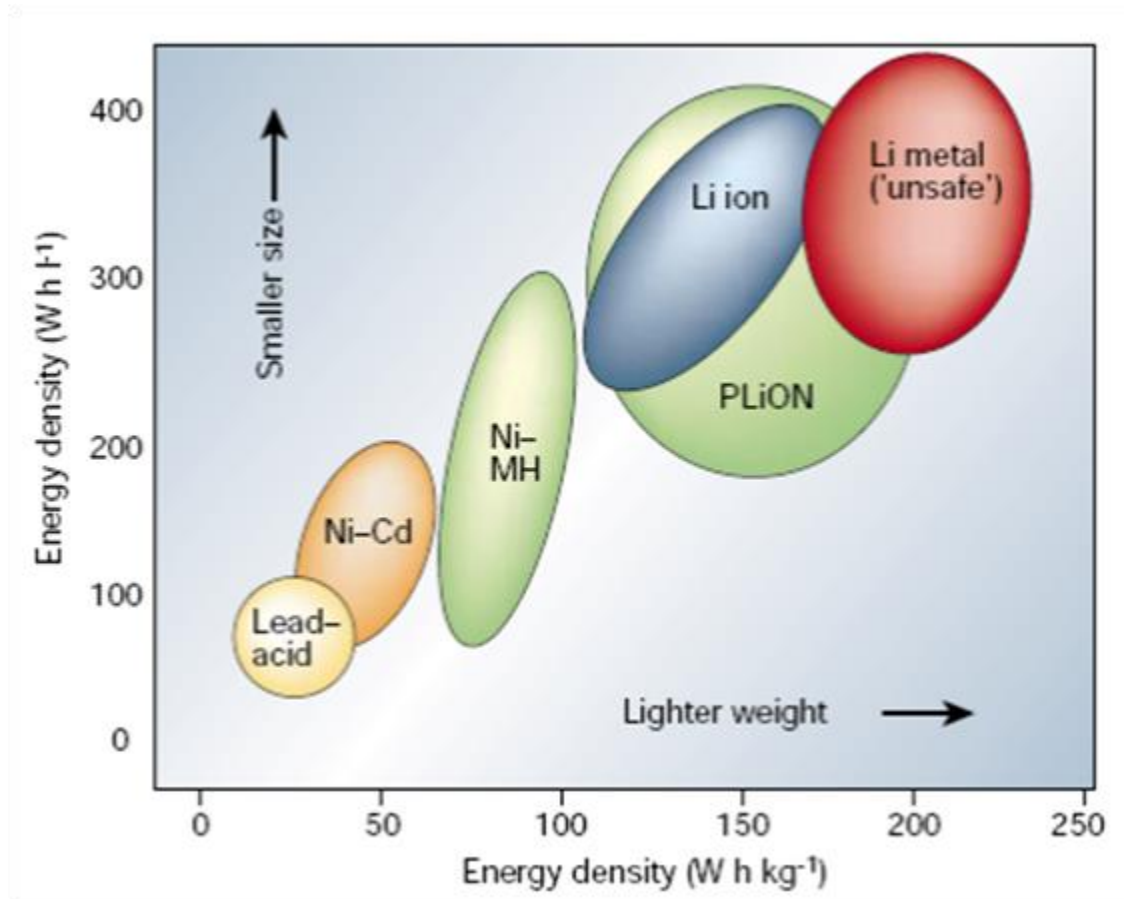


**Figure 1.2. Comparison of the different battery technologies in terms of volumetric and gravimetric energy density<sup>7</sup>.**

### 1.3 Limitations

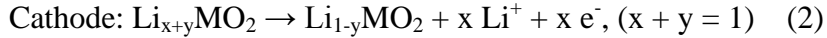
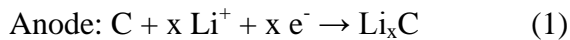
An ideal lithium-ion battery would have advantages of high energy densities, relatively low cost, environmental compatibility and safe operation potentials<sup>10</sup>. In contrast with the aforementioned applications, current lithium-ion batteries cannot fully satisfy all these requirements<sup>11</sup>. Most of the practical lithium-ion batteries deliver capacities and energy densities far below their theoretical values due to limited utilization of the active materials that participate in the electrochemical reactions<sup>4</sup>. This limitation is mainly due to slow electrode process kinetics with high polarization and a low rate of ionic diffusion or electronic conductivity. Thus, to improve the electrochemical performance of lithium-ion batteries, many researchers focused on the ionic diffusion and transport, electron transfer, the surface and interface structure optimization of the key materials for two electrodes.

To tackle these problems, many efforts have been made to improve the materials in each part of lithium-ion batteries (positive electrode, negative electrode and the electrolyte)<sup>12</sup>. For example, improvements sought in electrode materials have been focused on: i) larger capacity and higher energy density; ii) higher reversibility, and structural stability during charge-discharge cycles; iii) faster ionic diffusion and electronic transfer; iv) lower cost; and v) higher safety and more environmental friendliness.

### 1.4 Working principle

A lithium-ion battery consists of two electrodes, an anode as a negative electrode and a cathode as a positive electrode. They are capable of reversibly hosting Li ions during

charging and discharging process (Figure 1.3)<sup>13</sup>. The electrolyte is typically a lithium salt (e.g. LiPF<sub>6</sub>) dissolved in organic solvent (e.g. ethylene carbonate)<sup>14</sup>. It transfers the ions, but is an electronic insulator. A porous polymer membrane is used between the anode and the cathode material and separates them to avoid short circuit. When the cell is being charged, Li ions are extracted from the Li<sub>y</sub>MO<sub>2</sub> positive electrode and entered the carbon negative electrode. When the cell is being discharged, Li ions are reversibly extracted from the carbon electrode and inserted back into the positive electrode<sup>15</sup>. During the shifting, electrons flow oppositely to Li ions between the anode and the cathode through the outside circuit<sup>16</sup>. The electrochemical charging process is a solid-state redox reaction that can be briefly described as:



The discharging process is the reverse of these equations<sup>17</sup>.

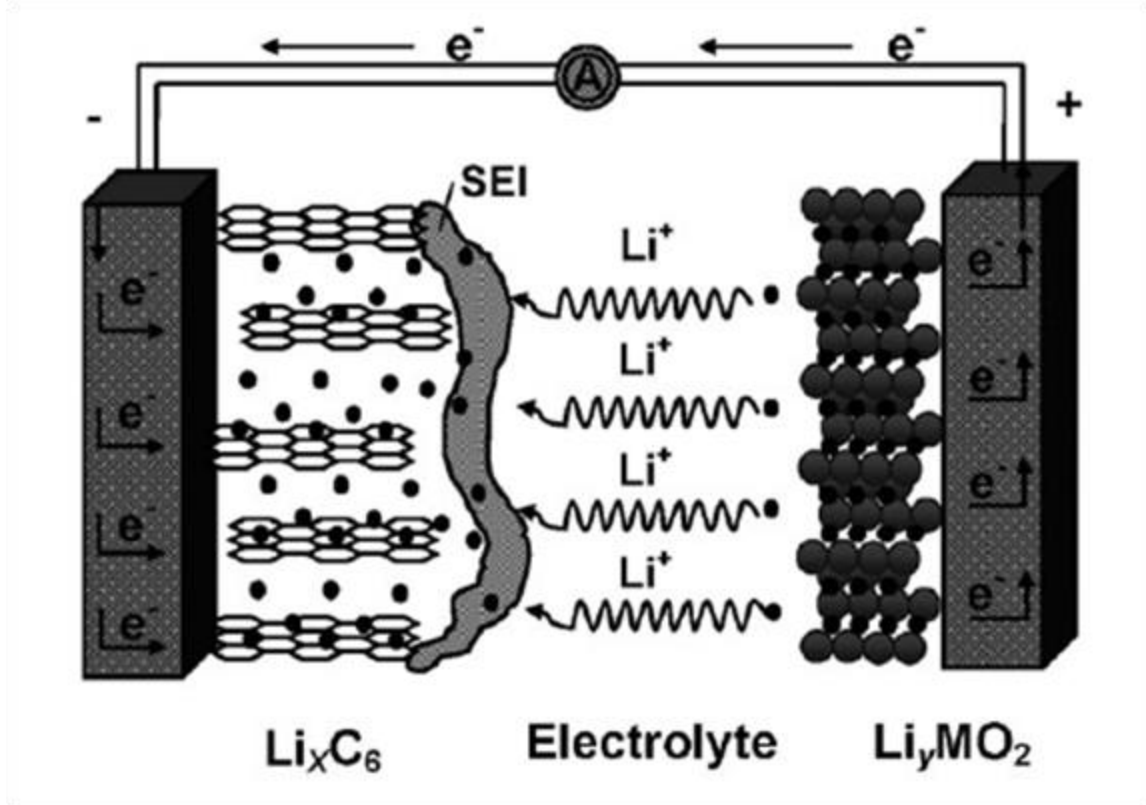


**Figure 1.3. Illustration of a lithium-ion battery in a charging process with graphite as the anode and  $\text{Li}_y\text{MO}_2$  as the cathode (M=metal). SEI is the abbreviation for Solid-Electrolyte-Interphase<sup>13</sup>.**

### 1.5 Cathode materials

To date, many developments in the area of positive electrode materials of lithium-ion batteries have been investigated and reported, and particularly in the past few years which include lithium metal oxides with a layered structure or a spinel structure, polyanion-based compounds and special organic materials for cathodes<sup>18, 19</sup>.

### 1.5.1 Lithium metal oxides

Currently, the most mature lithium-insertion cathode materials are lithium transition metal oxides, which can be classified into two major categories: 1)  $\text{LiMO}_2$  (M denotes a transition metal and is often Co, Mn, Ni, and their combinations, with a layered structure, and 2)  $\text{LiM}_2\text{O}_4$  with the spinel structure<sup>18</sup>.

#### 1.5.1.1 $\text{LiCoO}_2$ cathode

The classic  $\text{LiCoO}_2$  (in Figure 1.4) is the most successfully commercialized cathode since the first commercialization by Sony in 1991<sup>18</sup>. However, despite a high theoretical capacity of  $274 \text{ mAh g}^{-1}$ , its practical reversible capacity is limited to about half of this value due to the severe degradation of electrolyte decomposition and cathode degradation with a potential above 4.3 V. In addition, the reversible capacity of  $\text{LiCoO}_2$  cathode is also influenced strongly by the ordering of  $\text{Li}^+$  and  $\text{M}^{3+}$  ions in the lattice<sup>20</sup>. Efforts on improving  $\text{LiCoO}_2$  has involved structural aspects of the material and the optimisation of the synthesis process<sup>19</sup>. It is reported that doping with the trivalent ions (e.g., Al or Cr) and coating with the metal oxides or phosphates (e.g.,  $\text{ZrO}_2$ ,  $\text{Al}_2\text{O}_3$ ,  $\text{AlPO}_4$ , or  $\text{FePO}_4$ ) can improve the electrode performance of the  $\text{LiCoO}_2$  cathode<sup>21-24</sup>. Because of high cost, high toxicity and limited abundance of cobalt, alternative cathode materials such as  $\text{LiMnO}_2$ ,  $\text{LiNiO}_2$ ,  $\text{LiFeO}_2$  are fully or partially used<sup>4</sup>.

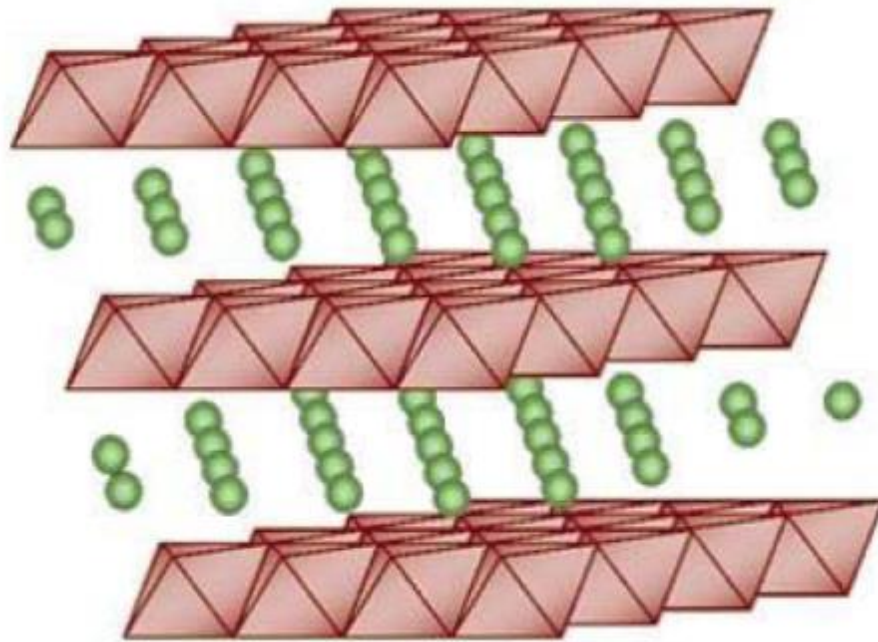


**Figure 1.4. Structure of layered lithiated transition metal oxides,  $\text{LiMO}_2$  ( $\text{M} = \text{Ni}, \text{Co}, \text{Mn}$ )<sup>25</sup>.**

#### 1.5.1.2 $\text{LiMn}_2\text{O}_4$ cathode

Owing to the high cost and toxicity of cobalt-based cathode ( $\text{LiCoO}_2$ ), and the difficulty in synthesizing phase-pure  $\text{LiMnO}_2$ ,  $\text{LiNiO}_2$  and  $\text{LiFeO}_2$  cathodes, the spinel  $\text{LiMn}_2\text{O}_4$  (Figure 1.5) is expected to supplant the currently commercialized  $\text{LiCoO}_2$  cathode. Unlike  $\text{LiCoO}_2$ ,  $\text{LiMn}_2\text{O}_4$  offers high thermal threshold, low cost, intrinsic rate capability, and environmental friendliness due to the chemically stable  $\text{Mn}^{3+}/\text{Mn}^{4+}$  couple and a 3D framework for facile  $\text{Li}^+$  mobility<sup>25, 26</sup>. However, gradual capacity loss occurs during Jahn–Teller distortion of  $\text{Mn}^{3+}$ , which transforms the cubic crystal symmetry of the spinel electrode into tetragonal

symmetry, and Mn dissolution in the electrolyte appears. One effective approach to mitigate this deleterious impact is to replace part of the manganese in  $\text{LiMn}_2\text{O}_4$  with mono- or multivalent cations (e.g.,  $\text{Li}^+$ ,  $\text{Mg}^{2+}$ , or  $\text{Zn}^{2+}$ ) or doping the oxide with additional oxygen to suppresses the Jahn-Teller effect on deep discharge<sup>27</sup>. One of the examples is substitution of  $\text{LiMn}_2\text{O}_4$  on an ordered  $\text{Li}_{1.12}\text{Mn}_{1.88}\text{O}_4$  demonstrated a 50% higher specific capacity than the bulk material at a current density of  $3000 \text{ mA g}^{-1}$ <sup>28</sup>. Another example is the substitution of the  $\text{Mn}^{3+}$  by other trivalent cations ( $\text{Al}^{3+}$ ,  $\text{Fe}^{3+}$ ,  $\text{Ni}^{3+}$ ,  $\text{Co}^{3+}$ , or  $\text{Cr}^{3+}$ )<sup>29-33</sup>. Furthermore, developing nanostructures, such as  $\text{LiMn}_2\text{O}_4$  nanorods and nanowires increases the reversible capacities as well<sup>34, 35</sup>. In a nanostructure, the switching between a cubic and tetragonal structure during lithium insertion and extraction are accommodated by the slippage at the domain wall boundaries<sup>36</sup>. The phase boundary energy changes with the particle size and thus changes the kinetics of Li reactions. It is reported that the electrochemical performance of  $\text{LiMn}_2\text{O}_4$  is improved by reducing the crystal nanoparticle size to 40 nm but decreased with the nanoparticle size reduced to below 15 nm<sup>37-39</sup>.

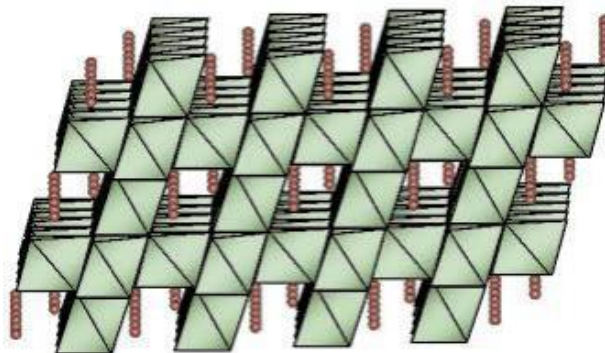


**Figure 1.5. Structure of the spinel  $\text{LiMn}_2\text{O}_4$ <sup>25</sup>.**

### 1.5.2 Polyanionic materials

Polyanion-based compounds,  $\text{Li}_x\text{M}_y(\text{XO}_4)_z$  ( $\text{M}$  = metal;  $\text{X}$  = P, S, Si, Mo, W, etc.), are now regarded as the most promising cathode materials for lithium-ion batteries. In this category, phospho-olivine  $\text{LiFePO}_4$  (Figure 1.6) has been the research focus since the pioneering work of Padhi<sup>40</sup>. It becomes the most intriguing cathode material because of its relatively high theoretical capacity ( $170 \text{ mAh g}^{-1}$ ), environmentally benign and abundant with stable cycleability and high safety<sup>41</sup>.

One great importance is the relatively stable potential of bulk  $\text{LiFePO}_4$ , which causes by the constant chemical potential difference between compositions close to  $\text{LiFePO}_4$  and  $\text{FePO}_4$ . Furthermore, it shows excellent cycle stability due to structural similarity between charged-discharged states<sup>42</sup>. However, ionic diffusion and electronic transport are vital issues for  $\text{LiFePO}_4$  cathode material and thus doping or coating  $\text{LiFePO}_4$  with an electronically or ionically conductive component becomes important. Kang *et al.*<sup>43</sup> and Delmas *et al.*<sup>44</sup> have shown that depositing lithium phosphate on the surface of  $\text{LiFePO}_4$  and applying large amount of carbon (65%) increase the conductivity of  $\text{LiFePO}_4$ , therefore greatly enhance the reversible capacity and rate cycleability of the composite structure. Moreover, making nanocomposite structure, such as  $\text{LiFePO}_4$ /carbon nanocomposite and  $\text{LiFePO}_4$  nanoparticles in a porous carbon matrix, has proven to be an efficient strategy because of the reduced distance for ionic and electronic transport. Generally, the behaviors of phase transition and

lithium transport within  $\text{LiFePO}_4$  and the compounds correlate correspondingly with the particle size, defects, morphologies, and crystallinity<sup>4, 45, 46</sup>.

In addition to,  $\text{LiFePO}_4$ , other olivine phases such as  $\text{LiCoPO}_4$  and  $\text{LiMnPO}_4$  have similar theoretical capacities and high voltages, but they also have poor capacity retention and sluggish kinetics due to their low intrinsic ionic and electronic conductivities<sup>47, 48</sup>. Substitution of other transition metals to form mixed-metal olivine compounds, such as  $\text{LiMn}_{0.8}\text{Fe}_{0.2}\text{PO}_4$ , offers the possibility to improve the rate capability while maintaining high voltages<sup>49</sup>. In addition, other attractive species in the polyanionic family including  $[\text{PO}_4\text{F}]^{4-}$ ,  $[\text{SO}_4\text{F}]^{3-}$  or  $[\text{SiO}_4]^{4-}$  delivers a high reversible capacity due to 2D pathways for Li ions transport with minimal structural changes on reduction/oxidation process<sup>50-54</sup>.  $\text{LiFeSO}_4\text{F}$  appears to be a competitive positive material capable of rivaling  $\text{LiFePO}_4$  by exhibiting better ionic and electronic conductivities<sup>51</sup>. Generally speaking, with the advantages of high capacity retention, environmentally friendliness and abundance,  $\text{LiFePO}_4$  is rapidly substituting commercialized  $\text{LiCoO}_2$  for practical application in lithium-ion batteries.

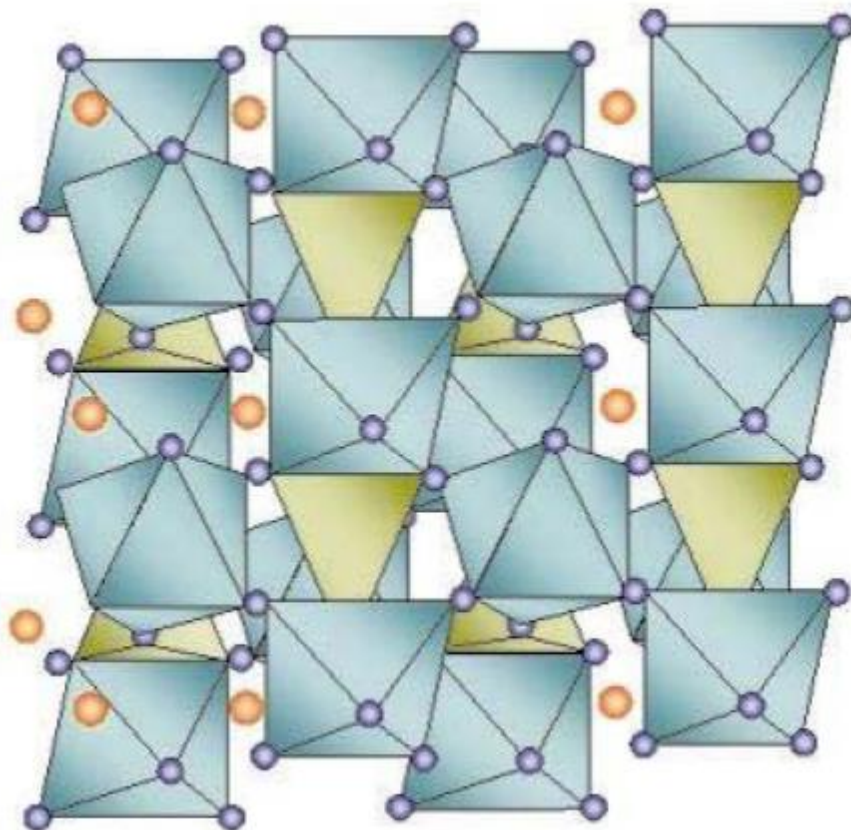


**Figure 1.6. Structure of olivine  $\text{LiFePO}_4$ <sup>25</sup>.**

### 1.5.3 Organic electrode materials

Particular attention is oriented nowadays to organic positive electrodes due to the ease of synthesis, low cost of production, and sustainability<sup>12, 55</sup>. Several types of polymer derivatives have been synthesized by Stura and co-workers<sup>12</sup>: poly(p-phenylenevinylene) (PPV), poly(2-methoxy-5-(2'-ethyl)hexyloxy-p-phenylenevinylene) (MEHPPV) and poly(ortho-anisidine) with titanium dioxide nanoparticles. These cathode materials show relatively good electrochemical performance and are thus suitable for lithium-ion batteries.

Cheng and Han<sup>56, 57</sup> demonstrated polyaniline and perylene-tetracarboxylicacid-dianhydride sulfide polymer as potential positive Li-insertion materials (Figure 1.7). Besides, a recent study by Chen and colleagues has shown that oxocarbon is another promising candidate of cathode material because of its high reversible capacity of 200 mAh g<sup>-1</sup> during the reduction and oxidation process. Since the operating voltage is too low to be practical, further chemical modification is still required<sup>4</sup>.

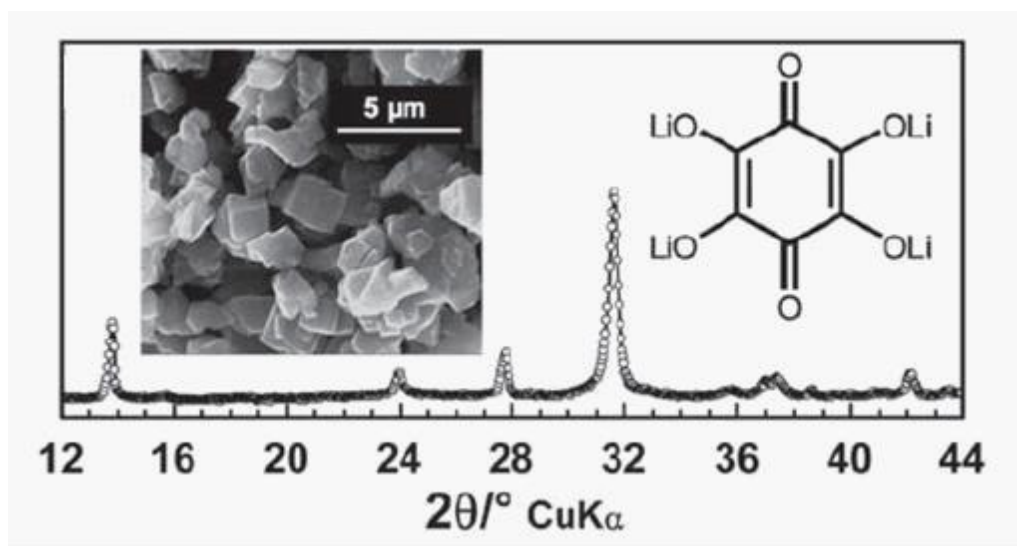


**Figure 1.7. Molecular structure, X-ray diffraction (XRD) pattern, and scanning electron microscope (SEM) image of organic cathode material  $\text{Li}_4\text{C}_6\text{O}_6$ <sup>4</sup>.**

## 1.6 Anode materials

Metallic lithium is an excellent anode material in terms of high energy density and it has been widely applied in primary cells. However, it may cause an internal short circuit and thus

lead to serious safety problems. Currently, almost all commercial lithium-ion batteries use graphite as the anode material. Carbonaceous materials, lithium alloys and transition metal oxides are among the most promising alternatives for the anode and dominate current researches on the anode materials. Because of the advantages of large charge-discharge capacities, favorable cyclic stability, fast response, low cost and high safety compared to metallic lithium, they will continue the dominance in rechargeable lithium-ion batteries. The emphasis is placed herein on three common types of anode materials that deliver high capacities and energy densities with low cost and good safety<sup>4</sup>.

### 1.6.1 Graphite

Commercial lithium-ion batteries have employed graphite as the anode material since the first manufacture of artificial graphite by E.G. Acheson at the end of the nineteenth century<sup>58</sup>. Graphite is characterized as a stack of hexagonally bonded sheets of carbon held together by van der Waals forces and can insert only 1 lithium for every 6 carbon atoms (Figure 1.8). Lithium can be inserted between the planes of graphite on the basis of the disparity of forces between two carbons in the same sheet or two adjacent sheets. Lithium ions can only combine on every second carbon hexagon in the graphite sheet due to the repulsion of lithium ions thus limiting the amount of lithium ions to 1 for every 6 carbon atoms. This directly determines the theoretical capacity of graphite during charging and discharging and provides a theoretical capacity of 372 mAh g<sup>-1</sup>. Graphite is widely used in commercial lithium-ion batteries because of their low potential, high capacity retention, low cost and high safety<sup>14</sup>.

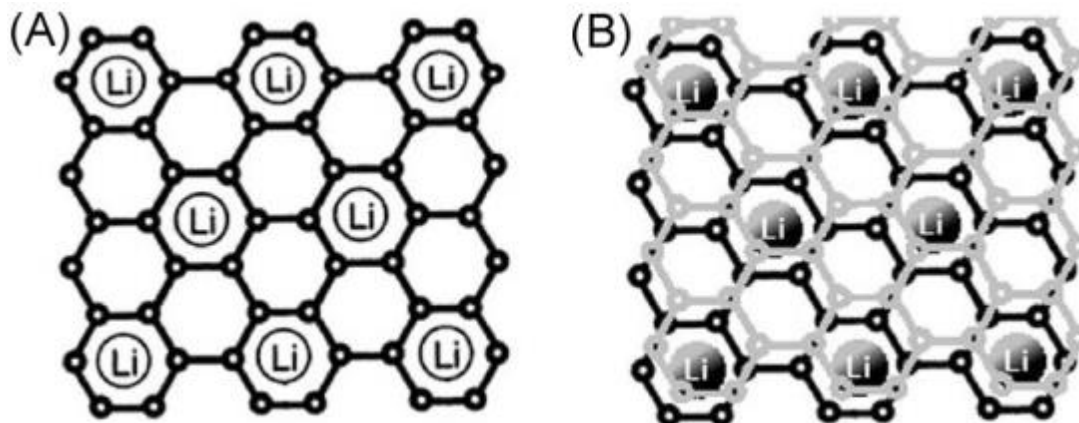


**Figure 1.8. Schematic of lithium intercalation in graphite: (A) Lithium is inserted in every the second carbon hexagon and (B) between the graphite layers<sup>14</sup>.**

### 1.6.2 Lithium alloys

Lithium alloys, Li-M (M = Si, Ge, Sn, Al, Bi, Zn, and Sb, etc) is another commonly used cathode material<sup>59, 60</sup>. The fact that M elements can reversibly react with large amounts of Li per formula unit provides the high capacity of lithium alloy materials. For example, Si, Ge and Sn generate lithium alloys  $\text{Li}_{4.4}\text{M}$  with theoretical specific capacities as high as 4200, 1600 and 993 mAh  $\text{g}^{-1}$ , respectively<sup>61</sup>. Unfortunately, dramatic volume expansion and contraction occurs during Li insertion and extraction and this is the major problem for using alloy-based materials. This leads to the pulverization of the electrode materials and poor cyclic performance<sup>62-64</sup>. Several strategies have been investigated to overcome these obstacles, such as using nanoscale materials or dispersing the active component in a rigid matrix to form composite structures<sup>1, 65</sup>. Carbon is reported to be a promising coating

material or matrix to disperse M elements and provides improved electrochemical performance<sup>10, 66-70</sup>. In the composite structure, the carbon matrix acts not only as a buffer for the volume change, but also improves the electric conductivity and ionic conductivity of the anode. In addition, because carbon is an electrochemical active material and has considerable Li-storage capacity, it has the advantages of suppressing the formation of SEI film and providing additional capacity<sup>1, 66-68</sup>.

#### 1.6.2.1 Si and Si/C nanocomposites

Si has been considered as one of the most attractive anode materials for lithium-ion batteries because it provides the highest gravimetric and volumetric capacity. Si has the ability to store large amounts of Li with a theoretical capacity of  $4200 \text{ mAhg}^{-1}$  by the formation of  $\text{Li}_{4.4}\text{Si}$  alloy with advantages of abundance, low cost, and environmental friendliness<sup>70</sup>. Li *et al.*<sup>64</sup> investigated the morphology and electrochemical performance of silicon nanoparticles (SiNPs) and silicon nanowires (SiNWs) by SEM (Figure 1.9(a)), TEM (Figure 1.9(b)) and cell testing techniques (Figure 1.9(c)). SiNPs and SiNWs were prepared with carbon black as the conductive additive and showed reversible capacities of  $1700$  and  $900 \text{ mAh g}^{-1}$ , respectively. It was found that carbon black played an important role to improve the capacity retention by increasing the electronic contact between the active particles. However, the same strategy was not effective for micrometer-sized Si particles because the occurrence of serious pulverization in these Si electrodes<sup>64, 71</sup>. Though SiNP showed a significant advantage in capacity retention, it appeared to agglomerate after one cycle thus causing low cyclic stability. Nanosized materials have a high surface energy and tend to aggregate. During electrochemical lithiation, particles expand and contact with each other, and very dense

agglomerates are formed after electrochemical cycling. This phenomenon is called ‘electrochemical agglomeration’, which has been observed in most of the alloy anodes<sup>71</sup>.

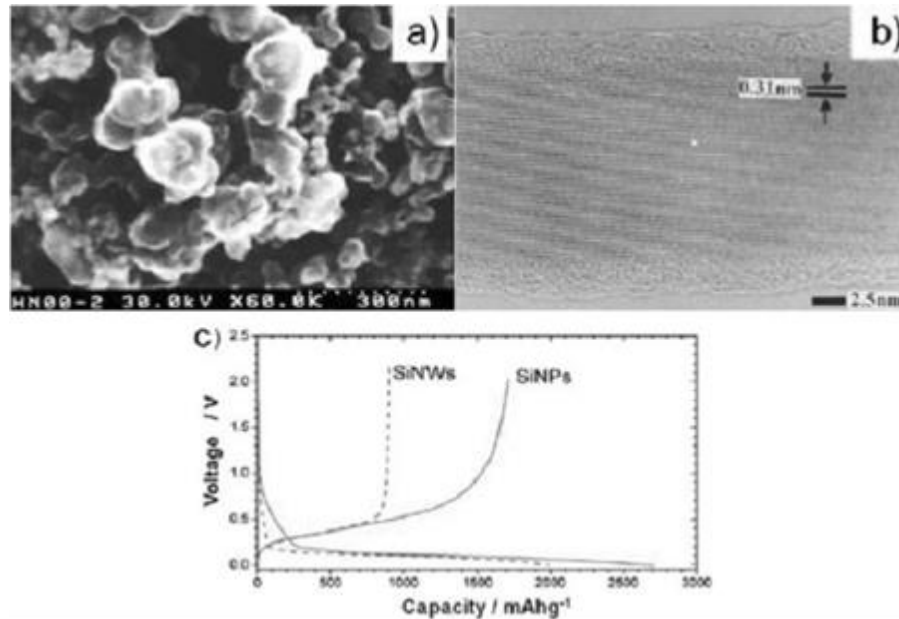


**Figure 1.9. a) SEM image of SiNPs. b) HRTEM image of SiNWs. A layer of SiO<sub>x</sub> covers the surface of the SiNWs. c) Discharge/charging curves of SiNPs (weight ratio of SiNPs/carbon black = 1: 1) and SiNWs (no conductive additive)<sup>64</sup>.**

Carbon matrix has been very attractive based on its buffering and constraining ability. It has been applied by many research groups to accommodate the large volume change and nanoparticle agglomeration. For example, Ji and Zhang<sup>1, 72-74</sup> have reported the preparation and cyclic profiles of Si/C composite nanofibers by embedding Si nanoparticles as an alloying medium in electrospun carbon nanofibers. The Si/C composite anode have exhibited

a reversible capacity of around 800 mAh g<sup>-1</sup> and a capacity retention of 85% after 20 cycles (Figure 1.10). It is concluded that the electrospinning and subsequent carbonization were effective methods to prepare Si/C composite nanofibers due to low cost, improved cycling performance and high reversible capacities<sup>1, 72-74</sup>. Various methods of fabricating Si/C composite anodes have been investigated. For example, Wilson *et al.*<sup>75</sup> have reported the use of chemical vapor deposition to disperse Si into carbon and obtained a reversible capacity of about 500 mAh g<sup>-1</sup>. Guo *et al.* and Ng *et al.*<sup>76, 77</sup> have developed carbon-coated silicon and spray-pyrolysis methods, respectively, in order to increase the cycling performances. All the results demonstrated that anodes of Si/C composites combined the advantageous properties of carbon (long cycle life) and Si (high Li storage capacity).

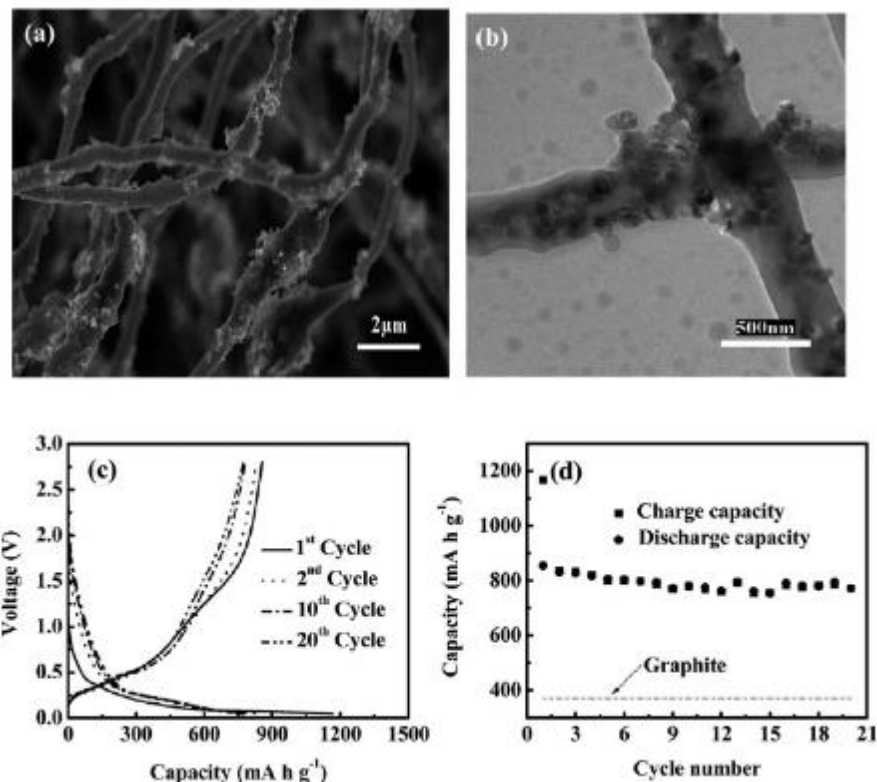


**Figure 1.10. (a) SEM and (b) TEM images of Si/carbon composite nanofibers, (c) Galvanostatic charge-discharge curves, and (d) cycling performance of Si/carbon nanofibers<sup>1</sup>.**

Many research groups have demonstrated the stable cycle performance and enhanced capacities of composite electrodes with porous structures<sup>28, 78-80</sup>. For example, macroporous crystalline silicon particles coated with less than 10 nm of amorphous carbon have shown a reversible capacity of 2780 mAh g<sup>-1</sup> after 100 cycles (Figure 1.11)<sup>81, 82</sup>. A porous Si/C nanocomposite was synthesized by adding Si nanoparticles to a hierarchical carbon monolith through a fabricating process<sup>83</sup>. In addition, mesoporous Si/C core-shell nanowires were shown of having an excellent first charge capacity of 3163 mAh g<sup>-1</sup>, a Coulombic efficiency

of 86% and a capacity retention of 78% after 80 cycles at a rate of 0.2 C ( $600 \text{ mA g}^{-1}$ )<sup>84</sup>. These studies further validate the concept of using porous carbon-containing composites with high surface area in the design of high performance electrode materials.

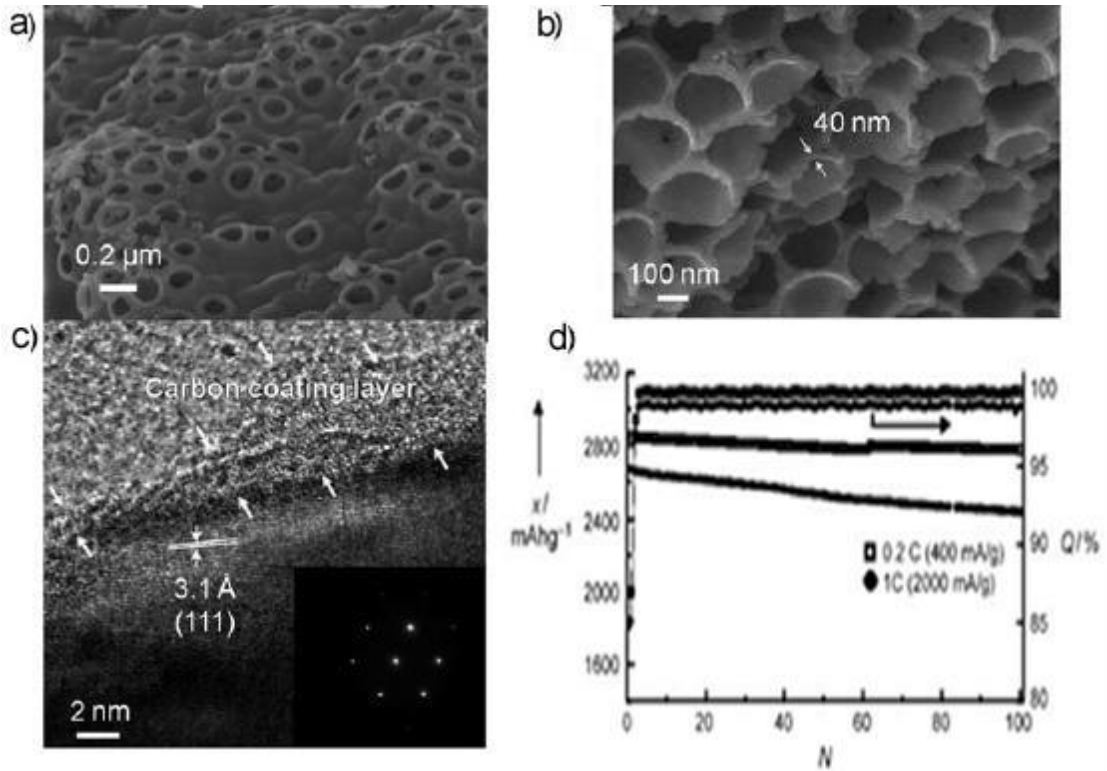


**Figure 1.11.** (a) SEM images of the 3D porous C-Si particles after etching, (b) cross-sectioned image of (c), (c) TEM image of the cross-sectioned 3D porous c-Si particle (the inset shows a selected area diffraction pattern (SADP)), and (d) charge capacities versus cycle number of the 3D porous c-Si particles cycled at different rates (0.2 C and 1 C) between 0 and 1.5 V in coin-type half cells. X=charge capacity, N=cycle number, Q=coulombic efficiency<sup>83</sup>.

O element and Si oxides can also be added to the Si/C structure to obtain relatively good electrochemical performance with high charge-discharge capacities and long cycle life. Si-O-C composite materials, which were prepared by pyrolyzing a copolymer of phenyl-substituted polysiloxane and divinylbenzene at 800 °C under a hydrogen atmosphere, had a high delithiation capacity about 965 mAh g<sup>-1</sup> in the first cycle and retained 660 mAh g<sup>-1</sup> after 40 cycles<sup>85</sup>. In addition, an anode using Si@SiO<sub>x</sub>/C nanocomposite was prepared by coating Si with a thin layer of SiO<sub>x</sub> and carbon from the hydrothermal carbonization of glucose at 200 °C<sup>13, 86</sup>. The obtained Si@SiO<sub>x</sub>/C nanocomposite (Figure 1.12a and b) exhibited the desired core/shell structure and showed a better cycling performance than pure Si nanoparticles (Figure 1.12c). An excellent cycling performance was achieved in a VC-containing electrolyte with a reversible capacity of 1100 mAhg<sup>-1</sup> even after 60 cycles.

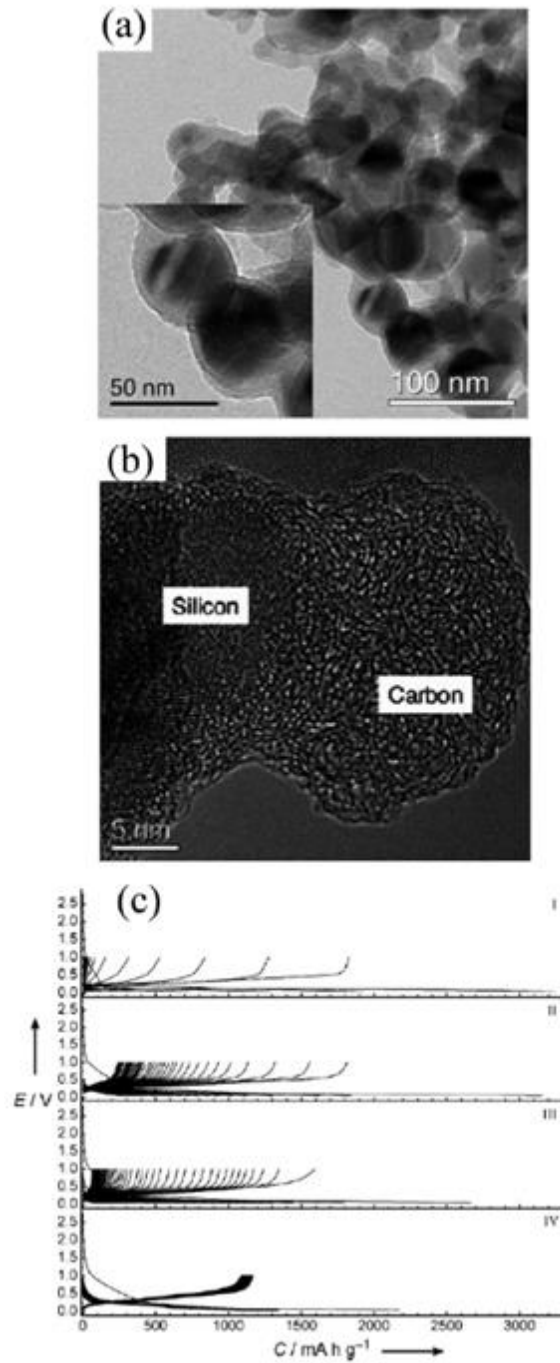


Figure 1.12. a) TEM image of the Si@SiO<sub>x</sub>/C nanocomposites. Inset: TEM image at a higher magnification. b) High-resolution TEM image of the Si nanoparticles coated with SiO<sub>x</sub> and carbon. c) Galvanostatic discharge-charge curves of pure Si

**nanoparticles (I, II) and Si@SiO<sub>x</sub>/C nanocomposite (III, IV) electrodes cycled at a current density of 150 mA g<sup>-1</sup> between voltage limits of 0.05 - 1.0 V in VC-free (I, III) and VC-containing (II, IV) 1m LiPF<sub>6</sub> in EC/DMC solutions<sup>13</sup>.**

A second element can also be complemented in forming Si-based alloys. It can be either a electrochemically active or inactive component, which serves as buffering the volume change of Si during cycling and increasing the conductivity of the electrode<sup>1, 60, 87, 88</sup>. If the second element is electrochemically active, it will join Si as a mutual buffer to each other to overcome the large volume expansion. Besides, these elements provide higher theoretical capacities and they are relatively cheap and abundant<sup>89-91</sup>. Si-based alloys such as CaSi<sub>2</sub><sup>92</sup>, FeSi<sub>6</sub><sup>93</sup>, TiSi<sup>94</sup>, Mg<sub>2</sub>Si<sup>95</sup> and many other elements have been investigated by many research groups. The voltage profiles of these Si-based anodes are similar to those of pure Si or Si/C anodes as mentioned above.

#### 1.6.2.2 Ge and Ge/C nanocomposites

Ge shows a high theoretical capacity of 1600 mAh g<sup>-1</sup>, which is 40% of the Si theoretical capacity. Compared with Si-based material, Ge exhibits a higher diffusivity of Li and a lower volume change around 370% during the lithiation and delithiation process<sup>96</sup>. Even so, an electrode based on Ge still suffers from poor cyclability<sup>96-99</sup>. For example, bulk Ge, Ge nanocrystals (12 nm mean diam) and Ge nano films (60 - 250 nm thick) were investigated and shown in Figure 1.13. The Ge nanocrystals showed reversible capacities of up to 1400 mAh g<sup>-1</sup> with 60% capacity retention after 50 cycles. Amorphous Ge thin film electrodes

showed capacities of  $1700 \text{ mAh g}^{-1}$  with no capacity loss over 60 cycles. However, bulk germanium exhibited a poor cycle life, with nearly complete capacity loss by the 7<sup>th</sup> cycle. It was discussed that the high surface area, short diffusion length of the active material and the absence of defects in nanophase materials attributed to the enhanced reversible capacity, rate capability and cycle life. These results suggest that nanoscale structures facilitate lithium ion diffusion rates and thus improve the reversible capacities and cycling stability<sup>96</sup>.

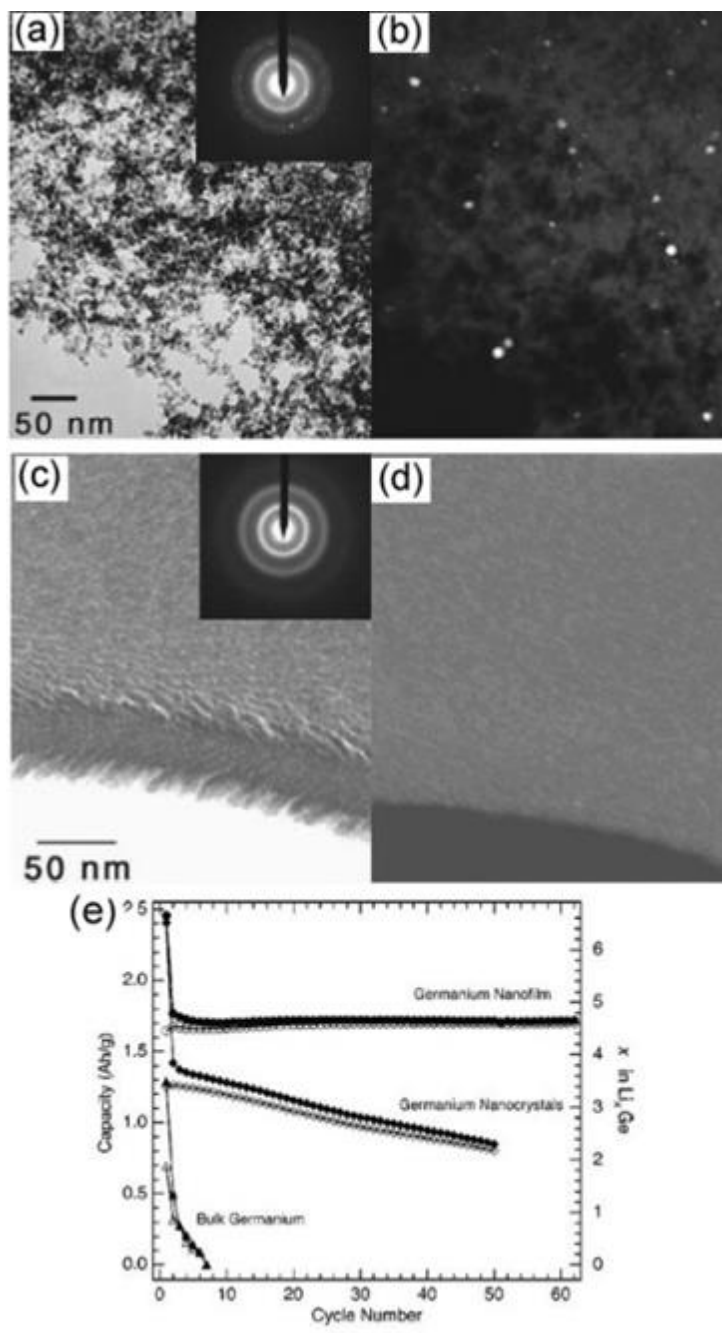
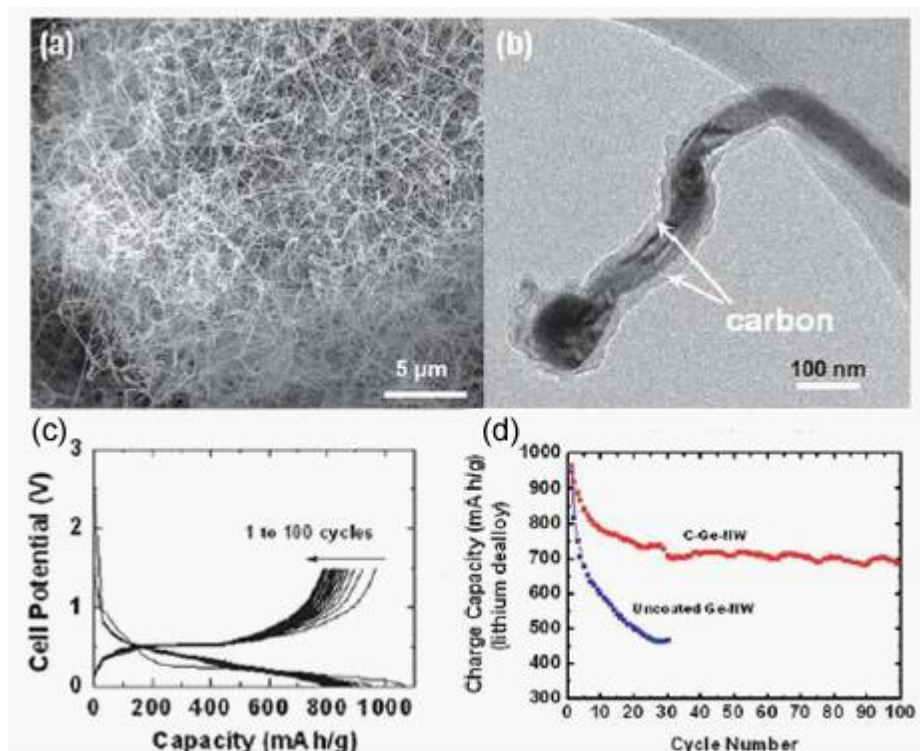


Figure 1.13. (a) Bright-field (Inset: the electron diffraction pattern), (b) dark-field TEM images of ballistically deposited germanium showing an agglomeration of nanocrystals, (c) bright-field (Inset: the electron diffraction pattern), (d) dark-field TEM images of

**evaporated germanium showing a uniform amorphous thin film, and (e) cycle life of germanium from ballistically deposited nanocrystals, an evaporated amorphous nanofilm, and the control sample of bulk crystalline germanium. The light and shaded markers represent the charge and discharge cycles, respectively<sup>96</sup>.**

Similar to Si, Ge nanoscale material suffers from agglomerations, leading to increased diffusion lengths, as well as electrical isolation of the particles due to volume changes that occur during the insertion and extraction process<sup>100</sup>. To accommodate the large volume change and nanoparticle agglomeration, carbon matrix functioning as a structural buffer and electro-active material has been given much attention<sup>98-100</sup>. For example, Seo *et al.*<sup>101</sup> presented a single crystalline Ge nanowire (GeNW) anode material sheathed with carbon prepared by a solid–liquid solution method. The composite electrode composed of Ge nanowires and carbon matrix showed good electrochemical properties, exhibiting a relatively high reversible capacity of 963 mAh g<sup>-1</sup> with a coulombic efficiency of 91% at the first cycle. The morphology and cyclic performance of the carbon sheathed GeNW anode material were shown in Figure 1.14. It was discussed that the excellent electrochemical properties of high reversible capacity, high coulombic efficiency, excellent rate capability and stable cycle performance were attributed to the formation of amorphous GeNWs during cycling and a homogenous carbon coating on discrete GeNWs<sup>101</sup>. Another example of Ge/carbon composite anode was prepared by Cui *et al.*<sup>100</sup> using solid-state pyrolysis of tetraallylgermane. These Ge/carbon nanospheres had an average diameter ranging from 50 nm to 70 nm with 5 - 20 nm encapsulated Ge nanoparticles. These materials exhibited high

discharge and charge capacities of 1190 and 923 mAh g<sup>-1</sup> in the first cycle, respectively. The Coulombic efficiency is as high as 78%. An excellent rate performance was observed at a further increase in current density from 150 to 300, 600, and 900 mA g<sup>-1</sup>. The high performance of Li storage was ascribed to the small grain size of the Ge phase and the carbon phase confinement of Ge particles from disintegration and agglomeration.



**Figure 1.14.** (a) SEM image of GeNWs with carbon coating, (b) TEM image of GeNWs with carbon coating, (c) voltage profiles of GeNW with carbon coating at the 0.5 C rate, and (d) cycle performance of uncoated and carbon sheathed GeNWs at a rate of 0.5 C between 0 and 1.5 V<sup>101</sup>.

A better performance shown in Figure 1.15 was obtained using porous Ge/C structure by Tan and coworkers. They reported an improved specific capacity of a composite anode material with GeNW embedded in porous carbon via the solution-liquid-solid method. At a current density of  $160 \text{ mA g}^{-1}$  and voltage window of  $0.001 - 1.5 \text{ V}$ , the high initial reversible charge capacities were  $1030 \text{ mAh g}^{-1}$  and  $930 \text{ mAh g}^{-1}$  for the GeNW and GeNW/porous carbon (PC-GeNW) composite, respectively. After 50 cycles, the reversible capacity of PC-GeNW was  $789 \text{ mAh g}^{-1}$ , which was 27% larger than that ( $624 \text{ mAh g}^{-1}$ ) of pure GeNW. Even though the content of the Ge was only 53.5 wt% in the PC-GeNW composite, it yielded a better stability and higher specific capacity after 15 cycles, indicating a synergistic effect between porous carbon and Ge nanowires. The porous carbon successfully buffered the volume change and provided high surface area to allow the fast entrance of Li ions<sup>102</sup>.

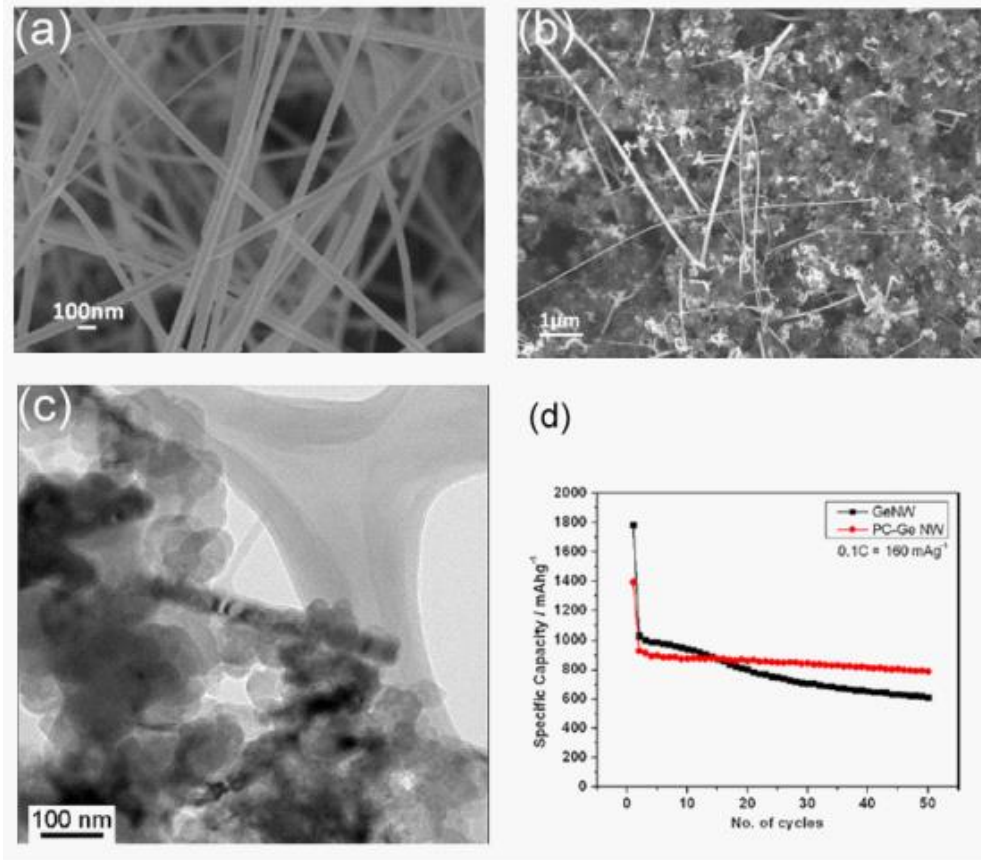


**Figure 1.15. SEM images of (a) GeNW, (b) PC-GeNW, (c) TEM image of PC-GeNW and (d) cycling performance of GeNW and PC-GeNW anodes<sup>102</sup>.**

To further minimize the electrode swelling, Chae *et al.*<sup>103</sup> and Hwa *et al.*<sup>104</sup> incorporated inactive Cu<sub>3</sub>Ge phase into the Ge/C phase by the Pechini method and pyrolysis method followed by mechanical milling process, respectively. Better cyclic stability of Ge/Cu<sub>3</sub>Ge/C composite anodes suggested that the Cu<sub>3</sub>Ge phase successfully played as the buffer against the volume change of Ge component together with carbon matrix<sup>103, 104</sup>. Figure 1.16 shows the TEM images (Figure 1.16a and b), XRD patterns (Figure 1.16c) and the cycling

performance (Figure 1.16d) of Ge/C and Ge/Cu<sub>3</sub>Ge/C anodes prepared by Chae *et al.* They obtained the first delithiation capacities of 1513 and 1530 mAh g<sup>-1</sup>, which were calculated by the weight of Ge component, for the Ge/C and Ge/Cu<sub>3</sub>Ge/C electrodes respectively. After 50 cycles, the reversible capacities of Ge/Cu<sub>3</sub>Ge/C electrodes were much higher than those of Ge/C electrodes since Ge/Cu<sub>3</sub>Ge/C electrodes exhibited a slower decreasing tendency. It was observed that by adding the Cu precursor in the preparation step, nanosized (<100 nm) and sphere-shaped Ge/Cu<sub>3</sub>Ge particles were obtained. The size reduction compared to Ge particles (~800 nm) in Ge/C electrodes was ascribed to the suppression of grain growth by the presence of Cu component. The cycling performance of Ge electrode was improved by incorporating an electrochemically inactive Cu<sub>3</sub>Ge phase due to the down-sizing effect to alleviate the absolute volume change and the buffering action of the Cu<sub>3</sub>Ge phase against the massive volume change of the Ge component. Besides, the high electronic conductivity of Cu<sub>3</sub>Ge phase may also contribute in improving cycling performance since Cu<sub>3</sub>Ge phase can provide a conductive network in the electrically loosened electrode layer<sup>103</sup>. Likewise, Mg-Ge<sup>105</sup>, Mg<sub>2</sub>Ge/Si<sup>106</sup>, Cu-Si<sub>1-x</sub>Ge<sub>x</sub><sup>107</sup>, Si/Ge, Ge/SnP<sub>0.94</sub><sup>108</sup> and Si-Ge-Mo composite anodes were investigated by various analytical techniques and exhibited large charge-discharge capacities and excellent cycling performance by mitigating the severe volume change of Ge with improved electric conductivity.

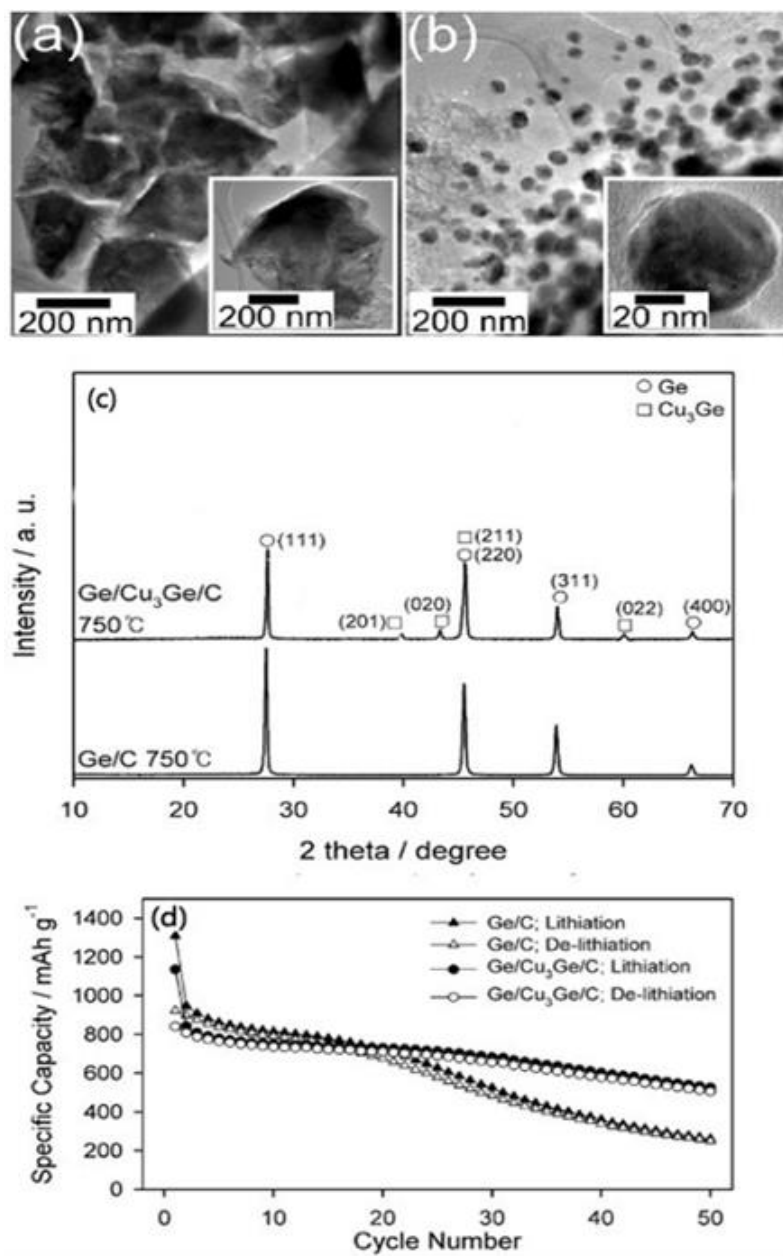
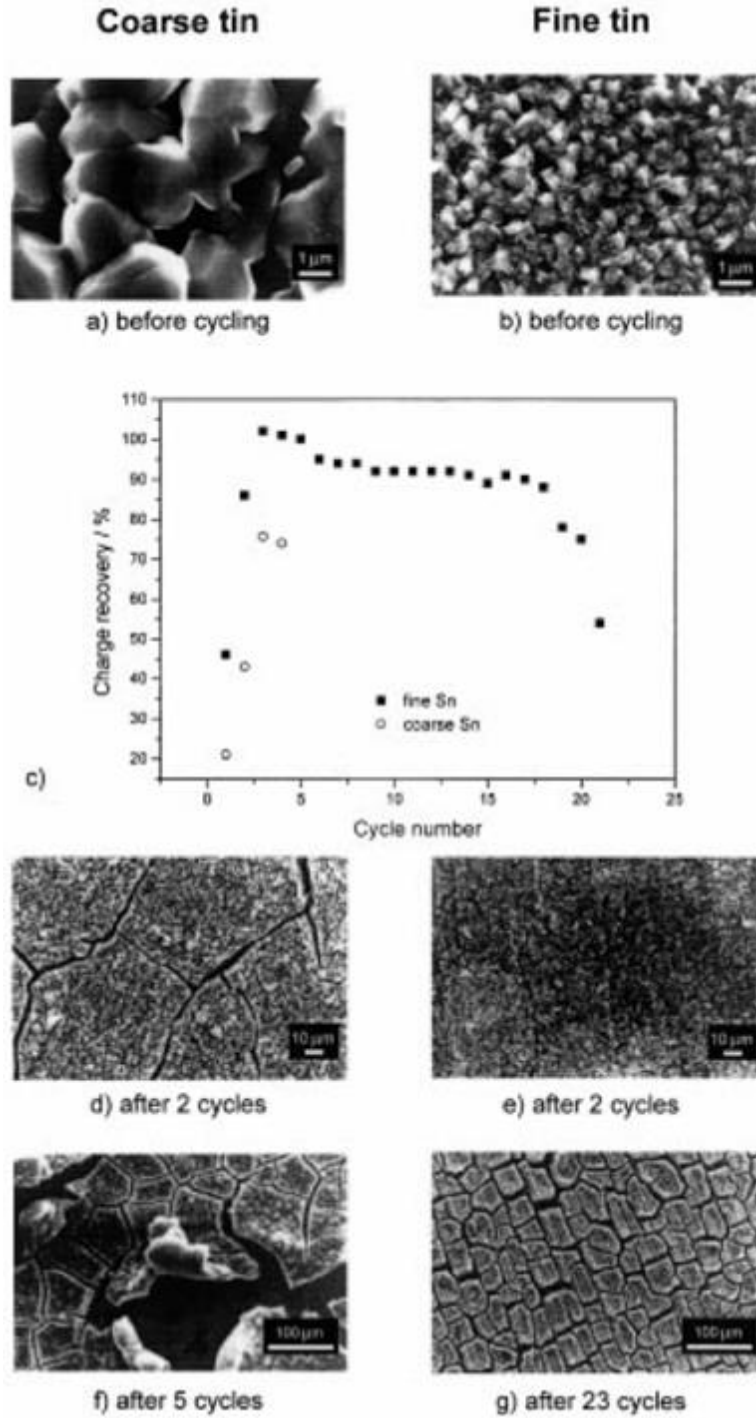


Figure 1.16. HR-TEM images of (a) Ge/C composite powders, (b) Ge/Cu<sub>3</sub>Ge/C composite powders, (c) XRD patterns of the Ge/Cu<sub>3</sub>Ge/C and Ge/C composite powders, and (d) the charge and discharge capacities as a function of cycle number for two electrodes. Current density = 100mA g<sup>-1</sup>, voltage cut-off range = 0.001 - 2.0 V<sup>103</sup>.

### 1.6.2.3 Sn and Sn/C composites

Sn yields a relatively high theoretical capacity of  $994 \text{ mAh g}^{-1}$ , which is equivalent to about 2.5 times of the capacity of graphite and have been given considerable interest for use as negative-electrode materials<sup>109, 110</sup>. However, like other Group IV element, Sn also exhibits inherently poor cycling stability due to large volume change and pulverization of the electrode during lithiation and delithiation process<sup>110-113</sup>. Figures 1.17a-c illustrate the morphology and cycling performance of coarse and fine tin particles, respectively. The degradation of the coarse and fine particulate tin electrodes is demonstrated by the SEM images in Figures 1.17d-g. In the case of coarse tin particles, large cracks formed and dissociated active material from the structure during cycling. The cracks allowed the electrolyte to penetrate into fissures to form electronically insulating products, as well as the gradual loss of active material from the electrode after repeated cycling. Finally, the electrode failed. However, in the case of fine tin particles, they tended to maintain the structure and thus showed a better cycling performance with well-balanced structure after 23 cycles<sup>16</sup>.



**Figure 1.17.** (a and b) SEM images of Sn films: (a) coarse particles (2 - 4 mm), (b) fine particles (0.2 - 0.4 mm), (c) cycling performance of coarse Sn and fine Sn materials, (d-

**g) SEM images of the discharged Sn at different cycle numbers: (d and f) coarse Sn, (e and g) fine Sn particles<sup>16</sup>.**

To alleviate the severe expansion and contraction of the structure, prevent disintegration and aggregation of Sn, and mitigate the detachment of the active material, encapsulation of Sn nanoparticles with carbon was proposed by different methods and structures<sup>114-125</sup>. Yu *et al.*<sup>122</sup> developed Sn/C nanofibers from electrospun SnCl<sub>4</sub>/PAN composite fibers by stabilization in air and carbonization in nitrogen at 550, 700, 850, and 1000 °C, respectively (Figure 1.18). For comparison, as-received carbon nanofibers were also prepared by stabilization and carbonization at 850 °C. The resultant Sn/C composite nanofiber anodes combined effects of nano-sized Sn and carbon matrices and exhibited a large reversible capacity and good cycling performance. It was concluded that the Sn/C nanofibers carbonized at 700 and 850 °C presented much higher charge (785.8 and 811 mAh g<sup>-1</sup>) and discharge (1211.7 and 993 mAh g<sup>-1</sup>) capacities than those at 550 and 1000 °C and the as-received carbon nanofibers<sup>122</sup>. Other synthesis procedures of Sn/C composite so far used various type of precursors for carbon-resins<sup>126, 127</sup>, polymers<sup>117</sup>, sucrose<sup>116</sup>, graphite<sup>128, 129</sup>, and activated carbon<sup>130</sup>.

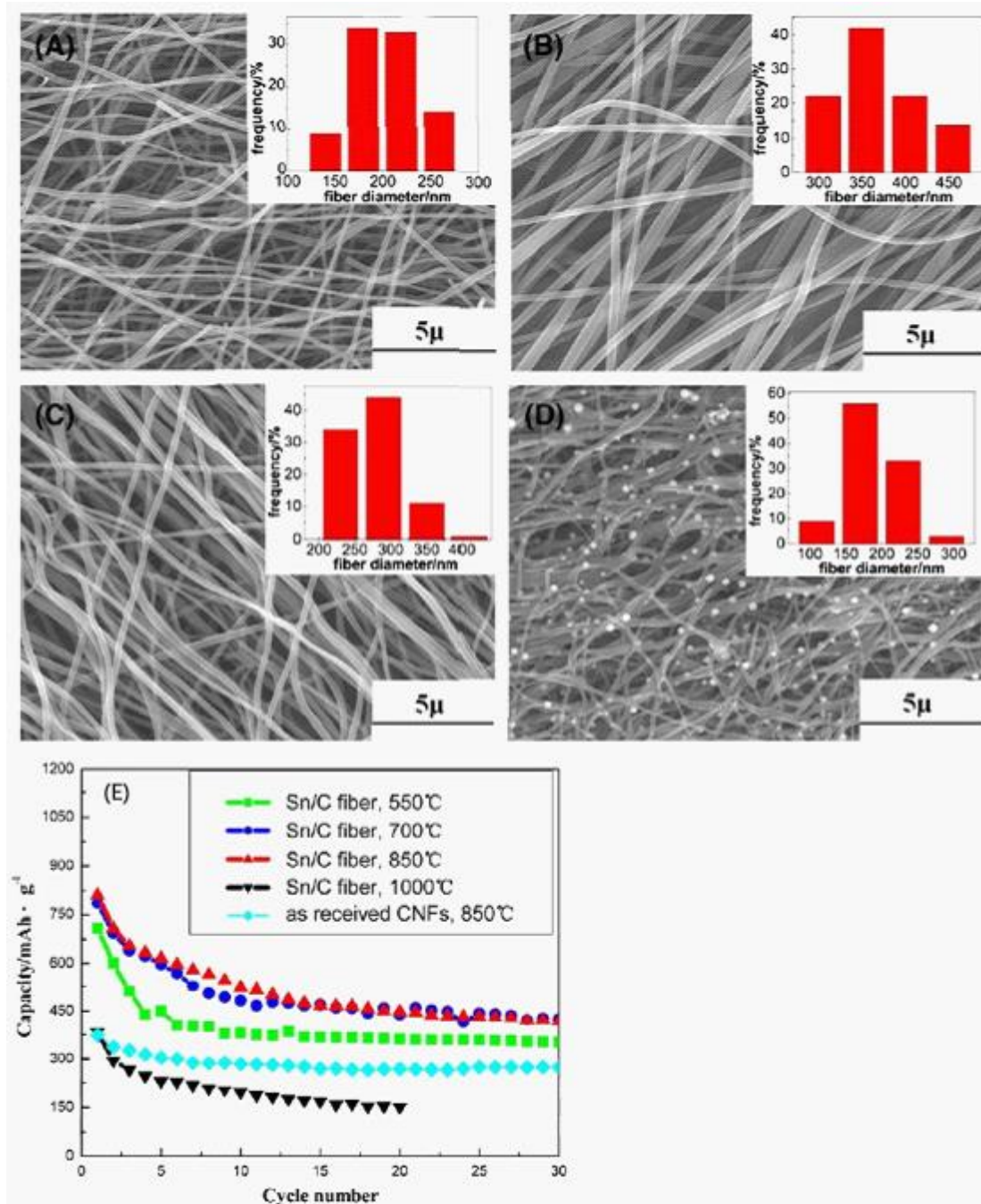
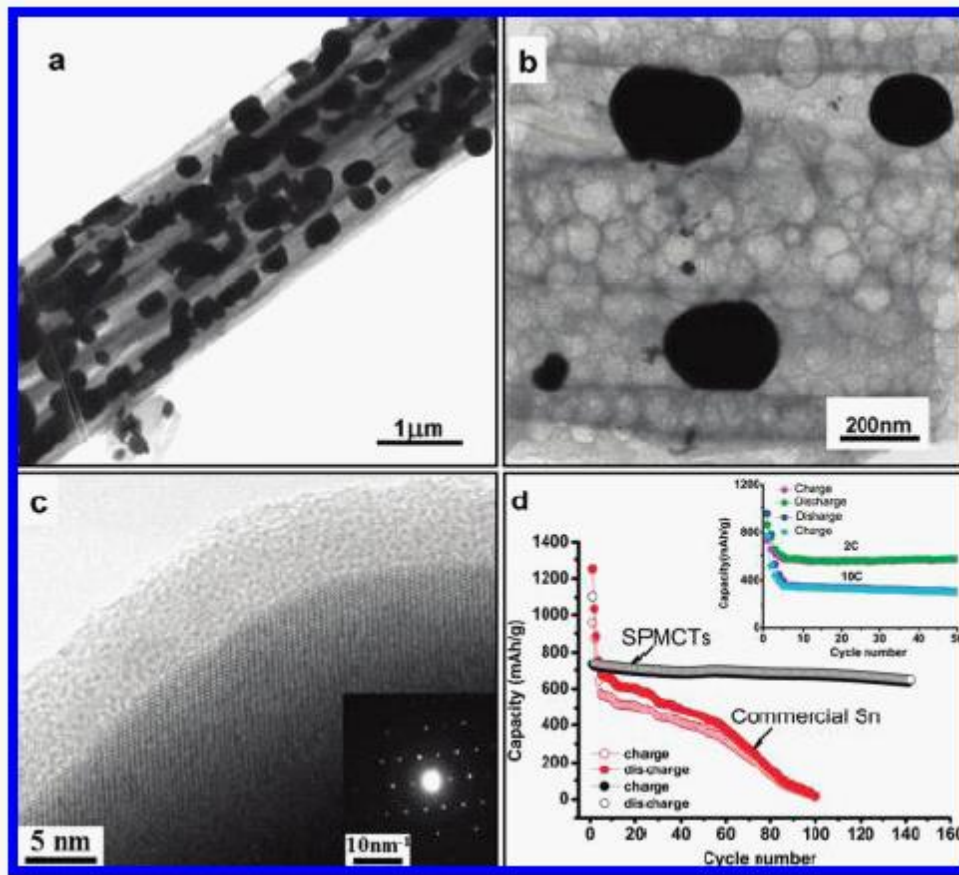


Figure 1.18. SEM images and diameter distribution of (A) as-received carbon nanofibers carbonized at 850 °C and Sn/C nanofibers carbonized at (B) 700, (C) 850,

**(D) 1000 °C, and (E) reversible capacities versus cycle numbers of as-received carbon nanofibers and Sn/C nanofibers carbonized at different temperatures<sup>122</sup>.**

Porous structural materials are new promising electrode materials for Li-ion batteries and have been proved to feature: (i) large open pores that allow fast transport of liquid electrolyte, (ii) large amount of active sites for charge transfer reactions due to the high surface area of materials, and (iii) numerous pores that can buffer the large volume change<sup>131, 132</sup>. Recently, a novel porous Sn/C composite with core-shell morphology of Sn nanoparticles encapsulated in porous multichannel carbon microtubes that was fabricated by electrospinning technique and subsequent calcinations, shown in Figure 1.19. A 30% capacity loss of the first cycle was observed, after which the Coulombic efficiency approached 100% (Figure 1.19d). Notably, the porous core-shell Sn/C electrode provided a reversible discharge capacity as high as 648 mAh g<sup>-1</sup> even after 140 cycles. It was concluded that the cooperation between a high density of tin particles and sufficient space of carbon were achieved. Furthermore, the porous carbon shell maintained the stability of the electrode structure and also avoided oxidation of Sn. In addition, the single nozzle electrospinning technique was proved to be a powerful alternative among techniques synthesizing one-dimensional core-sheath Sn/C composites<sup>133</sup>. Apart from the multichannel carbon microtube structure, other carbon structures, such as mesoporous carbon<sup>134</sup>, bamboo-like hollow carbon nanofibers<sup>135</sup>, hierarchical carbon<sup>123</sup>, and hollow carbon spheres<sup>119, 120</sup> were demonstrated to accommodate nanometer-sized Sn particles and obtained high specific capacities and good cycling performance.



**Figure 1.19.** (a) TEM micrograph of the converted Sn encapsulated in multichannel carbon microtubes after heat treatment under an Ar/H<sub>2</sub> atmosphere. (b) HRTEM image confirming the porous multichannel walls. (c) HRTEM micrograph and SAED pattern of an isolated Sn nanoparticle, revealing the presence of single-crystalline metallic tin and amorphous carbon. (d) Cyclability of Sn particles encapsulated in porous multichannel carbon microtubes and commercial Sn nanopowder with similar sizes (~200 nm) at a cycling rate of 0.5 C (current density 100 mA g<sup>-1</sup>); the inset displays the discharge capacities of Sn particles encapsulated in porous multichannel carbon

**microtube electrodes as a function of discharge rate at 2 and 10 C. All of the batteries were cycled in a voltage window of 5 mV to 2 V<sup>133</sup>.**

To achieve better cycle performance of Sn anodes, Sn-based alloys, including Sn–Co<sup>136, 137</sup>, Sn–Ni<sup>138, 139</sup>, Sn–Sb<sup>124, 140</sup>, and Sn–Cu<sup>141-144</sup> have also received great attention.

### 1.6.3 Transition metal oxides

Interstitial-free 3D transition-metal oxides ( $M_xO_y$ ,  $M = \text{Fe, Co, Ni, Mn, Cu, etc.}$ ) are capable of incorporating more than one Li per metal, hence providing a relatively high theoretical capacity<sup>145-147</sup>. The reaction mechanism of the  $M_xO_y$  electrodes is mainly related to reversible formation and decomposition of  $\text{Li}_2\text{O}$  upon Li uptake and release<sup>1, 4</sup>. Transition metal oxides are converted to a metallic state through a conversion reaction



The reverse feasibility of this reaction can be ascribed to the highly reactive metallic domains embedded in a  $\text{Li}_2\text{O}$  matrix, which is generated during the first lithiation process<sup>4</sup>. Correspondingly, these metal oxides exhibit high capacities and energy densities due to the fully utilized oxidation state and more than one electron involved in the reaction<sup>148</sup>. However, they often show low Coulombic efficiency at the first cycle, unstable SEI film formation and large potential hysteresis<sup>1</sup>. To solve these problems, researchers have been focused on porous nanostructured transition metal oxide materials and transition metal

oxide/carbon nanocomposites recently<sup>149</sup>. In the following section, we will discuss some studies based on cobalt oxide in this category, which are highly related to my research.

#### 1.6.3.1 Co<sub>3</sub>O<sub>4</sub> and Co<sub>3</sub>O<sub>4</sub> nanocomposites

Co<sub>3</sub>O<sub>4</sub> can store more than eight lithium atoms per formula unit, corresponding to a high theoretical capacity of 890 mAh g<sup>-1</sup><sup>150, 151</sup>. However, as an anode material, it experiences a relatively large volume change and an unstable SEI. This causes the pulverization of the electrodes with decreased electrical conductivity and reversible capacity<sup>151, 152</sup>.

Co<sub>3</sub>O<sub>4</sub> microspheres (shown in Figure 1.20) were synthesized by a simple hydrothermal treatment by Liu *et al.*<sup>153</sup>. Micrometer-sized spherical particles were obtained with high specific surface area (93.4 m<sup>2</sup> g<sup>-1</sup>) and large pore volume (78.4 cm<sup>3</sup> g<sup>-1</sup>). The porous structure offered more interfacial bondings for extra sites of Li<sup>+</sup> insertion, which resulted in a large initial irreversible capacity and capacity cycling loss caused by SEI film formation. The capacity retention of Co<sub>3</sub>O<sub>4</sub> microspheres was almost above 90% at the 12th cycle and it retained a lithium storage capacity of 550.2 mAh g<sup>-1</sup> after 25 cycles, indicating good long-life stability. Moreover, another work<sup>154</sup> investigated these large Co<sub>3</sub>O<sub>4</sub> nanocubes, hexagonal Co<sub>3</sub>O<sub>4</sub> nanodiscs and Co<sub>3</sub>O<sub>4</sub> nanoflowers. The nanoflower sample showed highly reversible lithium storage capability after 100 charge-discharge cycles. Furthermore, Co<sub>3</sub>O<sub>4</sub> mesoporous nanowire arrays<sup>155</sup> and needle-like nanotubes<sup>156</sup> were prepared using a template-free ammonia evaporation-induced method and a self-supported topotactic transformation route from Co(OH)<sub>2</sub>, respectively. They released first discharge capacities around 1000 mAh

$\text{g}^{-1}$  with nearly 100% retention over 30 cycles and maintained a stable capacity of  $700 \text{ mAh g}^{-1}$  after 20 cycles.

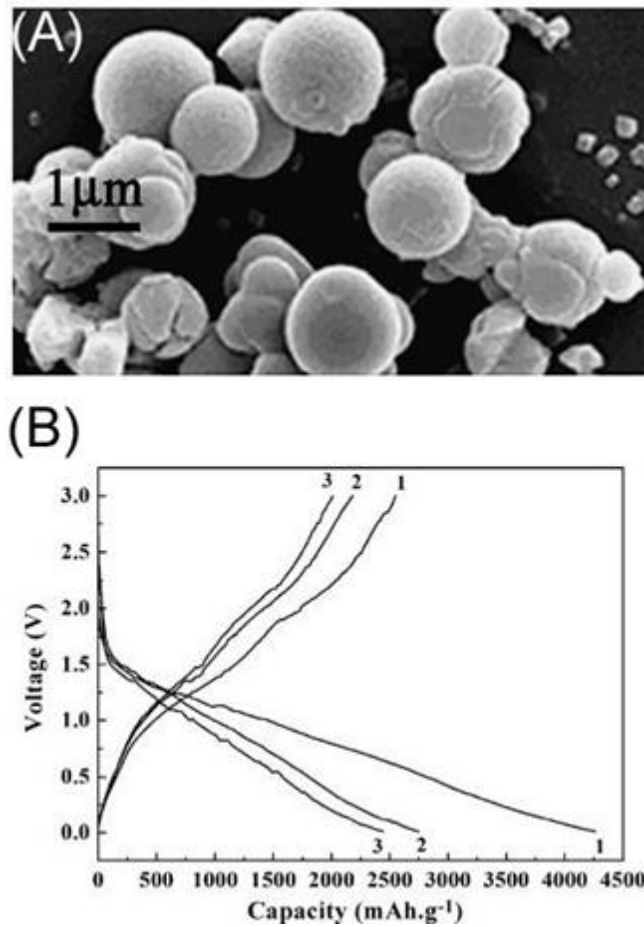


**Figure 1.20.** (A) SEM image of  $\text{Co}_3\text{O}_4$  microspheres calcined at  $200 \text{ }^\circ\text{C}$ . (B) The initial three-cycle charge–discharge curves of  $\text{Co}_3\text{O}_4$  electrode at a current density of  $15 \text{ mA g}^{-1}$  between  $0.01$  and  $3.0 \text{ V}$ <sup>153</sup>.

The cycling stability of nanometer-sized  $\text{Co}_3\text{O}_4$  can be improved by uniformly embedding nanoparticles in carbon through solid-state pyrolysis of organic cobalt precursors under an inert atmosphere, followed by mild thermal oxidation<sup>151</sup>. The obtained  $\text{Co}_3\text{O}_4/\text{C}$  nanocomposites consisted of  $\text{Co}_3\text{O}_4$  nanoparticles of approximately 20 nm diameter (Figure 1.21a) and thin carbon layers covering the surface (Figure 1.21b). The initial reversible capacity reached at  $940\text{mAhg}^{-1}$  at a rate of C/5 with an initial Coulombic efficiency of about 73% (Figure 1.21c). This is significantly higher than that of pure  $\text{Co}_3\text{O}_4$  nanoparticles of similar particle size (64%). After 20 cycles, the reversible capacity of C-covered  $\text{Co}_3\text{O}_4$  was observed to be maintained at about  $940\text{mAh g}^{-1}$  with a Coulombic efficiency of above 99%, whereas the reversible capacity of the pure  $\text{Co}_3\text{O}_4$  nanoparticles rapidly decreased to around  $120\text{mAh g}^{-1}$  after 20 cycles (Figure 1.21d). The good cycling performance arose from the action of the carbon layers which played the role of structure buffer. Another example was presented by Yang *et al.*<sup>157</sup> with nanometer-sized  $\text{Co}_3\text{O}_4$  nanoparticles uniformly embedded in the pores of hard carbon spherules (HCS). A specific capacity of  $403\text{mAh g}^{-1}$  was preserved after 35 cycles. This improvement was attributed to the small size of the embedded  $\text{Co}_3\text{O}_4$  particles, alleviating volume variation and loose contact with the carbon matrix during repeated cycling, and to the high structural stability of the HCS, preventing the possible aggregation of the  $\text{Co}_3\text{O}_4$  nanoparticles. Besides, cobalt oxide–graphene composites with a homogenous dispersion of cobalt oxide into/onto the graphene sheets via a simple pyrolysis and oxidation process were prepared<sup>13</sup>. The obtained  $\text{Co}_3\text{O}_4$ –graphene composites exhibited remarkable Li storage performance with highly reversible capacity ( $754\text{mAh g}^{-1}$ ), good

cycle performance, and good rate capability mainly due to the mechanical confining of graphene sheets.

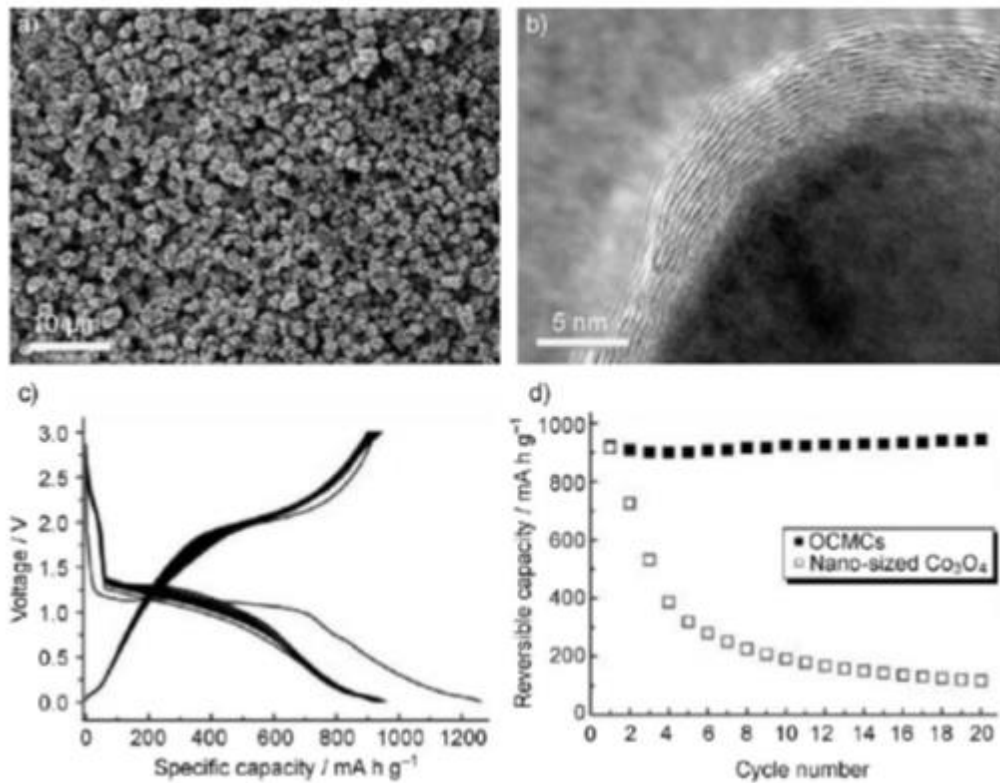


**Figure 1.21.** a) SEM image and b) high-resolution TEM image of the carbon/cobalt oxide nanocomposite. c) Galvanostatic discharge/charge curves of carbon/cobalt oxide nanocomposite, and d) comparison of the cycling performance of the nanocomposite (OCMCs) and nanometer-sized Co<sub>3</sub>O<sub>4</sub> electrodes<sup>151</sup>.

Finally, although it is inspiring to achieve the improvement in anode capacity, the total capacity of a battery levels off without an improvement in the cathode capacity<sup>158</sup>. Therefore, the development of new cathode materials with higher capacity is of urgent importance. In addition, most of the anode materials highlighted herein would be attractive for practical application in fabricating the new-generation lithium-ion batteries if it is possible for their successfully mass production.

### 1.7 Electrolytes

The most important characteristics of an electrolyte are the high  $\text{Li}^+$  conductivity and rapid  $\text{Li}^+$  motion within the electrolyte and across the electrode/electrolyte interface for lithium-ion batteries. Other desired characteristics of the electrolyte include low toxicity and low cost, as well as good stability and compatibility with electrode materials<sup>159</sup>. Traditional organic liquid electrolytes experience serious decomposition reactions at high temperatures under the circumstances of overcharging. Typical ionic liquids involve large organic cations such as imidazolium, pyridinium, and pyrrolidinium and the corresponding coordinated inorganic anions<sup>160</sup>. Because of their lower viscosity and high Li-salt solubility, modified imidazolium cation-based ionic liquids have been recognized as competitive electrolytes to sustain considerable battery performance<sup>160, 161</sup>. Solid electrolytes can be one of the most promising candidates, because they potentially allow the existence of the construction of lighter and safer all-solid-state batteries with design flexibility in the shape and size. Polymer electrolytes, which can serve as both electrolytes and separators between the anode and cathode, are of peculiar interest. Great attention has been focused on poly(ethylene oxide) (PEO) and related polymers that are blended with Li salts such as  $\text{LiXF}_6$  ( $\text{X} = \text{P}, \text{As}, \text{Sb}$ )<sup>161</sup>,

<sup>162</sup>. In addition to PEO-related electrolytes, poly(vinylidene fluoride) (PVDF)-based polymer electrolytes are also attractive candidates with ionic conductivities up to  $0.1 \text{ S m}^{-1}$  at room temperature<sup>163</sup>. They can act as membranes due to the intrinsically high electrochemical stability in a wide voltage range, good processability, and mechanical properties.

Asides from single liquids or solid electrolytes, the development of hybrid electrolyte systems is a new trend. The mixture of two or more electrolytes may realize the combined advantages of the individual components. For example, Li ion-containing solutions (e.g.,  $\text{LiPF}_6$  in carbonate solvent) trapped in a polymer matrix form a gel-type membrane that offers both high ionic conductivity and good mechanical stability<sup>161, 162, 164</sup>. Practically, PVDF-based gel electrolytes have been applied to pair with a Sn/C anode and a  $\text{LiNi}_{0.5}\text{Mn}_{1.5}\text{O}_4$  cathode to construct safe, high-rate, and high-energy cells. Therefore, a proper combination of newly developed anode, cathode, and electrolyte materials create opportunities for unprecedented achievements in rechargeable lithium-ion batteries.

## 2. Electrospinning technology

The field of electrospinning traces back to an initial patent on the electrical dispersion of fluids in 1902. Then in 1934 Formhals patented the fabrication of textile yarns from electrically dispersed fluids<sup>165</sup>. However, this technique did not receive much attention until the 1990s, when it was found to generate nanofibers from many organic polymers by several research groups (notably that of Reneker)<sup>166, 167</sup>. Since then, this technique started becoming very popular and the number of publications about electrospinning increased dramatically

each year. Today, electrospinning is an established technique for generating nanofibers<sup>166, 168-170</sup>.

## 2.1 Working principle

A typical electrospinning setup consists of a syringe, a grounded collector and a high voltage power supply (Figure 1.22)<sup>171</sup>. During a typical electrospinning process, a syringe is filled with polymer solution or melt and a high voltage is applied between the syringe nozzle and a collector<sup>172, 173</sup>. One of the fundamental differences between electrospinning and other mechanically driven spinning techniques is that the extrusion force is generated by the interaction between the charged polymer fluid and an external applied electric field<sup>165, 173</sup>. During electrospinning, a conical fluid structure called Taylor cone is formed at the tip of the syringe. At a critical voltage, the repulsive force of the charged polymer overcomes the surface tension of the solution and a charged jet erupts from the tip of the Taylor cone. If the applied voltage is not high enough, the jet will break up into droplets. If the voltage is sufficiently high, a stable jet will form at the tip of the Taylor cone. Beyond the stable region, the jet is subject to bending instability that results in the polymer being deposited on the grounded collector via a whipping motion. As the charged jet accelerates towards the region of lower potential, the solvent evaporates, and the resulting increased electrostatic repulsion of the charged polymer causes the fibers to elongate. The strength of the polymer chains prevents the jet from breaking up and result in the formation of fibers<sup>174-180</sup>.

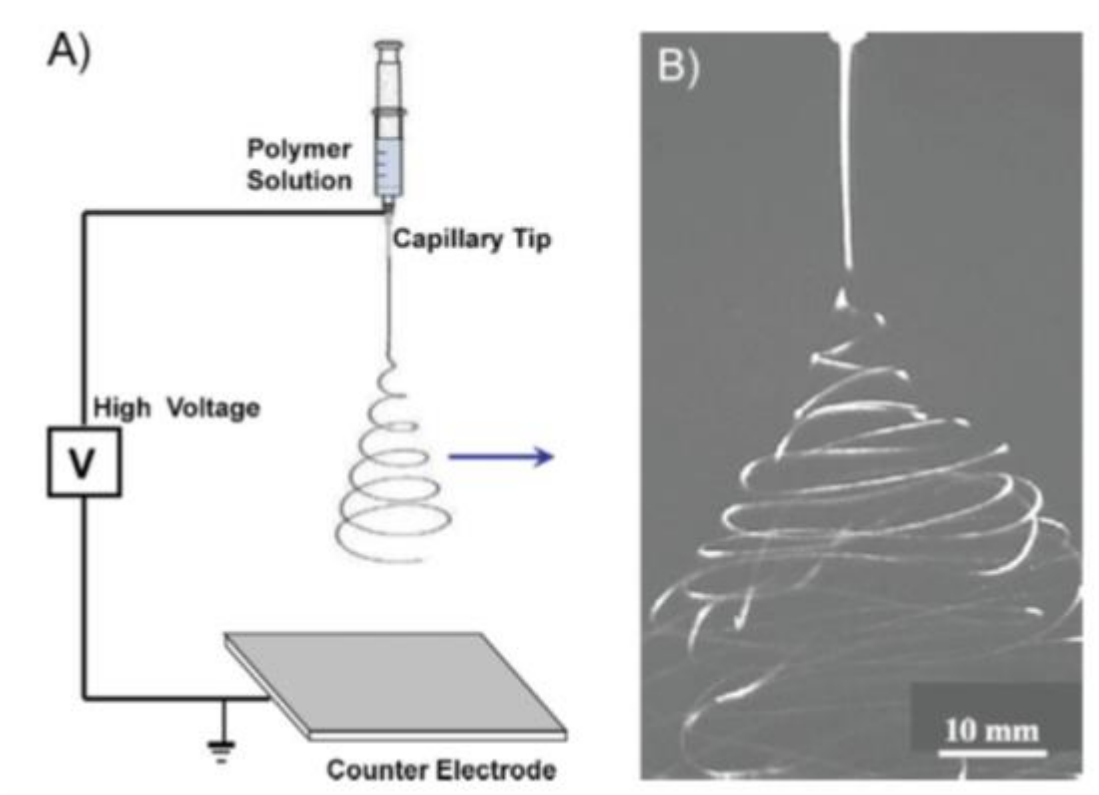


**Figure 1.22. A) Schematic diagram showing a laboratory setup for electrospinning. B) Photograph of an electrospinning jet captured by a high-speed video showing the bending instability of the jet<sup>171</sup>.**

Various electrospun nanofibers made of natural polymers, polymer blends, ceramic precursors and metal or metal oxides have been investigated for their different fiber morphologies, such as beaded<sup>181, 182</sup>, ribbon<sup>182, 183</sup>, porous<sup>184, 185</sup>, core-shell<sup>185</sup> and aligned<sup>186</sup> fibers (Figure 1.23). It is reported that about 40 - 60%<sup>168, 187</sup> of electrospinning publications focus on applications of tissue engineering<sup>188-190</sup>, drug delivery<sup>191-193</sup>, and wound healing<sup>192, 194, 195</sup>. In addition to biomedical applications, electrospinning has also been used in other

areas such as sensors<sup>196-198</sup>, separation membranes<sup>199, 200</sup>, protective layer<sup>165</sup> and energy applications<sup>1, 72-74, 122</sup>.

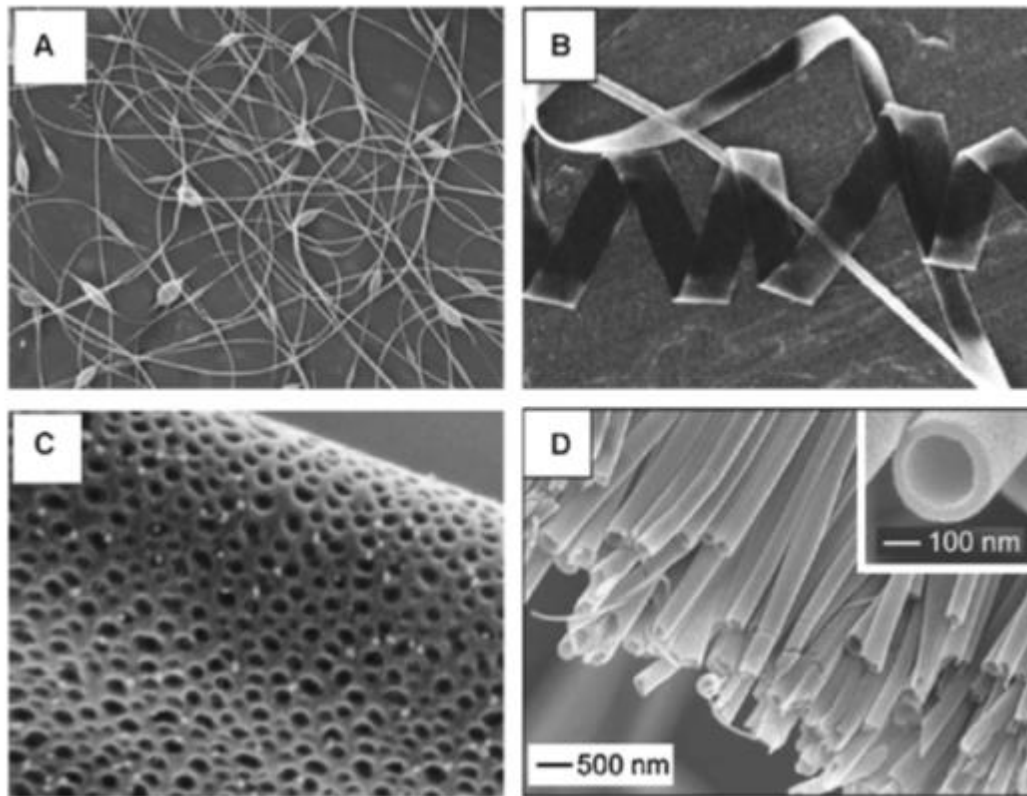


**Figure 1.23. Different electrospun fiber morphologies: (A) beaded, (B) ribbon, (C) porous, and (D) core-shell fibers<sup>165</sup>.**

## 2.2 Applications

As demonstrated in previous section, electrospinning is a remarkably simple and powerful technique for generating nanomaterials. Compared with bulk materials, electrospun fibers

offer many advantages due to the high surface-to-volume ratio<sup>175-178</sup>. Therefore, they have been applied in many fields, such as nanoelectronic and optical devices, sensors, electrocatalysis, superhydrophobic surfaces, environment, energy, and biomedical fields<sup>171</sup>.

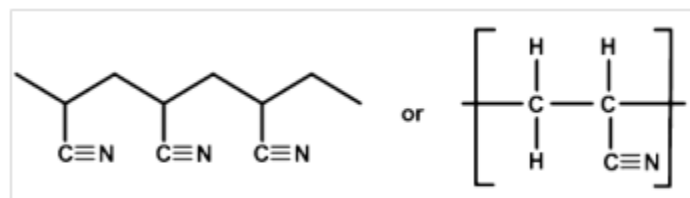
However, there are still many challenges with the use of nanofibers. Most of the studies in this area used small-scale electrospinning devices to electrospin nanofibers. Though it is possible to produce nanofibers in mass-production scale, efforts are still needed to evaluate the characteristics and performance of the fibers produced by the large-scale equipment. In addition, it is a challenge to produce uniform fibers with an average diameter below 100 nm, which is particularly the case for melt electrospinning. It is also worth noting that other non-electrospinning technologies, such as the melt-blown and micro fiber technologies used in the fiber industry, have the potential of producing submicron fibers. Hybrid technologies are being developed for mass production of nanofibers as well<sup>178-180</sup>.

### 2.3 Polyacrylonitrile as a precursor to carbon fibers

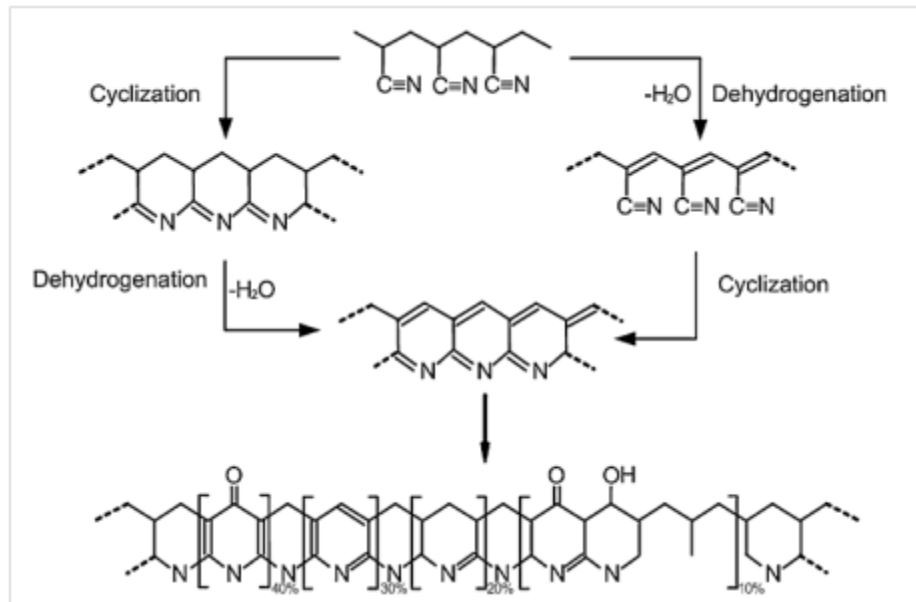
As a famous carbon precursor, Polyacrylonitrile (PAN) is frequently used in the production of commercial carbon fibers because of its high dielectric constant. In addition, poly(vinyl alcohol) (PVA), polyimides (PIs), polybenzimidazol (PBI) poly(vinylidene fluoride) (PVDF), phenolic resin and lignin are also popular precursors to convert to carbon nanofibers in lithium-ion battery application<sup>201</sup>.

Figure 1.24 shows the molecular structure of PAN. Two heat treatment steps involve in the process of converting PAN to carbon. The first heat treatment is done at 250 - 300 °C in air,

where PAN becomes a crosslinked structure (Figure 1.25) through dehydrogenation and cyclization reactions. The next thermal treatment step is performed in an inert atmosphere (e.g. nitrogen or argon) at 600 - 1300 °C in inert atmosphere. Carbonized nanofibers are obtained and the non-carbon elements are removed in the forms of methane, hydrogen, hydrogen cyanide, water, carbon dioxide, and ammonia, etc. The carbonized fibers, as shown in Figure 1.26, exhibits significant weight loss and shrinkage, resulting in the decrease of fiber diameter. The carbon fibers can undergo additional heat treatments up to 3000 °C for further graphitization<sup>201</sup>.



**Figure 1.24. Molecular structure of PAN<sup>201</sup>.**



**Figure 1.25. Stabilized PAN structure<sup>201</sup>.**

Both the carbon and graphite fibers are conductive and have many important applications. In our work, carbonized PAN nanofibers prepared by electrospinning are used as an anode material in lithium-ion batteries.

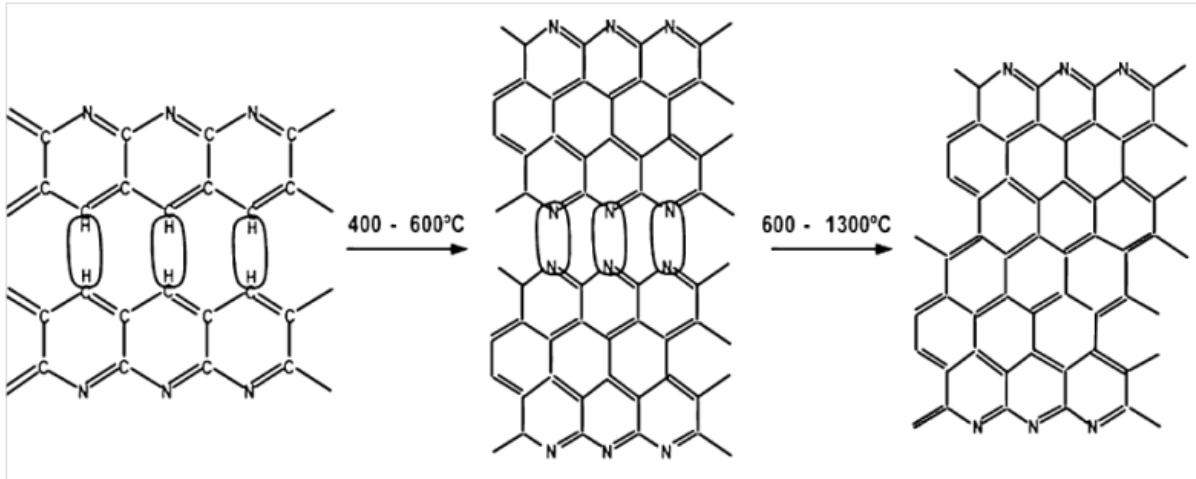


**Figure 1.26. Structure changes for PAN precursor during carbonization<sup>201</sup>.**

## CHAPTER 2 OBJECTIVES

The main objective of this work is to fabricate distinctive composite nanofibers and explore their potential applications as anode materials for new-generation high-performance rechargeable lithium-ion batteries. The work includes:

1. High-performance Sn/Carbon Composite Anodes Derived from Sn(II) Acetate/Polyacrylonitrile Precursor by Electrospinning

Intriguing Sn anodes have been one of the research focuses for lithium-ion batteries due to large theoretical capacity and relatively good cycling performance. However, Sn anode materials experience nanoparticle aggregation and large volume changes during the lithium insertion and extraction process, which result in structural failure and quick capacity loss of the anodes during charge/discharge cycles. To solve these two problems, carbon confinements and Sn-salts may help. In this work, Sn/C nanofibers derived from Sn(II) acetate/PAN precursors were fabricated. The carbon nanofiber and Sn(II) acetate can provide confinement for the huge volume changes of the nanoparticles and prevent nanoparticle aggregation, respectively. As a result, these composite nanofibers provided high charge-discharge capacities and good cycling performance.

## 2. Comparison of Si/Carbon, Ge/Carbon and Sn/Carbon Composite Nanofiber Anodes used in New-generation Lithium-ion Batteries

There has been much research interest in the development of higher-specific-energy lithium-ion batteries, particularly in higher-capacity alternatives for the commercially used graphite anode, such as group IV elements: Si, Ge and Sn. They show large theoretical specific capacities that are much higher than that of graphite. However, the metal and semi-conducting materials suffer from large volume change during lithium insertion and extraction, leading to decrepitation and loss of electrical contact in bulk electrodes. To alleviate the large volume changes during lithiation and delithiation process, nanocomposites of Si, Ge and Sn with confinement-material carbon nanofibers were investigated. The resultant promising electrochemical performance of Si/C, Ge/C and Sn/C can be attributed to their unique one-dimensional carbon nanofiber structure with effective confinement of the severe volume change, increased conductivity and shorter lithium ion diffusion distance in the nano-sized fibers.

## 3. $\text{Co}_3\text{O}_4$ /Carbon Composite Nanofibers for Use as Anode Material in Advanced Lithium-ion Batteries

Among various electrode materials, transition metal oxide  $\text{Co}_3\text{O}_4$  has received significant attention due to its relatively high theoretical specific capacity, low electrode potential, high Columbic efficiency, low cost and high level of safety. However,  $\text{Co}_3\text{O}_4$  electrodes suffer

from large initial irreversible loss, low electronic conductivity and poor cycling stability, which is related to the severe particle aggregations and relatively large volume change during lithium insertion/extraction process. To solve these problems, carbon confinement may help. In this work, two nano-sized particles, which are 10 - 30 nm and 30 - 50 nm, are used to produce  $\text{Co}_3\text{O}_4$ /carbon composite nanofiber anodes to examine the influence of carbon matrix on particle aggregations.

#### 4. Nanosized Ge@C@CNF and Ge@CNF@C composites via CVD method for use in advanced lithium-ion batteries

To further constrain the enormous volume change of Ge nanoparticles, additional carbon layer by chemical vapor deposition (CVD) method was deposited on the Ge/C nanofibers (Ge@CNF). In this work, two different approaches were used to mitigate the pulverization with amorphous carbon material fabricated by CVD method. In the first approach, nano-Ge nanoparticles were firstly coated with amorphous carbon by CVD method and subsequently mixed with CNF (referred to as Ge@C@CNF) by electrospinning technique. In the second approach, amorphous carbon fabricated by CVD method was used to coat the outer layer of the Ge@CNF composite nanofibers as a structural confinement material (referred to as Ge@CNF@C). As a comparison, Ge@CNF structure was also examined. The resultant morphology and electrochemical performance of Ge@CNF, Ge@C@CNF and Ge@CNF@C indicated the influence of the additional CVD carbon layer in this chapter.

## CHAPTER 3 OVERALL EXPERIMENTAL SECTION

### 1. Chemicals

PAN, Sn(II) acetate salt (99.995%, powder, anhydrous), solvent N, N-dimethylformamide (DMF), Li ribbon and copper foil (thickness is 25  $\mu\text{m}$ ) were purchased from Aldrich Chemical Company Inc (USA). Si nanoparticles (particle size  $\geq 70$  nm) were purchased from Nanostructured & Amorphous Materials, Inc. Ge (particle size: 70 - 120 nm) and Sn (particle size  $< 100$  nm) nanoparticles were purchased from SkySpring Nanomaterials. Aluminum foil was purchased from Pactogo Inc. (USA). Li hexafluorophosphate ( $\text{LiPF}_6$ ) (power, sealed under argon), ethylene carbonate (EC) (100%, sealed under argon), ethyl methyl carbonate (EMC) (100%, sealed under argon), spring, gasket, cases, cap, spacer were purchased from Ferro Corporation (USA). Separators (Celgard 2400) were supplied Celgard LLC (USA). All were used as-received without further purification.

### 2. Nanofiber preparations

A variable high voltage power supply (Gamma ES40P-20W/DAM) was used to apply a spinning voltage. Electrospinning solutions were loaded in a 10 ml syringe to which a stainless steel capillary metal - hub needle was attached. The inside diameter of the metal needle was 0.30 mm. The positive electrode of the high voltage power supply was connected to the needle tip. The grounded electrode was connected to a metallic collector covered with an aluminum foil. The tip-collector distance and flow rate were fixed at 15.5 cm and 1.0 ml/h, respectively. Under the high voltage, a polymer jet was ejected and accelerated toward

the counter electrode, during which the solvent was rapidly evaporated. Dry nanofibers were accumulated on the collection screen and collected as a fibrous mat.

The carbonization of PAN precursor nanofiber mats was performed in an atmosphere-controlled furnace (Model 7AM-C12, LUCIFER, Pennsylvania). Firstly, the electrospun nanofibers were heated to 280 °C at 5 °C min<sup>-1</sup> in air environment, and this temperature was maintained for several hours. In this process, thermoplastic PAN was converted to a non-plastic cyclic or ladder compound. The temperature was then increased from 280 °C to higher temperatures with a heating rate of 2 °C min<sup>-1</sup> in an inert atmosphere (high-purity argon) and held for one hour in order to complete the carbonization process.

The CVD process was carried out using an ASM 6" LPCVD with an operating temperature of 760 °C and an operating pressure of 10 Torr. Pure CH<sub>4</sub> gas was used as the carbon precursor with a flow rate of 200 sccm and deposited for 60 min in order to obtain thorough carbon deposition.

### 3. Nanofiber characterizations

The morphology and diameter of nanofibers were evaluated using scanning electron microscopy (JEOL 6400F FESEM at 20 kV). Electrospun samples were coated with Au/Pd layers of approximately 100 Å thickness by a K-550X sputter coater to reduce charging.

Transmission electron microscopy (TEM) with an accelerating voltage of 120 kV (Hitachi HF-2000 TEM at 200 kV) was used to study the structure of nanofibers attached on 400 mesh carbon coated Cu grids. High-resolution TEM with an accelerating voltage of 300kV (FEI Titan STEM) was also used to further study the morphology and composition of the as-prepared nanofibers.

X-ray diffraction (XRD) analysis was performed with Rigaku SmartLab X-Ray Diffraction System, Cu K $\alpha$ ,  $\lambda = 1.5405 \text{ \AA}$  in a range of 0 - 90°. The operating voltage and current were 40.0 kV and 60.0 mA, respectively. A crystal-monochromated collection system was used to acquire the diffractograms at 0.02 degree intervals at a rate of 1 s per step. Peak positions were determined by the APD 1700 (Version 4) software.

#### 4. Electrochemical evaluations

Electrochemical performance evaluations were performed using 2032 coin-type cells. The relatively thin, mechanically tough electrospun carbon nanofibers were prepared by a simple punching process after carbonization, and were attached onto copper foil (thickness is 25  $\mu\text{m}$ , Aldrich), and directly used as the working electrode. Li ribbon and Celgard 2400 separator were used as counter electrode and separator, respectively. The working electrode, separator, spring, gasket, cases, cap and spacer were placed in an oven at about 120 °C overnight under vacuum. Electrolyte used was 1 M LiPF<sub>6</sub>, dissolved in 1/1 (V/V) EC/ EMC (Ferro Corp.). The cells were assembled in a high-purity argon-filled glove box using a pressure crimper. Charge (Li insertion) and discharge (Li extraction) were conducted using an Land automatic

battery cycler (LAND CT2001A) between cut-off potentials of 0.01 and 2.0V, 2.5 V or 2.8 V with current density of 50 mAh g<sup>-1</sup>.

CHAPTER 4 HIGH-PERFORMANCE TIN/CARBON COMPOSITE ANODES DERIVED  
FROM TIN(II) ACETATE/POLYACRYLONITRILE PRECURSORS BY  
ELECTROSPINNING TECHNOLOGY

Abstract: Sn/carbon composite nanofibers with various compositions were prepared from Sn(II) acetate/polyacrylonitrile (PAN) precursors by a combination of electrospinning and carbonization methods, and their potential use as anode materials for rechargeable lithium-ion batteries was investigated. The composite electrode derived from 20 wt% Sn(II) acetate/PAN precursor showed excellent electrochemical properties, including a large reversible capacity of 699 mAh g<sup>-1</sup> and a high capacity retention of 83% in 50 cycles. Sn/carbon composite nanofibers exhibited enhanced electrochemical performance ascribing to the combination of the properties of both Sn nanoparticles (large Li storage capability) and carbon matrices (long cycle life), and therefore could be potentially used in high-energy rechargeable lithium-ion batteries.

Keywords: Tin, tin(II) acetate, composite nanofiber, electrospinning, lithium-ion battery.

## 1. Introduction

Lithium-ion batteries have large energy density, low cost and high safety, and hence they are being widely used in digital cameras, laptops and hybrid vehicles<sup>135</sup>. The first commercialization of lithium-ion batteries was by Sony in early 1990s with graphite as the anode material. Graphite provides a relatively low theoretical capacity of 372 mAh g<sup>-1</sup> and cannot meet the high energy density requirements of future large-scale energy storage devices<sup>114</sup>. To solve this problem, metallic or semiconducting materials with high theoretical capacities have been investigated aiming to improve the energy densities of lithium-ion batteries, e.g., Si (4200 mAh g<sup>-1</sup>), Ge (1900 mAh g<sup>-1</sup>), and Sn (992 mAh g<sup>-1</sup>)<sup>202</sup>. However, these high-capacity anode materials experience severe nanoparticle aggregation and large volume change during the lithium insertion and extraction process, which result in structural failure and quick capacity loss during charge and discharge cycles<sup>203</sup>.

To minimize the severe volume change of metallic or semiconducting materials during the lithium insertion and extraction process, many researchers focused on carbon-coating, nano-composite and porous structures<sup>204-207</sup>. Among the approaches, using carbon matrices, such as carbon particles<sup>119, 208, 209</sup>, carbon nanotubes<sup>210, 211</sup> and graphene<sup>212</sup>, to confine the anode nanostructure was found to be able to improve the cycle performance of metallic or semi conducting materials<sup>117</sup>. Recently, it has been reported that dispersing Sn nanoparticles into carbon nanofibers by electrospinning technique can result in less pulverization of Sn and thus more satisfactory electrochemical performance for lithium-ion batteries<sup>122, 133, 213</sup>.

Herein, we report the electrochemical performance of Sn/C nanofiber anodes derived from Sn(II) acetate/polyacrylonitrile (PAN) precursors of different concentrations. Sn(II) acetate is soluble in the PAN solution and could lead to a homogenous dispersion of Sn nanoparticles in the final Sn/C composite nanofiber anodes.

## 2. Experimental

PAN, Sn(II) acetate and solvent N,N-dimethylformamide (DMF) were purchased from Sigma Aldrich. Sn(II) acetate was added DMF solution of 8 wt% PAN to prepare spinning solutions at 60 °C. Sn(II) acetate concentrations used were 6, 10, 20 and 30 wt% (compared to PAN). In order to obtain homogeneous solutions, strong mechanical stirring combined with an ultrasonic treatment (FS20H Sonicator, Fisher Scientific) was applied for at least 48 h.

Electrospinning process was carried out with a flow rate of 1.0 ml h<sup>-1</sup>, needle-to-collector distance of 15.5 cm, and voltage of 15 kV. Electrospun Sn(II) acetate/PAN nanofibers were first stabilized in air at 280 °C for 5.5 h (heating rate: 5°C min<sup>-1</sup>) and then carbonized in argon at 800 °C for 1 h (heating rate: 2°C min<sup>-1</sup>) to obtain Sn/C nanofibers.

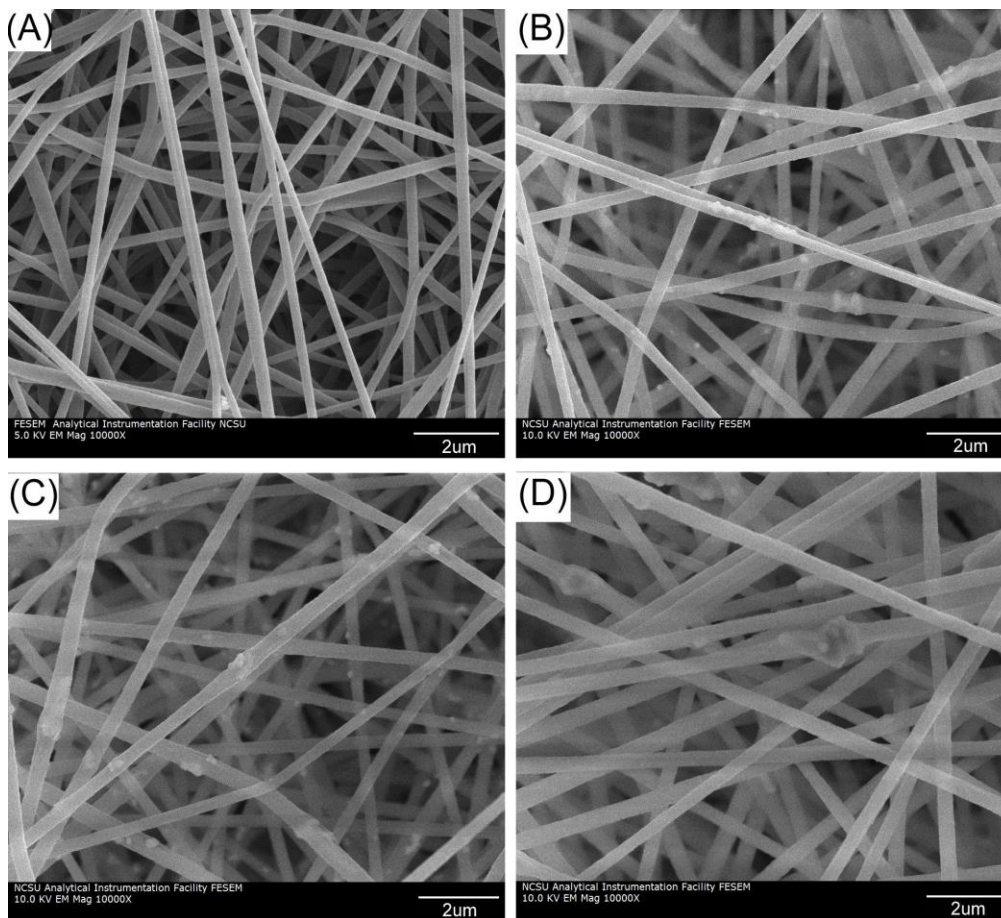
The morphology and diameters of Sn(II) acetate/PAN and Sn/C composite nanofibers were evaluated using scanning electron microscopy (JEOL 6400F Field Emission SEM at 5 kV). The structure variations of nanofibers were identified using trans-mission electron microscopy (Hitachi HF-2000 TEM at 200 kV) and X-ray diffraction (Rigaku SmartLab X-Ray Diffraction System, Cu K $\alpha$ ,  $\lambda$ = 1.5405 Å).

Electrochemical performance evaluations were performed using 2032 coin-type half cells. Sn/C composite nanofibers formed freestanding, conductive mats that were cut into the working electrode (diameter = 3/8 inch). The working electrode was vacuum-dried at 120 °C for 24 h, and then assembled with the lithium counter electrode in an argon-filled glove box. The electrolyte used was a 1 M LiPF<sub>6</sub> solution in ethylene carbonate (EC)/dimethyl carbonate (DMC) (1:1 v/v). Galvanostatic charge and discharge experiments were conducted using a battery testing system (LAND CT2001A) at a current density of 100 mA g<sup>-1</sup> between 0.01 and 2.80 V.

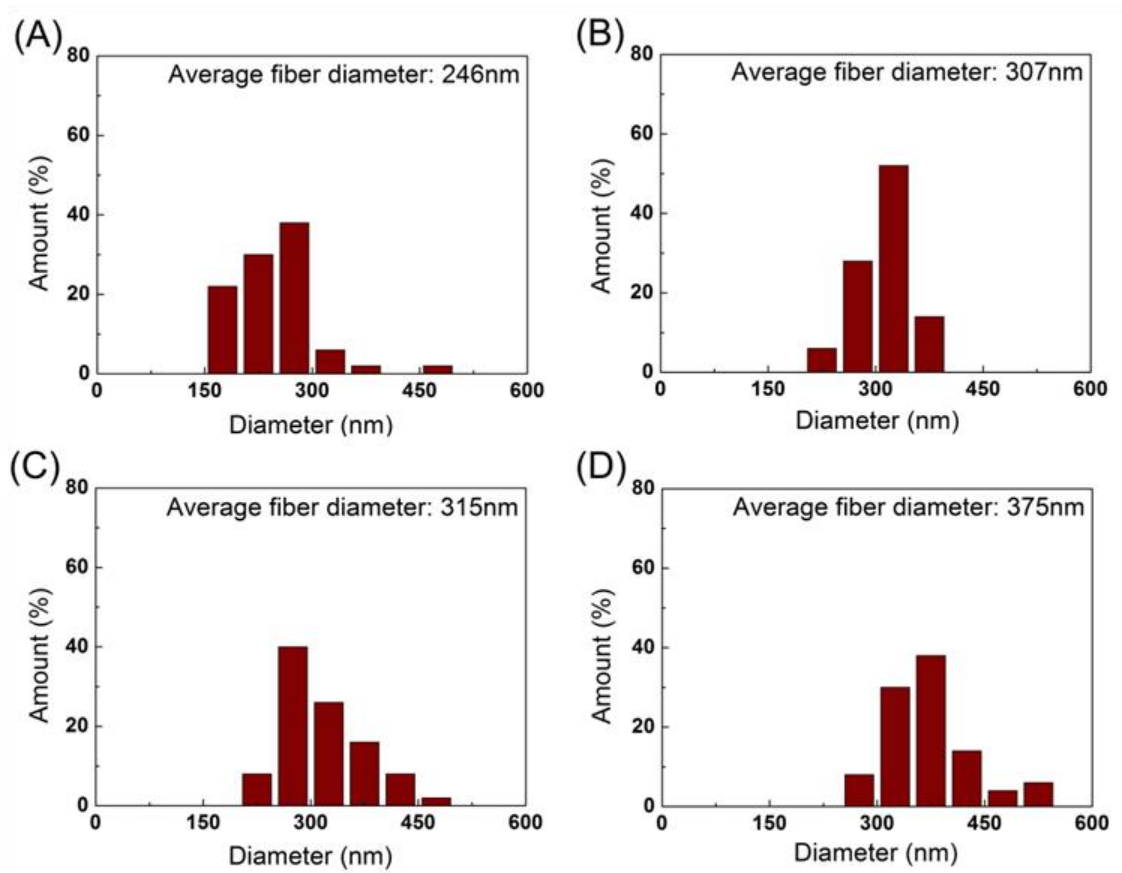
### 3. Results and discussion

#### 3.1 Morphology

Figure 4.1 show the morphology and fiber diameter distributions of 6%, 10%, 20% and 30% Sn(II) acetate/PAN nanofibers. The diameter distributions of these nanofibers are shown in Figure 4.2. The electrospun Sn(II) acetate/PAN nanofibers are continuous, homogeneously distributed, and exist in a reticular morphology. With increase in Sn(II) acetate concentration, more beads and irregularities occur. The average fiber diameters are 246, 307, 315 and 375 nm for 6%, 10%, 20% and 30% Sn(II) acetate/PAN nanofibers, respectively. The increase in fiber diameters mainly results from the increased solution viscosities at high Sn(II) acetate concentrations.



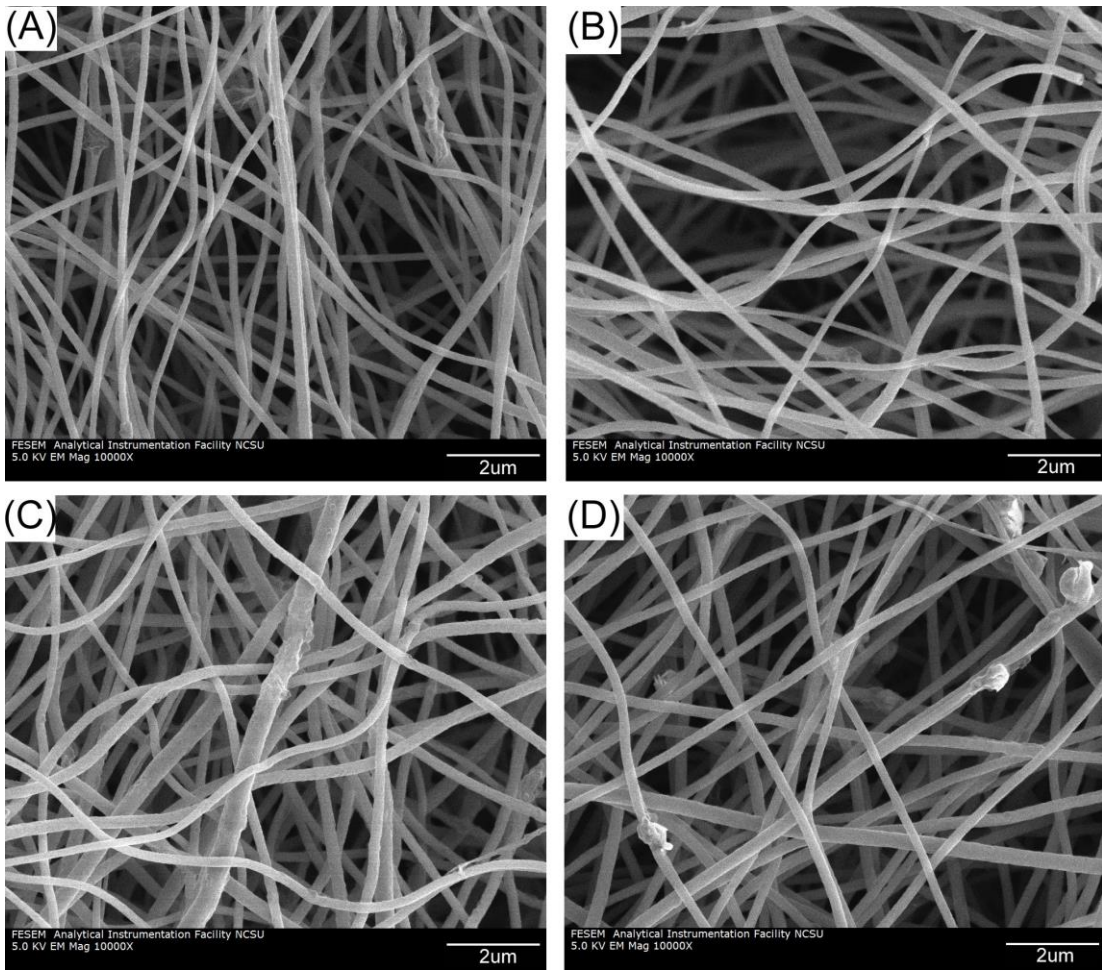
**Figure 4.1. SEM images of (A) 6%, (B) 10%, (C) 20%, and (D) 30% Sn(II) acetate/PAN nanofibers.**



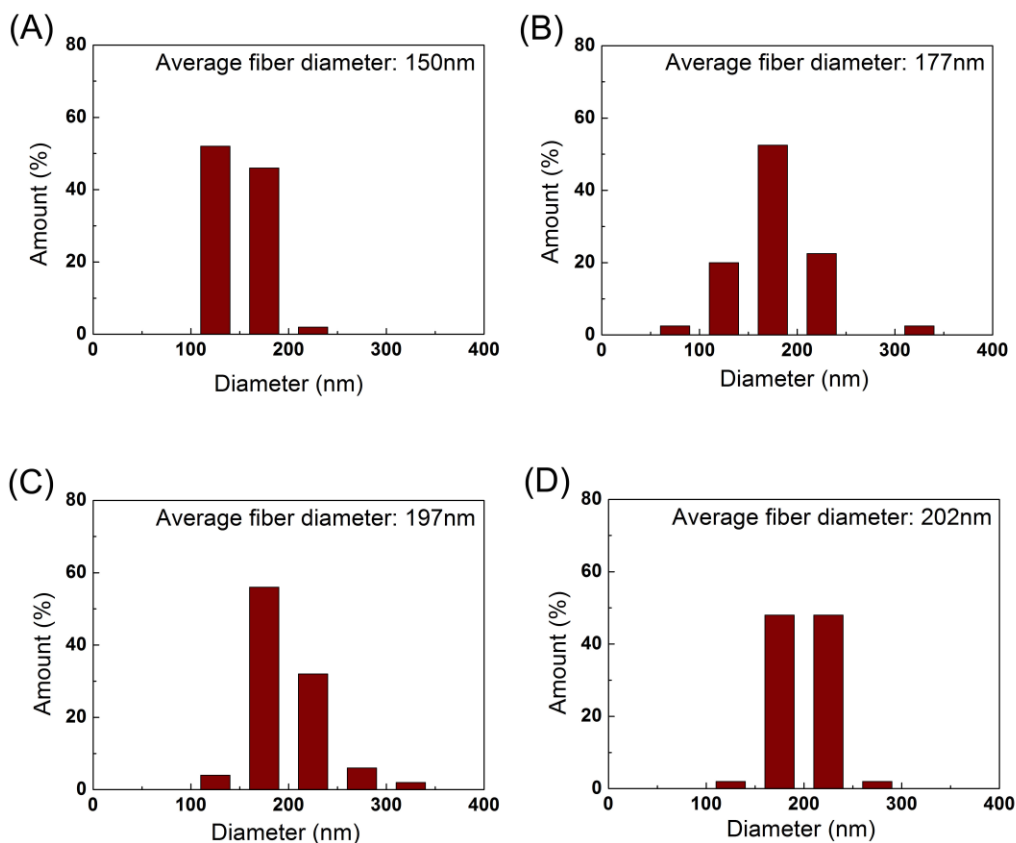
**Figure 4.2. Nanofiber diameter distributions of (A) 6%, (B) 10%, (C) 20%, and (D) 30% Sn(II) acetate/PAN nanofibers.**

Compared with Sn(II) acetate/PAN nanofibers, carbonized Sn/C composite nanofibers are more irregular and uneven (Figure 4.3). In addition, substantial fiber diameter decrease is observed due to the removal of acetate from the Sn(II) acetate salt and non-carbon element from PAN during the heat treatment process. Figure 4.4 shows that the average fiber diameter decreases to 150, 177, 197 and 202 nm for Sn/C composite nanofibers derived from 6%, 10%, 20% and 30% precursors, respectively. Similar to Sn(II) acetate/PAN nanofibers,

Sn/C composite nanofibers generate more beads and irregularities when the concentration of Sn(II) acetate precursor increases.

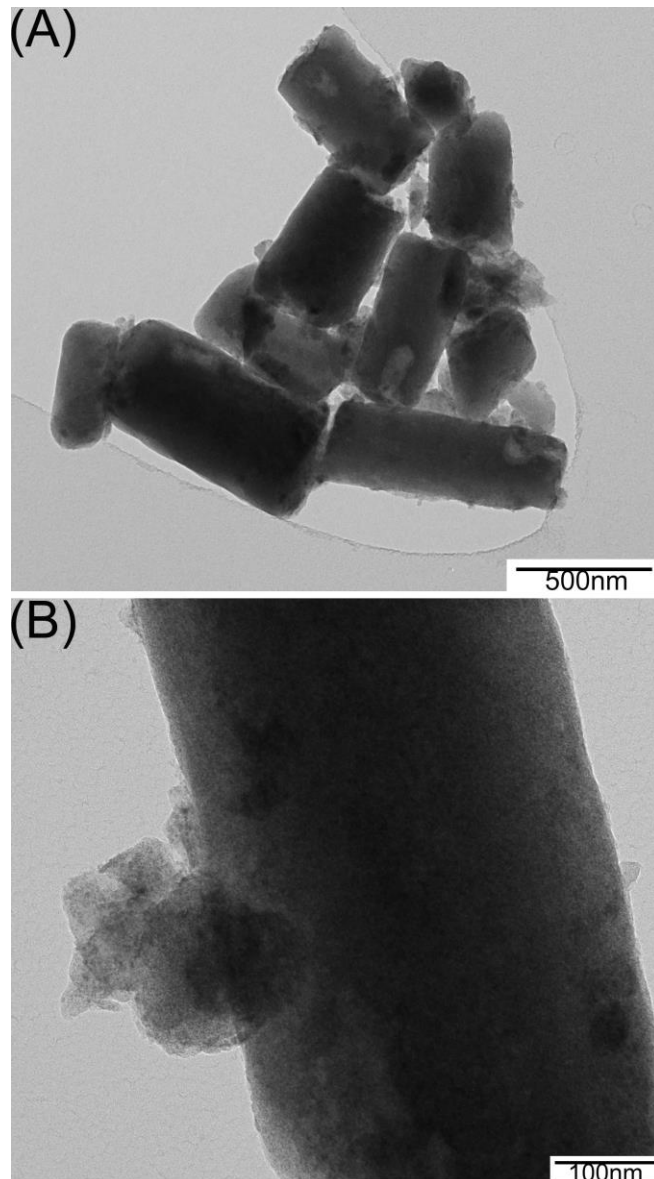


**Figure 4.3. SEM images of Sn/C nanofibers derived from (A) 6%, (B) 10%, (C) 20%, and (D) 30% precursors.**



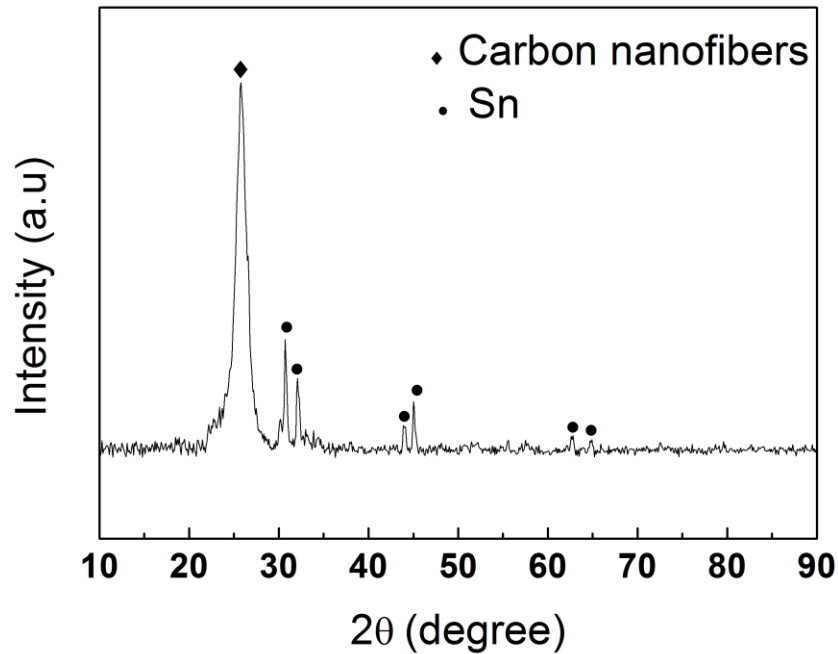
**Figure 4.4. Nanofiber diameter distributions of Sn/C nanofibers derived from (A) 6%, (B) 10%, (C) 20%, and (D) 30% precursors.**

Figure 4.5 exhibits TEM images of Sn/C nanofibers. Sn/C nanofibers were grounded to small pieces prior to TEM observation. Results indicate that Sn nanoparticles are formed and dispersed in the carbon matrix uniformly during the heat treatment process. The formation of metallic Sn is caused by the reducing environment created by the carbonization reactions. The average size of Sn particles is about 30 nm.



**Figure 4.5. Dark Field TEM images of Sn/C composite nanofibers derived from 20% precursor.**

The presence of Sn particles can also be observed from the XRD pattern of Sn/C composite nanofibers in Figure 4.6. Peaks at  $2\theta = 30.64, 32.03, 43.88, 44.91, 62.54, 64.60^\circ$  are ascribed to the (200), (101), (220), (211), (112), and (321) planes of tetragonal Sn (JCPDS card no. 04-0673). Good crystallinity of the Sn phase and high phase purity of the product are suggested by the sharp diffraction peaks. In addition, no peaks are found for SnO<sub>2</sub>, indicating all Sn(II) ions are reduced to metallic Sn. From Figure 4.6, a sharp carbon peak is also found at  $2\theta = 25.69^\circ$ , corresponding to the (002) plane of the highly ordered carbon material (JCPDS card no. 13-0148).



**Figure 4.6. XRD pattern of Sn/C composite nanofibers derived from 20% precursor.**

### 3.2 Electrochemical performance

Galvanostatic charge-discharge experiments were carried out at a current density of 100 mA g<sup>-1</sup> within a voltage window of 0.01 - 2.8 V to evaluate the electrochemical performance of Sn/C nanofiber anodes derived from 6, 10, 20 and 30% Sn(II) acetate/PAN precursors without adding any binder or conductive additive.

Figure 4.7 shows the galvanostatic charge-discharge profiles of the first, second and twentieth cycles of Sn/C nanofiber anodes, respectively. At the first cycle, Sn/C nanofiber anodes derived from 6, 10, 20 and 30% precursors show specific discharge capacities of 879, 984, 1002 and 1112 mAh g<sup>-1</sup>, and charge capacities of 515, 620, 699 and 782 mAh g<sup>-1</sup>, respectively. Higher Sn content leads to greater charge and discharge capacities since Sn has higher theoretical capacity than carbon. For Sn/C nanofibers, the discharge profiles of the first cycle consist of two segments: a plateau at around 0.9 V (0.7V for Sn/C anode derived from 6% precursor) and then a relatively slow voltage decrease. The plateau can be attributed to the decomposition of the electrolyte and the formation of solid electrolyte interface (SEI). It is noted that the Sn/C nanofiber anode derived from 6% precursor shows a similar charge-discharge characteristic to that of carbon nanofibers with a relatively low plateau of 0.7 V<sup>214</sup>. The second segment below the critical voltage is related to the complicated insertion of Li into Sn and carbon by forming Li<sub>4.4</sub>Sn and LiC<sub>6</sub> structures.

As shown in Figure 4.7B, the SEI plateau nearly disappears and results in significantly greater Coulombic efficiencies of about 97% at the second cycle. It is found that although the

capacities of Sn/C composite nanofiber anodes decrease slightly as compared to the first cycle, they still exhibit relatively high reversible capacities of 463, 554, 673 and 711 mAh g<sup>-1</sup>. In addition, in the second cycle, the charge-discharge curves of Sn/C anodes derived from 20% and 30% precursors become more close to each other and therefore the difference between the reversible capacities is smaller. Correspondingly, at the twentieth cycle (Figure 4.7C), the charge and discharge capacities of Sn/C anodes derived from 20% precursor are larger than those of Sn/C nanofiber anodes derived from 30% precursor. Though compared to Sn/C nanofiber anodes derived from 20% precursor, Sn/C nanofiber anodes derived from 30% precursor have more Sn particles and thus larger lithium acceptance ability, the pulverization of Sn caused by the large volume change (~ 300%) is more severe at this concentration and leads to reduced capacities.

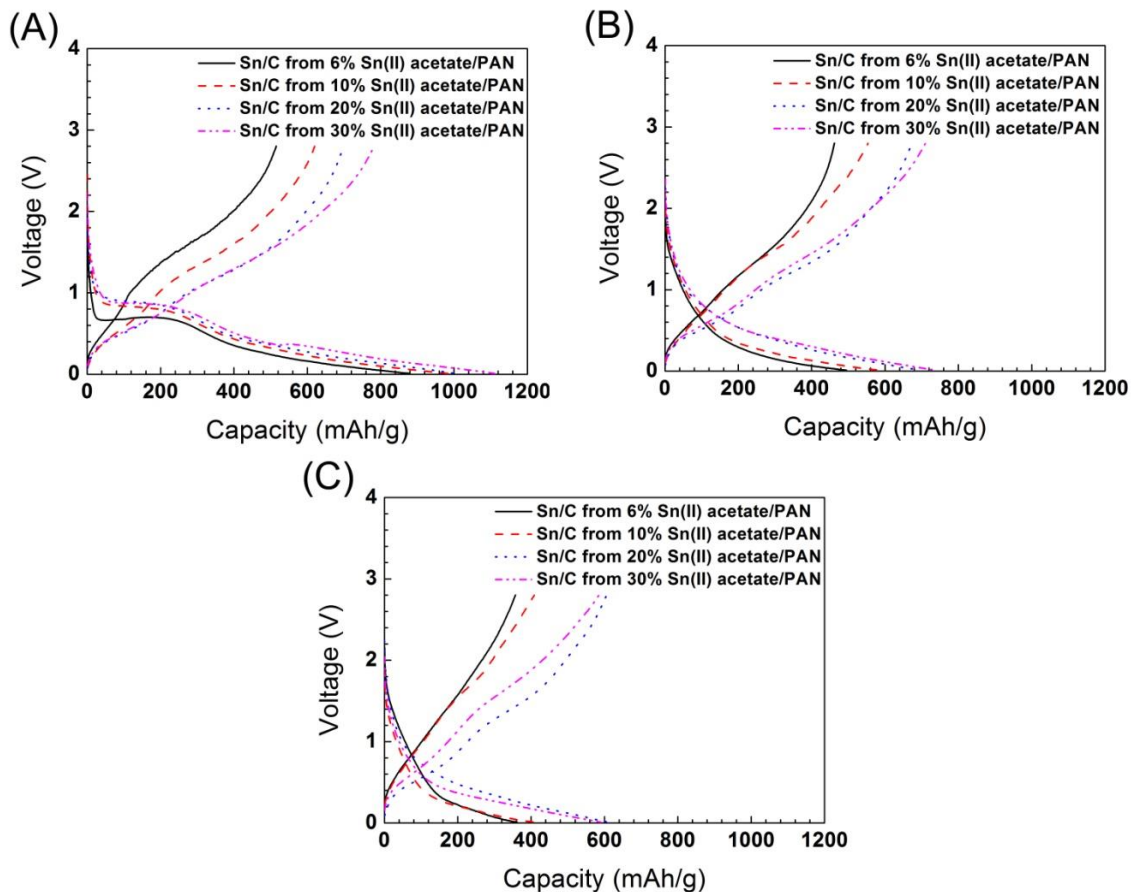


**Figure 4.7. Galvanostatic charge-discharge curves of (A) the first cycle, (B) the second cycle and (C) twentieth cycle of Sn/C nanofiber anodes derived from 6%, 10%, 20%, and 30% precursors. Current density:  $100 \text{ mA g}^{-1}$ . Carbonization temperature:  $800 \text{ }^\circ\text{C}$ .**

The cycling performance of Sn/C nanofiber anodes derived from 6, 10, 20 and 30% precursors is shown in Figure 4.8. The cycling performance of these Sn/C nanofiber anodes is of noteworthy stability. After 50 cycles, the charge capacities remain 348, 446, 576 and 495  $\text{mAh g}^{-1}$ , respectively, for Sn/C nanofiber anodes derived from 6, 10, 20 and 30%

precursors. These capacity values correspond to 68, 72, 83, and 64% capacity retention from the first-cycle values, which indicate a relatively slow capacity fading. As shown in Figure 4.8, Sn/C nanofiber anodes derived from 20% precursor demonstrate the most prominent electrochemical performance. It is believed that the increase in Sn content has at least two effects. On one hand, a higher Sn content leads to larger Li storage ability, i.e., higher charge and discharge capacities. On the other hand, the higher Sn content also causes larger Sn/C nanofiber diameters and more particle aggregations, which could promote the pulverization of the electrode structure and consequently jeopardize the cycling performance. Therefore, with increase in Sn content, both the charge capacity and capacity retention first increase and then reach the maximums when the Sn content is 20% in the precursor. With continuous increase in Sn content in precursor to 30%, both the charge capacity and capacity retention decrease. From Figure 4.8, it is also seen that the reversible capacity of the Sn/C anodes derived from 20% precursor at fiftieth cycle is still higher than those of other reported Sn/C nanofiber composite anodes<sup>122, 213</sup>. The improved cycling performance of Sn/C composite nanofibers can be explained that metallic nano-sized Sn is mainly distributed inside carbon nanofibers during carbonization process due to the use of Sn(II) acetate salt and thus carbon nanofibers as the confinement material can successfully restrain the huge volume change of Sn.

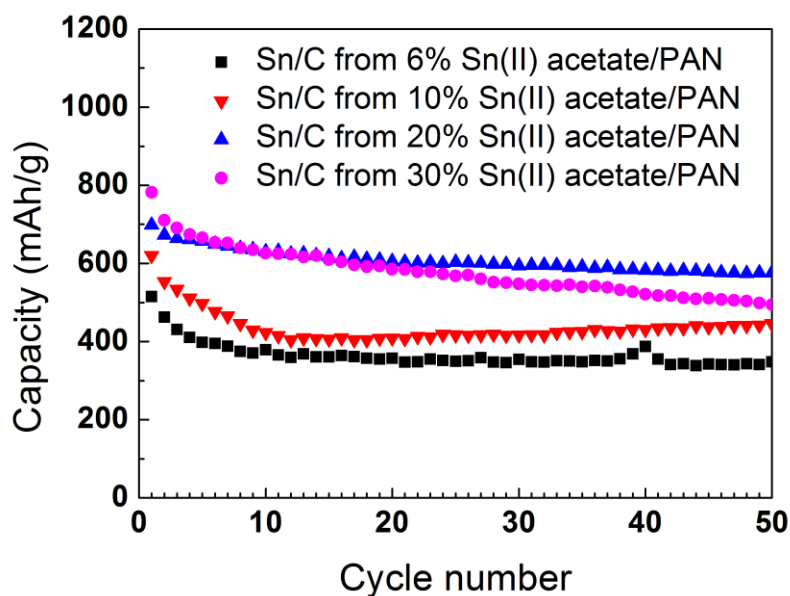


**Figure 4.8. Cycling performance of Sn/C nanofiber anodes derived from 6%, 10%, 20%, and 30% precursors. Current density:  $100 \text{ mA g}^{-1}$ . Carbonization temperature:  $800 \text{ }^\circ\text{C}$ .**

Figure 4.9 shows the Coulombic efficiencies of the first, second and twentieth cycles of Sn/C composite nanofiber anodes derived from 6, 10, 20 and 30% precursors. In the first cycle, the Coulombic efficiencies are 59, 64, 70 and 71%, as well as 94, 95, 97, 96% in the second cycle and almost 100% after the twentieth cycle. A Coulombic efficiency of less than 100% is mainly caused by the decomposition of the electrolyte and the formation of SEI film. The unstable SEI effect disappears and results in large Coulombic efficiencies for the Sn/C nanofiber anodes after the first cycle.

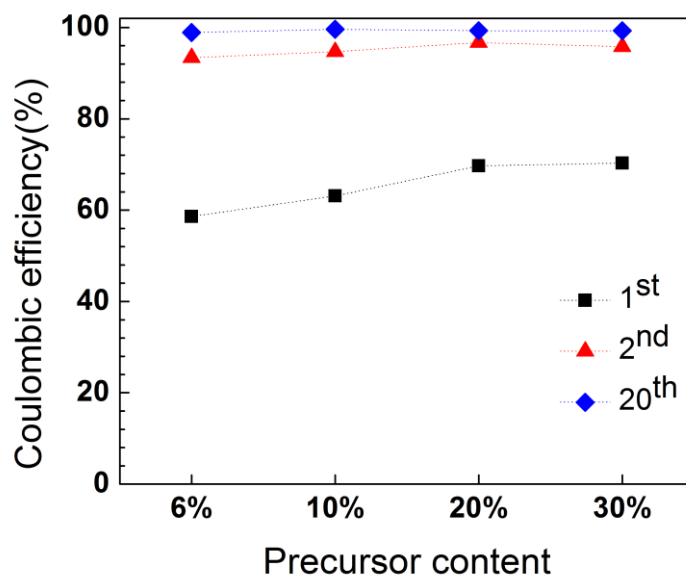


**Figure 4.9. Coulombic efficiencies of the first, second and twentieth cycles of Sn/C composite nanofiber anodes derived from 6%, 10%, 20%, and 30% precursors.**

The relatively good electrochemical performances of Sn/C composite nanofibers derived from Sn(II) acetate/PAN precursors can be attributed to their unique composite structure, such as the improved dispersion of Sn inside the nanofibers due to a soluble acetate, the unique one-dimensional fiber structure, and the shorter lithium ion diffusion distance in the nanofiber<sup>215</sup>.

#### 4. Conclusion

Sn/C composite nanofibers were prepared by electrospinning and the subsequent carbonization process with 6, 10, 20 and 30% Sn(II) acetate/PAN precursors. SEM results

show that with increase in Sn concentration, the surface morphology of the nanofibers becomes rougher probably due to increasing Sn aggregation in the fibers. However, the average diameter of Sn(II) acetate/PAN nanofibers decreases after heat treatment. The resultant Sn/C composite nanofibers were used as binder free anode materials for lithium-ion batteries and they exhibit relatively large reversible capacities and improved capacity retention. Among all anodes studied, Sn/C nanofiber anodes prepared from 20% Sn(II) acetate/PAN nanofiber precursor provide the largest Coulombic efficiency (~99.3%) and charge-discharge capacities during cycling due to relatively high Sn content and moderate volume change during lithium insertion and extraction process. Overall, the relatively good electrochemical performance of Sn/C nanofiber anodes is the result of the cooperative effects of homogeneously-distributed Sn material and the carbon matrix, as well as the unique one-dimensional nanofiber structure with large surface area and high length/diameter ratio.

CHAPTER 5 COMPARISON OF SILICON/CARBON, GERMANIUM/CARBON AND  
TIN/CARBON COMPOSITE NANOFIBER ANODES USED IN NEW-GENERATION  
LITHIUM-ION BATTERIES

Abstract: Alloy anodes (Si, Ge and Sn) electrospun into carbon nanofibers as binder-free electrodes were synthesized and studied for rechargeable lithium-ion batteries. Alloy anode materials suffered from serious volume changes and nanoparticle aggregations during lithium insertion and extraction, resulting in pulverization and capacity loss. Carbon nanofibers could help to preserve the alloy anode materials during repeated cycling, and consequently maintained the cycling stability. In this work, it was found that with increase in the amount of Si, Ge and Sn, the cycling stability was decreased due to the increasing large cluster quantity of nanoparticles within carbon nanofiber matrix. Compared with Si/C nanofibers, Ge/C and Sn/C exhibited better cycling performance due to better nanoparticle distribution and smaller volume changes. The reasons of the Si/C structure failure were explained in this article. It is believed that this study upon Si/C, Ge/C and Sn/C composite nanofiber electrodes could help designing alloy-based carbon composites with various structures for advanced lithium-ion batteries.

Keywords: Silicon, Germanium, Tin, composite nanofiber, nanoparticle aggregation, electrospinning, lithium-ion battery.

## 1. Introduction

In recent years, various materials have been employed to develop new generation of lithium-ion batteries with high energy and power densities for applications in portable electronic devices, electric vehicles, and emerging smart grids. There is currently significant research interest in the development of higher-capacity alternatives for the commercially used graphite anode, which has a relatively low theoretical specific capacity of  $372 \text{ mAh g}^{-1}$ ,<sup>100, 116</sup>. From the viewpoint of capacity, group IV elements are the most attractive since they can alloy with a large amount of lithium and exhibit high theoretical capacities. For example, Si, Ge and Sn can form  $\text{Li}_{4.4}\text{M}$  (M=Si, Ge, Sn) alloys and they show high theoretical specific capacities of 4300, 1600 and 991  $\text{mAh g}^{-1}$ , respectively<sup>73, 74, 99</sup>.

However, anodes based on high-capacity group IV elements suffer from large volume changes during lithium insertion and deinsertion, leading to decrepitation and loss of electrical contact in bulk electrodes<sup>216</sup>. Si has the largest known theoretical capacity, but undergoes a 400% change in volume<sup>65</sup>. Ge has a relatively lower theoretical capacity with a large volume change of 370%<sup>96</sup>. The fully lithiated  $\text{Li}_{4.4}\text{Sn}$  has the lowest theoretical capacity with a 259% volume expansion during the Sn alloying process<sup>129</sup>. To facilitate strain relaxation and improve electrode conductivity, which is gradually lost due to the large volume change, nanocomposites of Si, Ge and Sn with confinement-material carbon nanofibers have shown promising specific capacities and cyclability for use in lithium-ion batteries<sup>1, 72-74, 122</sup>. With flexible carbon nanofibers confining the structure, the loss of electronic contact caused by pulverization and insufficient binding is alleviated. Carbon

nanofibers have nanosized diameter and good conductivity, allowing efficient charge transport, both for Li ions from the electrolyte and electrons from the current collector. In addition, no binders or additives are needed during the battery production since these composite nanofibers form free-standing, flexible, and electrically-conductive mats that can be directly used as electrodes<sup>72, 74, 97</sup>.

In this study, we compared the morphology and electrochemical performance of Si/C, Ge/C and Sn/C composite nanofiber anodes produced from electrospinning and carbonization processes. Electrospinning is a simple, but versatile technique for processing nanofibers with or without nanoparticles of various geometries. During electrospinning, a polymer solution is fed by a syringe pump through a small capillary. A Taylor cone could be formed when the electrostatic force generated by a high voltage is balanced with the surface tension of the solution<sup>173</sup>. At a critical voltage, a charged jet is ejected and travels to the grounded collector, during which the jet undergoes whipping motions and finally forms a fiber mat<sup>165</sup>. In this work, the solution, a mixture of polyacrylonitrile (PAN), M (M=Si, Ge, Sn) and solvent N, N-dimethylformamide (DMF), was ejected and formed electrospun M/PAN composite nanofibers during electrospinning. Followed by a carbonization process, the electrospun M/PAN composite nanofibers could convert into M/carbon composite nanofibers. The resultant composite nanofiber mats feature relatively high porosity and large specific surface area which are used to alleviate the large volume change of M nanoparticles.

## 2. Experimental

PAN ( $M_w = 150,000$ ) and solvent DMF were purchased from Sigma Aldrich. Si, Ge, and Sn nanoparticles were purchased from SkySpring Nanomaterials, and their particle sizes are comparable: 70 - 120 nm. DMF solutions of PAN (8 wt%) containing different amounts of Si, Ge, and Sn nanoparticles (10, 30, and 50 wt% compared to PAN) were prepared at 60 °C. Mechanical stirring was applied for at least 24 h in order to obtain homogeneous dispersions of the nanoparticles.

To obtain composite nanofibers, a high-voltage power supply (Gamma ES40P-20W/DAM) was used to provide a voltage at around 15 kV during the electrospinning. Dry fibers were accumulated on the collector and formed fibrous mats. The electrospun Si/PAN, Ge/PAN and Sn/PAN nanofibers were firstly stabilized in air environment at 280 °C for 5.3 h (heating rate: 5 °C min<sup>-1</sup>), and then carbonized at 700 °C for 1 h in an argon atmosphere (heating rate: 2 °C min<sup>-1</sup>) to form Si/C, Ge/C and Sn/C nanofibers.

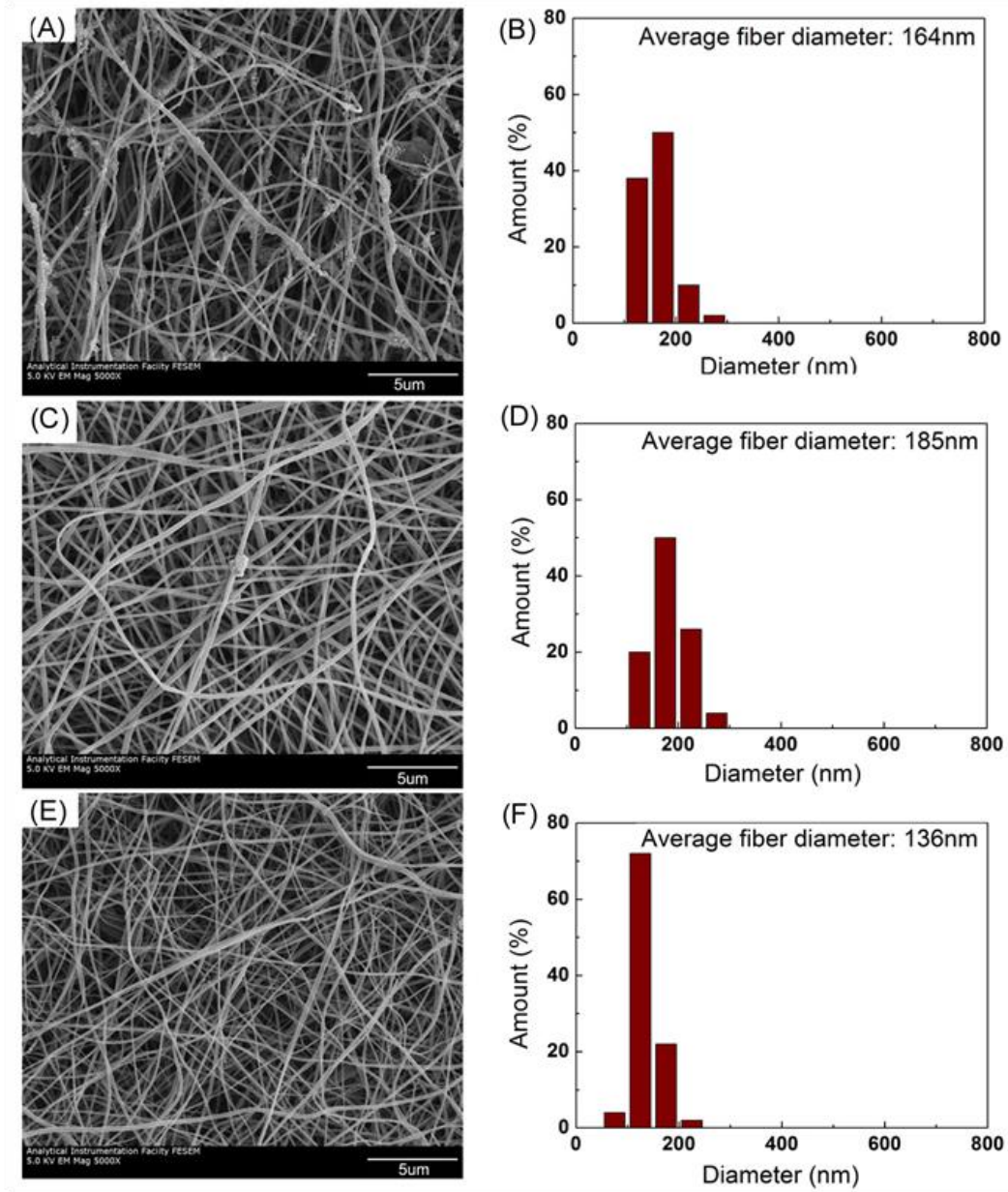
The morphology of the resultant Si/C, Ge/C and Sn/C nanofibers was observed with scanning electron microscope (SEM) (JEOL 6400F Field Emission SEM at 5 kV) and transmission electron microscopy (Hitachi HF-2000 TEM at 200 kV). Average fiber diameters and diameter distributions were calculated with 50 randomly selected fibers from SEM images. Electrochemical experiments were performed using coin-type half cells containing Si/C, Ge/C and Sn/C composite nanofibers as the working electrode and Li foil as the counter electrode. The working electrode was prepared by a simple punching process after

carbonization, and placed on copper foil. The electrolyte used was a 1 M LiPF<sub>6</sub> solution in ethylene carbonate (EC)/dimethyl carbonate (DMC) (1:1 v/v). The electrochemical performance was evaluated by carrying out galvanostatic charge-discharge experiments at 50 mA g<sup>-1</sup> between 0.01 and 2.0 V.

### 3. Results and discussion

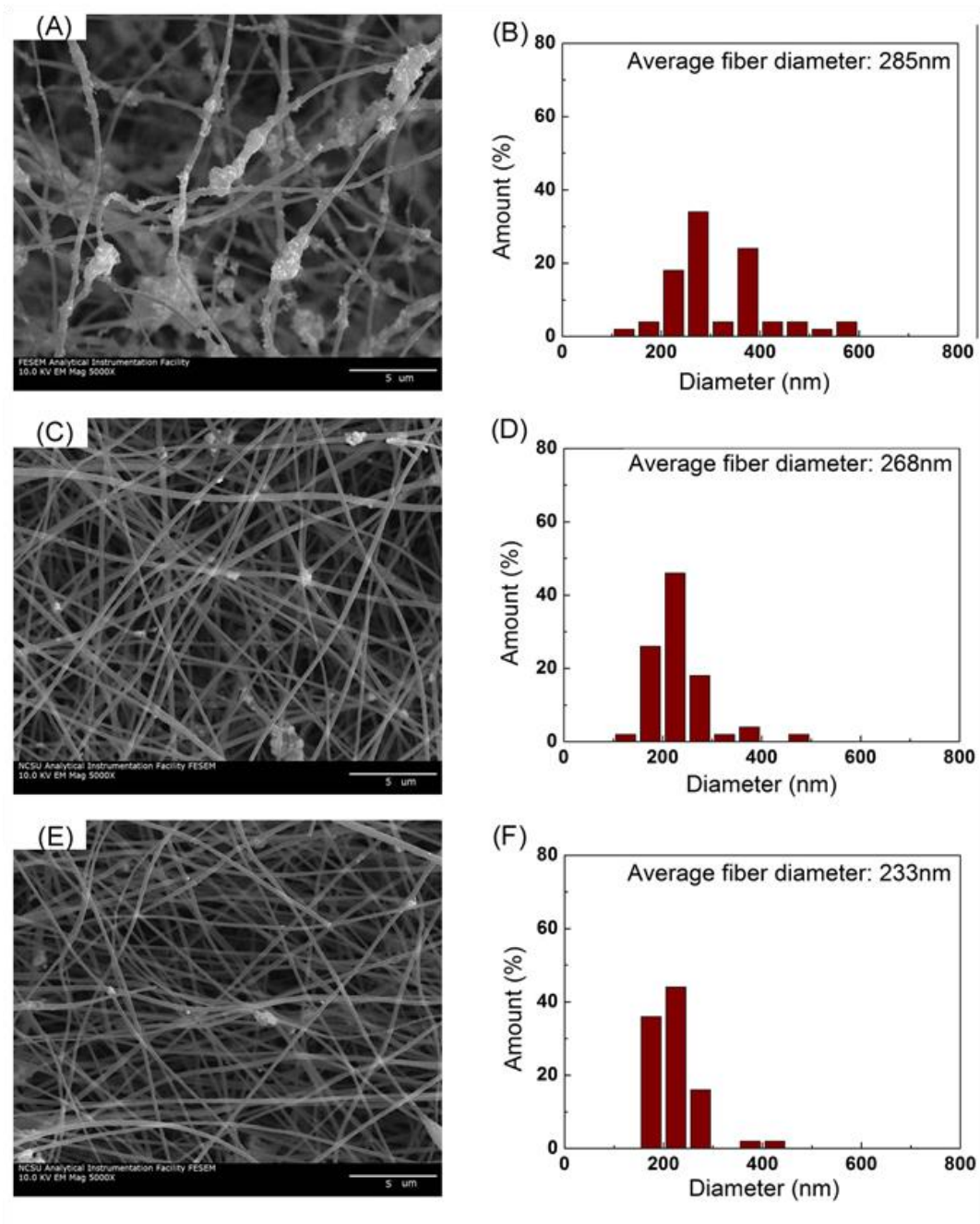
#### 3.1 Morphology

Figure 5.1 shows SEM images and diameter distributions of Si/C, Ge/C, and Sn/C nanofibers prepared from 10 wt% Si/PAN, Ge/PAN, and Sn/PAN precursors. The carbonized Si/C, Ge/C, and Sn/C nanofibers are homogeneously distributed, but slightly bent and wrinkled due to the removal of some species (such as CO<sub>2</sub>, HCN, and NH<sub>3</sub>, etc.) during heat treatment. The average fiber diameters of carbonized Si/C, Ge/C, and Sn/C nanofibers are 164, 185, and 136 nm, respectively. From Figure 5.1, it is also seen that with more particle aggregations, Si/C nanofibers show more mixed and irregular structures than Ge/C and Sn/C nanofibers. In other words, Ge/C and Sn/C nanofibers derived from 10 wt% Ge/PAN and Sn/PAN precursors exhibit relatively homogeneous distribution of Ge and Sn nanoparticles in the carbon nanofiber matrix. The difference in particle distribution may be due to the fact that Si is a semiconductor while Ge and Sn are metals. During electrospinning, electrically-conductive Ge and Sn nanoparticles mutually repulse each other and result in less particle aggregations than semi-conductive Si nanoparticles<sup>217</sup>.



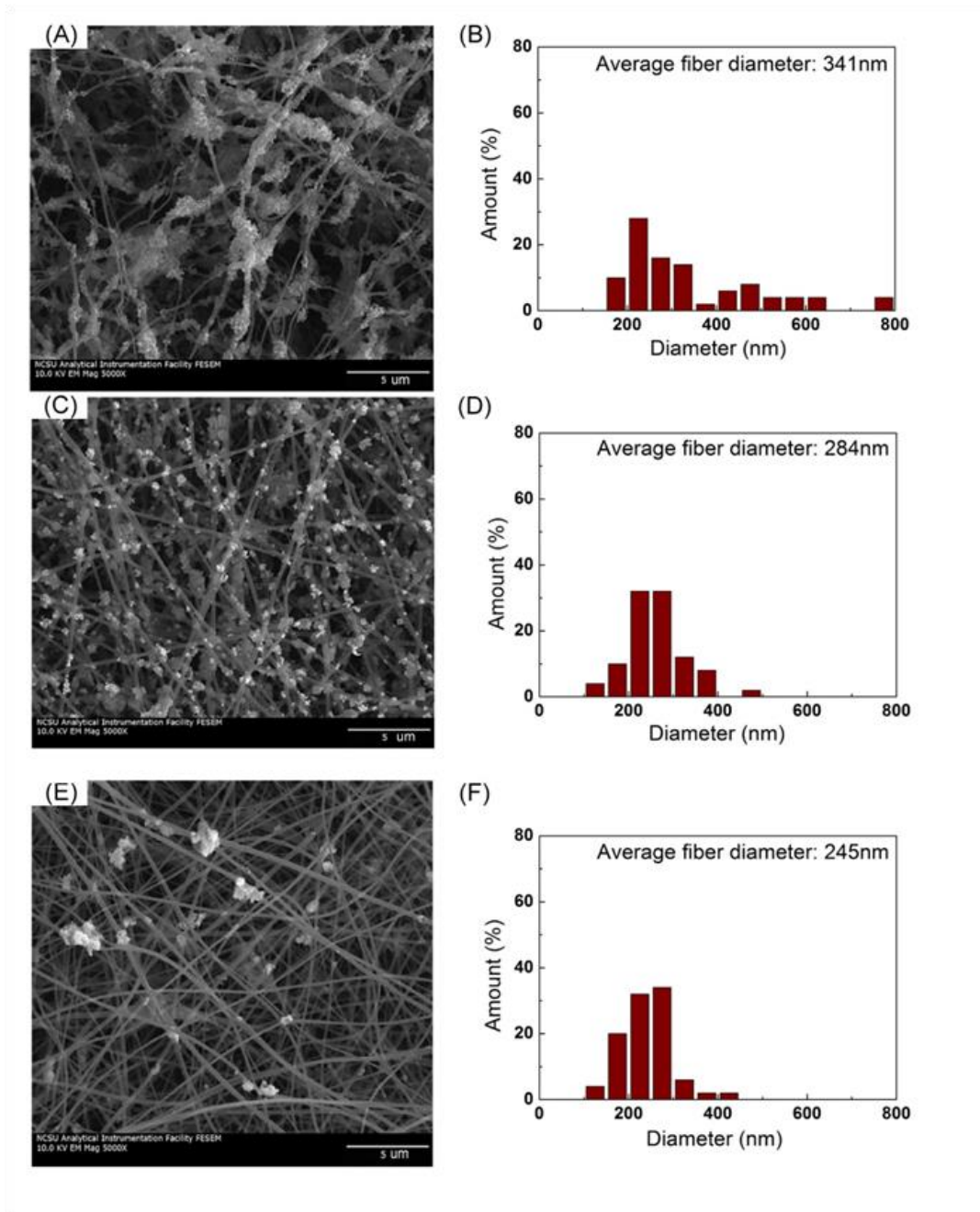
**Figure 5.1. SEM images and fiber diameter distributions of (A, B) Si/C, (C, D) Ge/C, and (E, F) Sn/C nanofibers prepared from 10 wt% Si/PAN, Ge/PAN, and Sn/PAN precursors, respectively.**

Figure 5.2 shows SEM images and diameter distributions of Si/C, Ge/C, and Sn/C nanofibers prepared from 30 wt% electrospun Si/PAN, Ge/PAN, and Sn/PAN precursors. Comparing Figures 5.1 and 5.2, it is seen that when the nanoparticle content increases from 10 to 30 wt% in precursors, composite nanofibers become rougher and more aggregations of nanoparticles can be seen from the fiber surfaces. Si/C nanofibers exhibit more uneven and wrinkled structures with larger particle aggregations. In addition, the diameters of the composite nanofibers increase to 285, 268, and 233 nm for Si/C, Ge/C, and Sn/C nanofibers, respectively. Increased nanoparticle content caused higher viscosities for the electrospinning solutions, and consequently caused higher diameters for the resultant nanofibers derived from 30 wt% precursors<sup>3, 218</sup>.



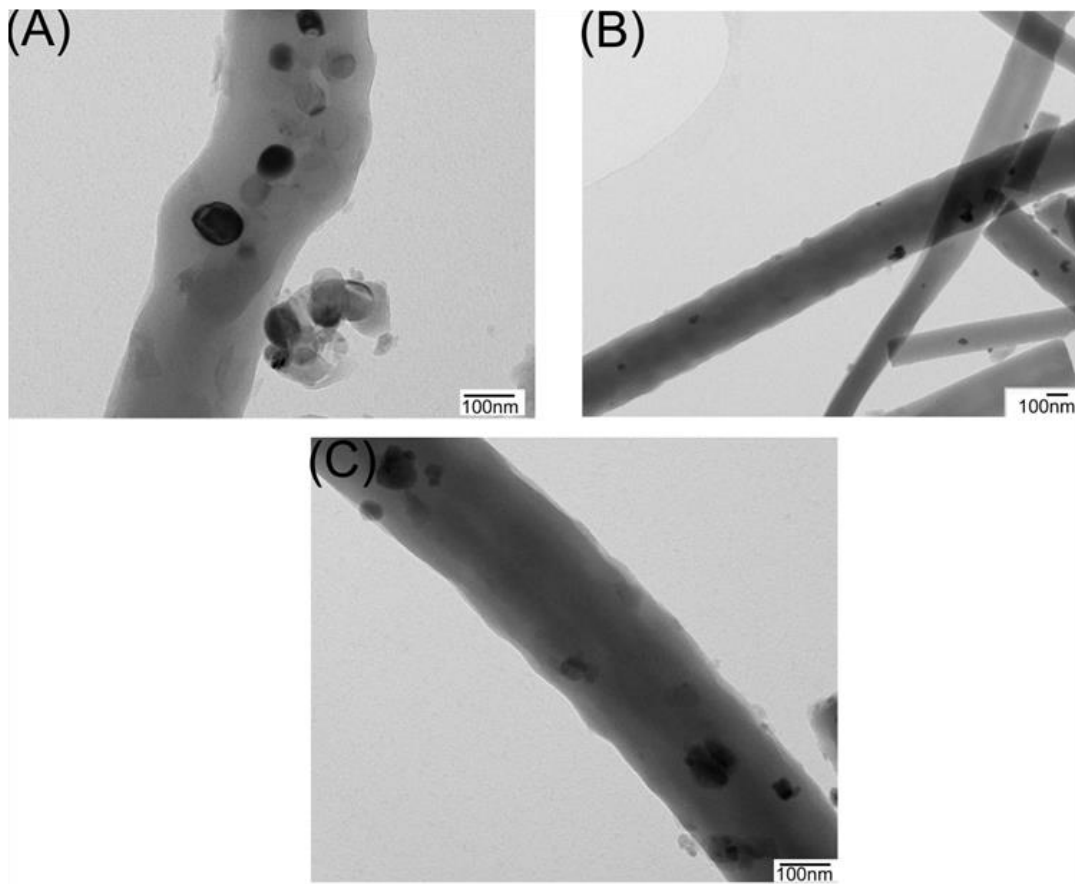
**Figure 5.2. SEM images and fiber diameter distributions of (A, B) Si/C, (C, D) Ge/C, and (E, F) Sn/C nanofibers prepared from 30 wt% Si/PAN, Ge/PAN, and Sn/PAN precursors, respectively.**

Figure 5.3 shows SEM images and diameter distributions of Si/C, Ge/C, and Sn/C nanofibers prepared from 50 wt% electrospun Si/PAN, Ge/PAN, and Sn/PAN precursors. With further increase in nanoparticle content to 50 wt% in precursors, Si/C, Ge/C and Sn/C composite nanofibers exhibit more aggregations of nanoparticles on the fiber surfaces. The average diameters of the composite nanofibers increase to 341, 284, and 245 nm for Si/C, Ge/C and Sn/C nanofibers, respectively, due to higher viscosities of the electrospinning solutions.



**Figure 5.3. SEM images and fiber diameter distributions of (A, B) Si/C, (C, D) Ge/C, and (E, F) Sn/C nanofibers prepared from 50 wt% Si/PAN, Ge/PAN, and Sn/PAN precursors, respectively.**

Figure 5.4 exhibits TEM images of Si/C, Ge/C, and Sn/C composite nanofibers prepared from 30 wt% Si/PAN, Ge/PAN, and Sn/PAN precursors, respectively. It is seen that Ge and Sn nanoparticles are distributed both inside and on the surface of carbon nanofibers. Some clusters around 100 - 200 nm are exhibited in the Si/C nanofibers, but no clusters are found in Ge/C and Sn/C nanofibers, indicating the good preservation of the discrete nature of the Ge and Sn nanoparticles. In other words, comparing Figures 5.4A, B and C, Si nanoparticles have poorer dispersion and more aggregations than Ge and Sn nanoparticles when dispersed in carbon nanofiber matrix by electrospinning.



**Figure 5.4. TEM images of (A) Si/C, (B) Ge/C, and (C) Sn/C nanofibers prepared from 30 wt% Si/PAN, Ge/PAN, and Sn/PAN precursors, respectively.**

Raman spectra of Si/C, Ge/C and Sn/C composite nanofibers derived from 30 wt% precursors are shown in Figure 5.5, and the results are consistent with typical disordered carbon materials<sup>219, 220</sup>. The strong peak centered near  $1350\text{ cm}^{-1}$  (D band) is indicative of defect-induced structures in the carbon materials, while the peak centered near  $1590\text{ cm}^{-1}$  (G band) can be explained as the high-frequency E<sub>2g</sub> first-order graphitic crystallites<sup>221-223</sup>. The ratios ( $I_D/I_G$ ) of the D band and G band intensities of Si/C, Ge/C and Sn/C composite

nanofibers are 1.12, 1.10 and 1.14, respectively, which are larger than 1.00, indicating the presence of a large amount of disordered structures or defects in the carbon matrix.

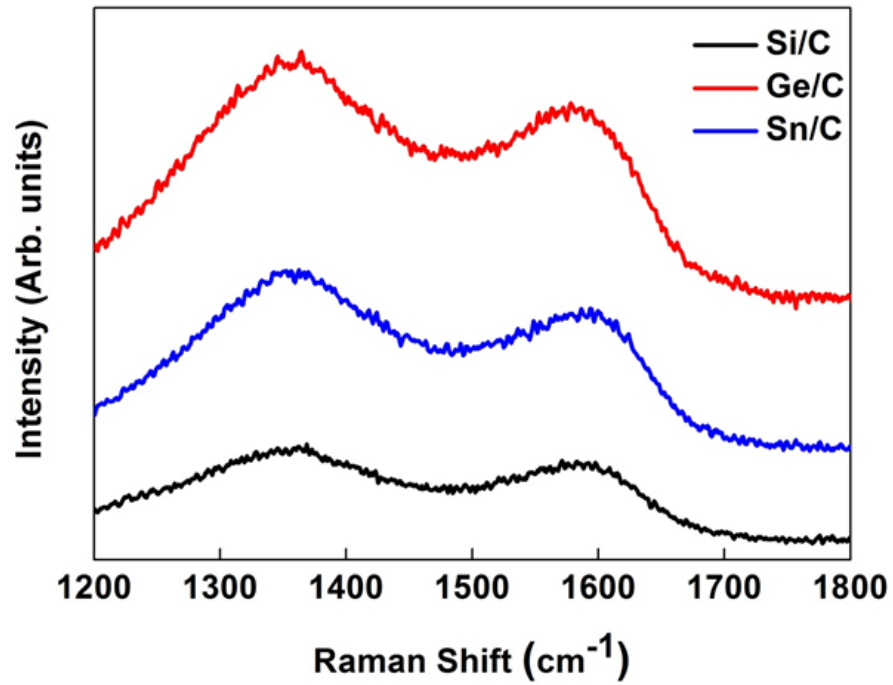


**Figure 5.5.** Raman spectra of Si/C, Ge/C, and Sn/C nanofibers prepared from 30 wt% precursors, respectively.

### 3.2 Electrochemical performance

Galvanostatic charge-discharge experiments were carried out at a current density of  $50 \text{ mA g}^{-1}$  within a voltage window of 0.01 - 2.00 V to evaluate the electrochemical performance of Si/C, Ge/C and Sn/C nanofiber anodes derived from 10, 30, and 50 wt% precursors.

Figure 5.6 shows the galvanostatic charge-discharge curves of the first, second and twentieth cycles of Si/C, Ge/C and Sn/C nanofibers derived from 10 wt% precursors, respectively. For the first cycle, the voltage of all three nanofibers drops rapidly during the discharge process from 2.00 V to about 0.68, 0.73 and 0.83 V, respectively, followed by a small plateau and a sloping line smoothly downshifting to 0.01 V. This small plateau is known as the result of the decomposition of electrolyte solution and the formation of the solid electrolyte interface (SEI), which covers the electrode surface and hinders the electrolyte from further decomposition<sup>72, 86</sup>. In the second cycle, the plateau disappears, indicating a stable SEI has been formed. From Figure 5.6, it is also seen that Si/C nanofibers have larger Li storage capacities than Ge/C and Sn/C nanofibers. For example, in the first cycle, Si/C, Ge/C and Sn/C nanofibers show initial specific discharge capacities of 1390, 1225, and 1310  $\text{mAh g}^{-1}$ , and initial charge capacities of 915, 640, and 650  $\text{mAh g}^{-1}$ , respectively. The initial irreversible capacities can be mainly ascribed to the formation of the SEI film during the first cycle<sup>72, 86, 224-226</sup>. In the second cycle, the discharge capacities of Si/C, Ge/C, and Sn/C nanofibers are about 880, 605, and 615  $\text{mAh g}^{-1}$ , and their charge capacities are 830, 565, and 565  $\text{mAh g}^{-1}$ , respectively. Si/C nanofibers still exhibit the highest Li storage ability among the three nanofiber anodes due to the largest theoretical capacity of Si. Compared to the first

cycle, the charge and discharge capacities in the second cycle are slightly lower. It is believed that the capacity loss is the consequence of the volume expansion during the formation of  $\text{Li}_x\text{Si}$ ,  $\text{Li}_x\text{Ge}$  and  $\text{Li}_x\text{Sn}$  alloys and subsequent detachment of Si, Ge and Sn particles from the structure. Similar results can be also found in the twentieth cycle. Compared to the second cycle, the relatively small differences of the capacities between the second cycle and the twentieth cycle indicate that the Si/C, Ge/C, and Sn/C composite structures result in a stable cycleability during their lithiation and delithiation processes.

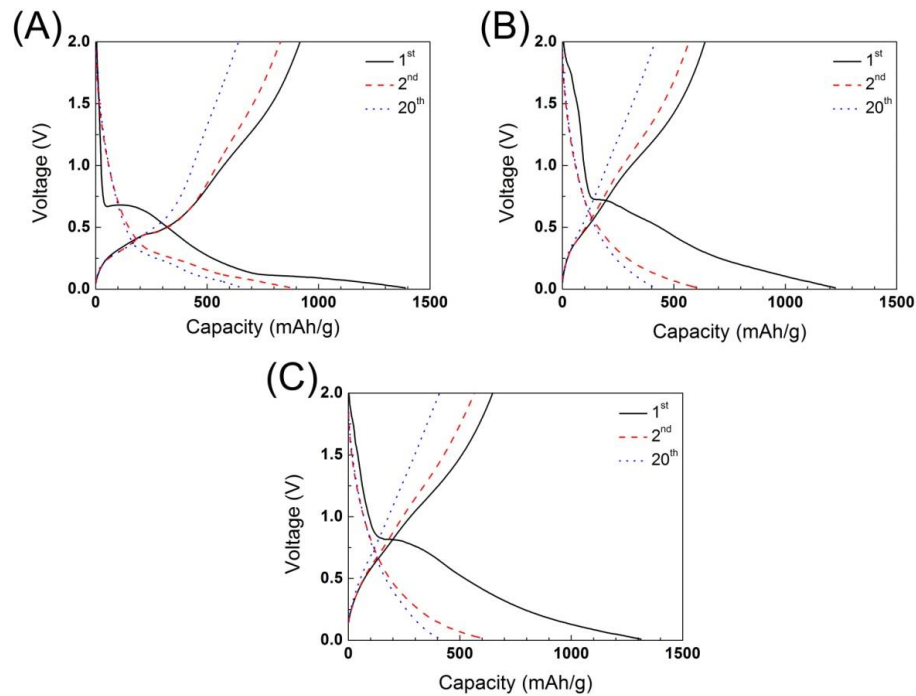


**Figure 5.6. Galvanostatic charge-discharge curves of the first, second and twentieth cycles of (A) Si/C, (B) Ge/C, and (C) Sn/C nanofibers prepared from 10 wt% precursors.**

From Figure 5.7, it is seen that Si/C, Ge/C and Sn/C nanofibers prepared from 30 wt% precursors show specific discharge capacities of 1760, 1385, 1260 mAh g<sup>-1</sup>, and charge capacities of 1380, 810, and 750 mAh g<sup>-1</sup>, respectively. These capacities are greater than those of nanofibers prepared from 10 wt% precursors since more Si, Ge and Sn nanoparticles are added. Besides, among these three nanofibers, Si/C composite nanofibers still exhibit the largest charge and discharge capacities since Si has the largest Li storage capability. Similarly, when the nanoparticle content further increases to 50 wt% in precursors (Figure 5.8), the discharge capacities increase to 2125, 1685 and 1410 mAh g<sup>-1</sup>, and the charge capacities increase to 1462, 880 and 805 mAh g<sup>-1</sup>, respectively.

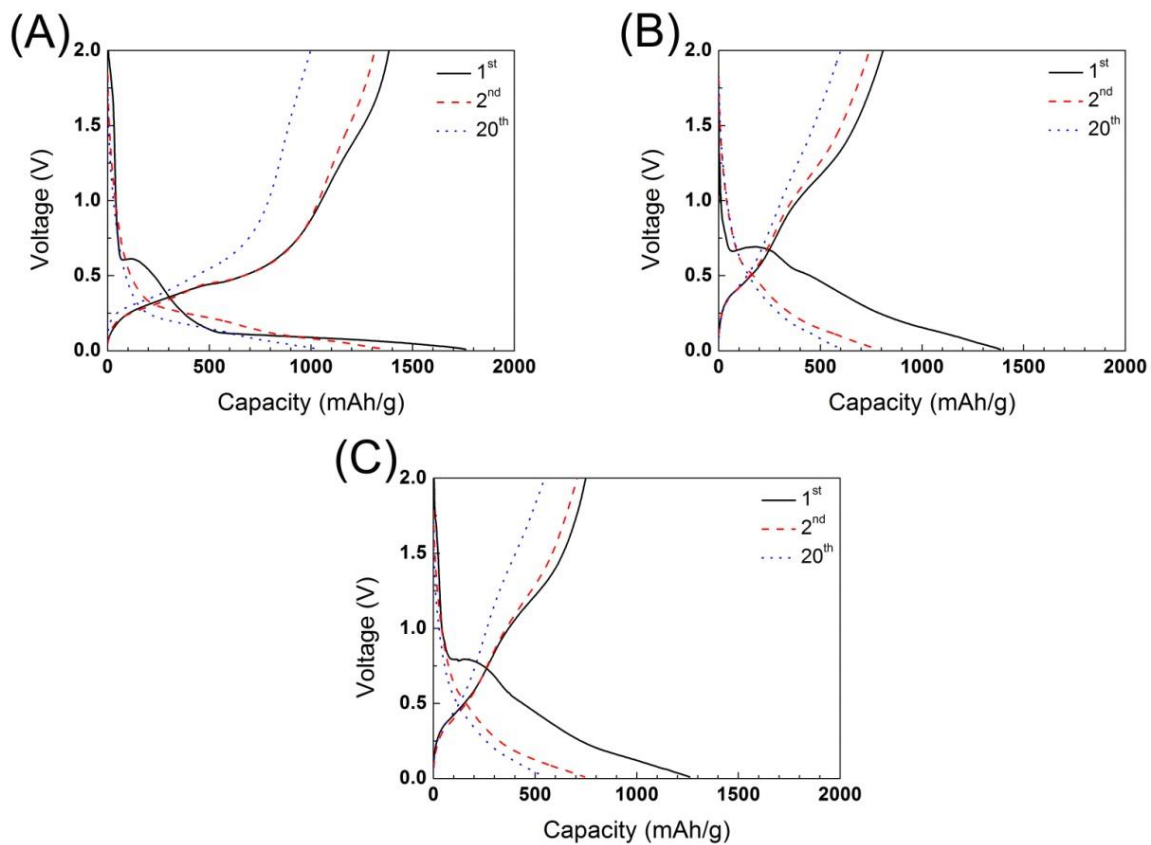


**Figure 5.7. Galvanostatic charge-discharge curves of the first, second and twentieth cycles of (A) Si/C, (B) Ge/C, and (C) Sn/C nanofibers prepared from 30 wt% precursors.**

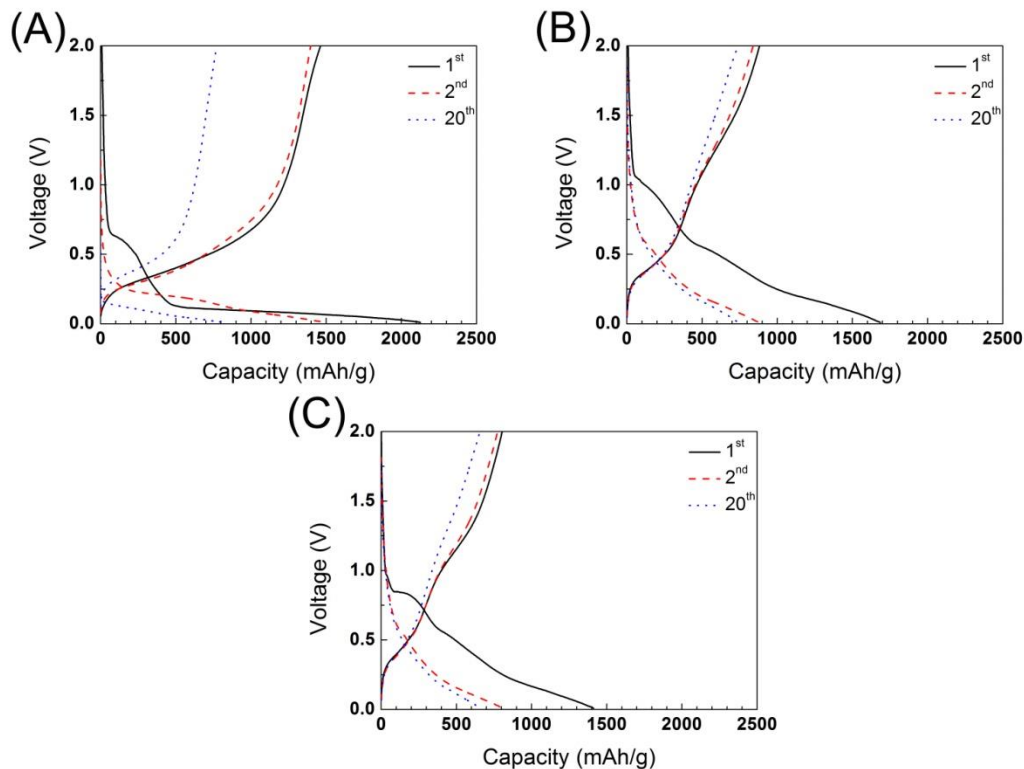


**Figure 5.8. Galvanostatic charge-discharge curves of the first, second and twentieth cycles of (A) Si/C, (B) Ge/C, and (C) Sn/C nanofibers prepared from 50 wt% precursors.**

Figure 5.9 presents the Coulombic efficiencies of Si/C, Ge/C, and Sn/C nanofibers prepared from 10, 30, and 50 wt% precursors. The initial Coulombic efficiencies of Si/C, Ge/C, and Sn/C nanofiber anodes prepared from 10 wt% Si/PAN, Ge/PAN, and Sn/PAN precursors are 66%, 53% and 50%, respectively. The relatively low Coulombic efficiencies in the first cycle are due to the decomposition of the electrolyte and formation of the SEI film. At the second cycle, a stable SEI film forms and results in large Coulombic efficiencies of the Si/C, Ge/C,

and Sn/C nanofibers, which are 95%, 94% and 92%, respectively. After 5 cycles, the Coulombic efficiencies of all three nanofibers are stabilized at around 98%. As for Si/C, Ge/C, and Sn/C nanofibers prepared from 30 wt% precursors, the initial Coulombic efficiencies are 79%, 59% and 60%, respectively, while those of nanofibers prepared from 50 wt% precursors are 69%, 53% and 57%, respectively. As shown in Figure 5.9, the first-cycle Coulombic efficiencies of Si/C nanofibers are much larger than those of Ge/C and Sn/C, this can be explained by their charge/discharge profiles (Figure 5.6). It is seen that all three nanofibers have two distinct intercalation processes, a potential plateau at 100 mV and another obvious step can be observed between 0.80 and 0.10 V, in which the passivation film, also known as the SEI, is formed by the irreversible reduction of electrolyte on the surface of the active material. From Figure 5.6 we can see that this process for Si/C nanofibers is shorter than the Ge/C and Sn/C nanofibers, resulting in higher Coulombic efficiencies.

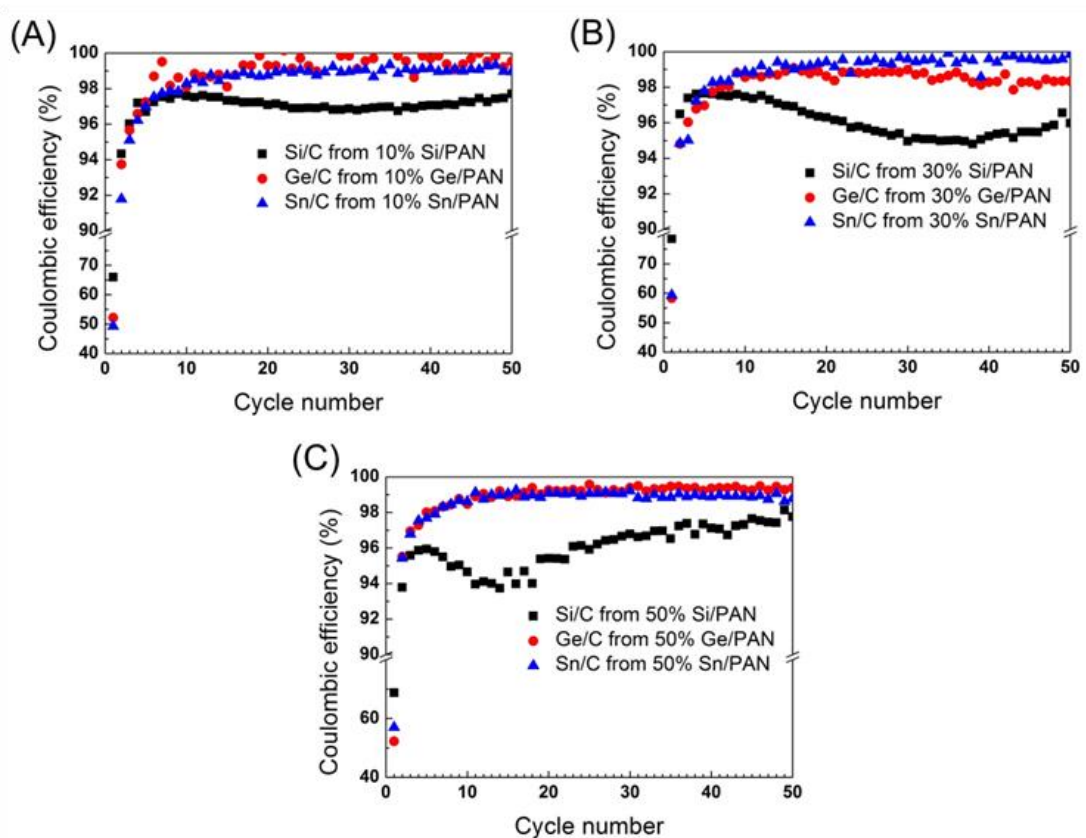


**Figure 5.9. Coulombic efficiencies of Si/C, Ge/C, and Sn/C nanofiber anodes prepared from (A) 10, (B) 30, and (C) 50 wt% precursors.**

The cycling performance of Si/C, Ge/C and Sn/C nanofibers is shown in Figure 5.10. It is seen that the cycling of Ge/C and Sn/C nanofibers is more stable than that of Si/C nanofibers, which is independent on the nanoparticle content. The significant capacity loss of Si/C nanofibers is mainly caused by the large Si nanoparticle agglomeration and severe volume change of Si particles during lithium insertion and distraction. The enormous agglomeration and volume change of the Si nanoparticles lead to severe particle separation and loss of

effective particle-particle electronic contacts<sup>74</sup>. On the other hand, both Ge and Sn nanoparticles experience less nanoparticle aggregations and smaller volume change upon repeated lithium insertion and extraction, and hence Ge/C and Sn/C nanofibers exhibit better cycling performance. The relatively good cycling performance of Ge/C and Sn/C composite nanofiber anodes derived from 10, 30 and 50 wt% Ge/PAN and Sn/PAN precursors may also be attributed to their unique one-dimensional carbon nanofiber structure with effective confinement of the severe volume change, increased conductivity and shorter lithium ion diffusion distance in the nano-sized fibers<sup>215</sup>.

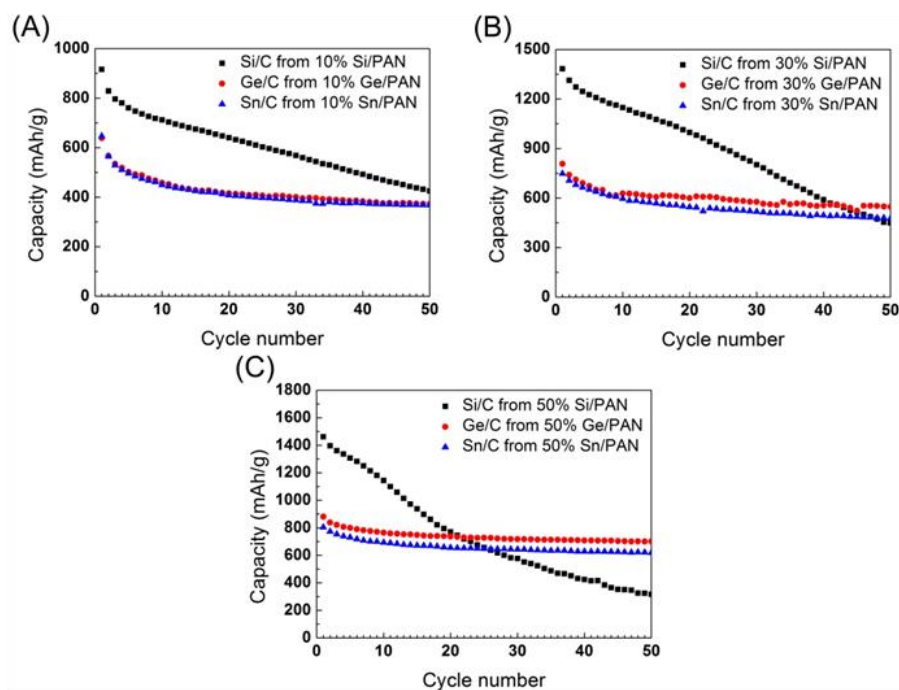


**Figure 5.10. Cycling performance of Si/C, Ge/C, and Sn/C nanofiber anodes prepared from (A) 10, (B) 30, and (C) 50 wt% precursors.**

#### 4. Conclusion

Si/C, Ge/C and Sn/C composite nanofibers with different nanoparticle contents were prepared by electrospinning and the subsequent carbonization process. SEM results show that with increase in nanoparticle content, the surface morphology of the fibers becomes rougher and uneven because of the increasing aggregation of nanoparticles. The resultant composite nanofibers were used as anodes for lithium-ion half cells and they exhibited relatively large reversible capacities and good cycle performance. Comparing Si/C, Ge/C and Sn/C composite anodes, Si/C nanofibers provided the largest initial Coulombic efficiency due to the least effect of SEI. However, Ge/C and Sn/C anodes presented better cycling performance than Si/C anodes due to better distribution in the carbon nanofibers and smaller volume change during lithium insertion and distraction processes. Results demonstrate that confining alloy anode materials into electrospun carbon nanofibers is a promising approach to obtain binder-free, high-capacity anodes for high-performance rechargeable lithium-ion batteries.

## CHAPTER 6 COBALT OXIDE/CARBON COMPOSITE NANOFIBERS FOR USE AS ANODE MATERIAL IN ADVANCED LITHIUM-ION BATTERIES

Abstract:  $\text{Co}_3\text{O}_4$ /carbon composite nanofibers were prepared by a combination of electrospinning and carbonization methods using 10 - 30 nm and 30 - 50 nm  $\text{Co}_3\text{O}_4$  nanoparticles, respectively, and their potential use as the anode material in rechargeable lithium-ion batteries was investigated. The composite  $\text{Co}_3\text{O}_4$ /carbon nanofiber electrode containing 30 - 50 nm  $\text{Co}_3\text{O}_4$  nanoparticles showed large reversible capacities and good cycleability with charge capacities of 677 and 545 mAh  $\text{g}^{-1}$  at the second and twentieth cycles, respectively. In contrast, the composite  $\text{Co}_3\text{O}_4$ /carbon nanofiber electrode containing 10 - 30 nm  $\text{Co}_3\text{O}_4$  nanoparticles showed fast capacity fading during cycling due to severe nanoparticle aggregation. Results suggested that the good electrochemical performance of  $\text{Co}_3\text{O}_4$ /carbon nanofiber electrode containing 30 - 50 nm  $\text{Co}_3\text{O}_4$  nanoparticles was ascribed to the combination of the properties of both  $\text{Co}_3\text{O}_4$  nanoparticles (large Li storage capability) and carbon nanofiber matrix (long cycle life), and therefore this electrode material could be potentially used in high-energy rechargeable lithium-ion batteries.

Keywords: Cobalt oxide, composite nanofiber, nanoparticle aggregation, electrospinning, lithium-ion battery.

## 1. Introduction

Lithium-ion batteries are considered as promising energy storage devices due to their eco-friendliness, low cost, large specific energy storage ability<sup>74, 227, 228</sup>. They are playing increasingly important role in wireless communication devices, hybrid electric vehicles, and emerging smart grids<sup>1</sup>. In order to meet the growing application requirements of novel energy storage, numerous materials and structures are thoroughly investigated in order to find new electrode materials with superior Li storage ability, improved cycleability, and lower cost.

Among various electrode materials, transition metal oxide tricobalt tetraoxide ( $\text{Co}_3\text{O}_4$ ) has received significant attention due to its relatively high theoretical specific capacity of  $890 \text{ mAh g}^{-1}$ , low electrode potential, high Columbic efficiency, long cycle life, and high level of safety<sup>229, 230</sup>. However,  $\text{Co}_3\text{O}_4$  electrodes suffer from large initial irreversible capacity loss, low electrical conductivity, and poor cycling stability that is related to the severe particle aggregations and relatively large volume change during lithium insertion/extraction process<sup>152, 229-231</sup>. The agglomeration of  $\text{Co}_3\text{O}_4$  particles and relatively large volume change could lead to the pulverization of the active particles and the loss of particle-particle electrical contact during repeated lithiation and delithiation processes, and thus cause serious detriment of the cycling stability<sup>229, 231</sup>.

One possible strategy to alleviate these problems is to prepare nanometer-sized composite material with carbon nanofiber matrix, which has been proved to be an effective solution to enhance the cycling performance of  $\text{Co}_3\text{O}_4$  anode materials<sup>230, 232, 233</sup>. Carbon nanofibers

demonstrate good capability of buffering the volume change in the electrode structure, short lithium-ion diffusion pathway, and relatively high conductivity. The carbon matrix can accommodate the internal mechanical stress induced by the volume change of  $\text{Co}_3\text{O}_4$  nanoparticles and preserve the integrity of the anode. In addition, the matrix is electronically conductive and helps electron transport during lithium insertion and extraction processes<sup>72</sup>. In this chapter, the size effect of the  $\text{Co}_3\text{O}_4$  nanoparticles are investigated with 10 - 30 nm and 30 - 50 nm  $\text{Co}_3\text{O}_4$  nanoparticles imbedded in carbon nanofibers produced by electrospinning technology.

## 2. Experimental

PAN (Mw = 150,000) and solvent N, N-dimethylformamide (DMF) were purchased from Sigma Aldrich.  $\text{Co}_3\text{O}_4$  nanoparticles were obtained from US Research Nanomaterials, Inc., and their particle sizes were 10 - 30 nm and 30 - 50 nm, respectively.  $\text{Co}_3\text{O}_4$  nanoparticles were added in DMF solution of 8 wt% PAN to prepare spinning solutions at 60 °C.  $\text{Co}_3\text{O}_4$  concentration used was 20 wt% (compared to PAN). Mechanical stirring was applied for at least 48 h in order to obtain homogeneous dispersion of the nanoparticles.

Electrospinning process was carried out with a flow rate of 0.1 ml h<sup>-1</sup>, needle-to-collector distance of 15.5 cm, and voltage of 15 kV supplied by Gamma ES40P-20W/DAM. Dry fibers were accumulated on the grounded collector and formed free-standing fibrous mats. The electrospun  $\text{Co}_3\text{O}_4$ /PAN nanofibers were firstly stabilized in air environment at 280 °C for 5.3 h (heating rate: 5 °C min<sup>-1</sup>), and then carbonized at 700 °C for 1 h in an argon atmosphere (heating rate: 2 °C min<sup>-1</sup>).

The morphology of the resultant  $\text{Co}_3\text{O}_4/\text{C}$  nanofibers were evaluated with scanning electron microscope (SEM, JEOL 6400F Field Emission SEM at 5 kV). The average fiber diameters of 50 fibers per sample, without bead defects, were measured using Resolution. Fibers were also analyzed with a transmission electron microscope (TEM, Hitachi HF-2000 TEM at 200 kV). Analysis of the composition and crystal structure of  $\text{Co}_3\text{O}_4/\text{C}$  nanofibers was conducted using a Rigaku SmartLab X-ray diffractometer at a scan rate of  $5^\circ \text{ min}^{-1}$ .

Electrochemical experiments were performed using coin-type half cells containing carbonized  $\text{Co}_3\text{O}_4/\text{C}$  composite nanofibers as the working electrode and Li foil as the counter electrode.  $\text{Co}_3\text{O}_4/\text{C}$  composite nanofibers formed freestanding, conductive nonwoven mats, and they were directly used as the working electrodes without using any polymer binder or conductive filler. The electrolyte used was a 1 M  $\text{LiPF}_6$  solution in ethylene carbonate (EC)/dimethyl carbonate (DMC) (1:1 v/v). Galvanostatic charge and discharge experiments were conducted using a battery test instrument (LAND CT2001A) at a current density of  $50 \text{ mA g}^{-1}$  over the potential range from 0.01 to 2.50 V.

### 3. Results and discussion

#### 3.1 Morphology

Figure 6.1 exhibits SEM images of  $\text{Co}_3\text{O}_4/\text{C}$  nanofibers with different  $\text{Co}_3\text{O}_4$  particle sizes of 10 - 30 nm and 30 - 50 nm, respectively. The  $\text{Co}_3\text{O}_4/\text{C}$  nanofibers are relatively straight and exhibit uniformly-distributed diameters. Bead-like structures can be seen from both  $\text{Co}_3\text{O}_4/\text{C}$  nanofibers containing 10 - 30 nm and 30 - 50 nm  $\text{Co}_3\text{O}_4$  nanoparticles. Compared with

$\text{Co}_3\text{O}_4/\text{C}$  nanofibers containing 30 - 50 nm  $\text{Co}_3\text{O}_4$  nanoparticles in Figure 6.1C,  $\text{Co}_3\text{O}_4/\text{C}$  nanofibers containing 10 - 30 nm  $\text{Co}_3\text{O}_4$  nanoparticles in Figure 6.1A exhibit more irregular spherical beads with diameters around 500 nm. Under a higher magnification (Figures 6.1B and D), it is seen that the bead-like structures basically contain aggregations of  $\text{Co}_3\text{O}_4$  nanoparticles on the fiber surface.

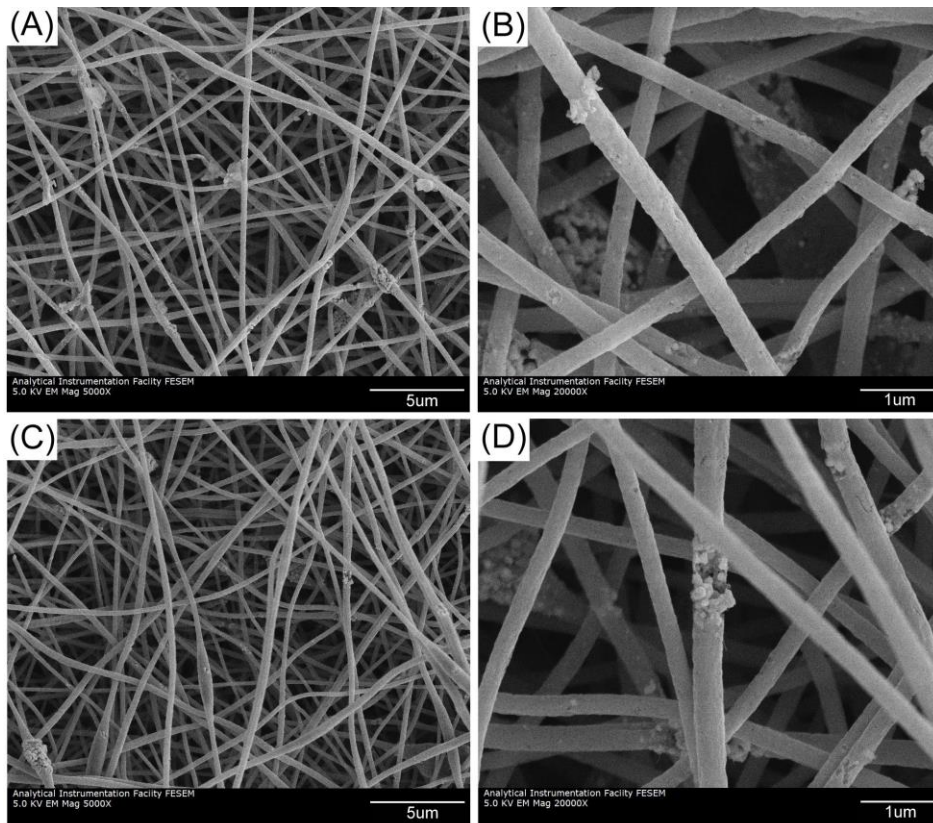


**Figure 6.1. SEM images of  $\text{Co}_3\text{O}_4/\text{C}$  composite nanofibers.  $\text{Co}_3\text{O}_4$  particle size: (A,B) 10 - 30 nm, and (C,D) 30 - 50 nm.**

Figure 6.2 shows TEM images of  $\text{Co}_3\text{O}_4/\text{C}$  nanofibers containing 10 - 30 nm and 30 - 50 nm  $\text{Co}_3\text{O}_4$  nanoparticles. It is seen that the majority of the nanoparticles are dispersed inside the carbon nanofiber matrix. A small portion of nanoparticles are not encapsulated inside in the nanofibers, but they appear to be attached to the fiber surface tightly. Most  $\text{Co}_3\text{O}_4$  nanoparticles are separated from each other; however, some nanoparticles form aggregates of 100 nm or greater. Comparing Figures 6.2A and B, it is seen that more individual  $\text{Co}_3\text{O}_4$  nanoparticles can be found in  $\text{Co}_3\text{O}_4/\text{C}$  nanofibers containing 30 - 50 nm  $\text{Co}_3\text{O}_4$  nanoparticles; on the other hand,  $\text{Co}_3\text{O}_4/\text{C}$  nanofibers containing 10 - 30 nm  $\text{Co}_3\text{O}_4$  nanoparticles have more  $\text{Co}_3\text{O}_4$  nanoparticle clusters, which are larger than 100 nm. In other words, 10 - 30 nm  $\text{Co}_3\text{O}_4$  nanoparticles have poorer dispersion than 30 - 50 nm  $\text{Co}_3\text{O}_4$  nanoparticles. This phenomenon can be explained that smaller particles have higher surface energy and tend to agglomerate into irregular and large secondary particles or clusters<sup>234-236</sup>.

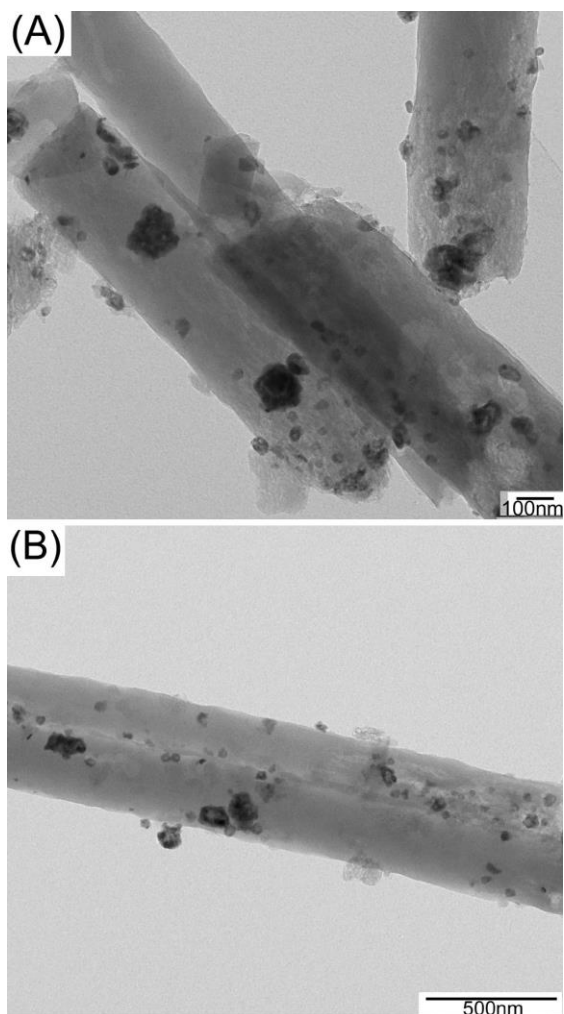


**Figure 6.2. TEM images of  $\text{Co}_3\text{O}_4/\text{C}$  composite nanofibers.  $\text{Co}_3\text{O}_4$  particle size: (A) 10 - 30 nm, and (B) 30 - 50 nm.**

To further investigate the effect of particle size on the morphology of  $\text{Co}_3\text{O}_4/\text{C}$  composite nanofibers, the fiber diameters are measured and their distributions are shown in Figure 6.3. The average fiber diameters of  $\text{Co}_3\text{O}_4/\text{C}$  composite nanofibers with 10 - 30 nm and 30 - 50 nm  $\text{Co}_3\text{O}_4$  nanoparticles are 294 and 269 nm, respectively. When the particle size is smaller,

the particles tend to form more agglomerates in the electrospinning solutions and result in higher solution viscosity. Nanofibers produced from high-viscosity solution typically have larger fiber diameters<sup>218</sup>. This result confirms the SEM and TEM observation (Figures 6.1 and 6.2) that the agglomerations of 10 - 30 nm  $\text{Co}_3\text{O}_4$  nanoparticles are severer than the 30 - 50 nm ones with same concentration of  $\text{Co}_3\text{O}_4$  in the composite nanofibers.

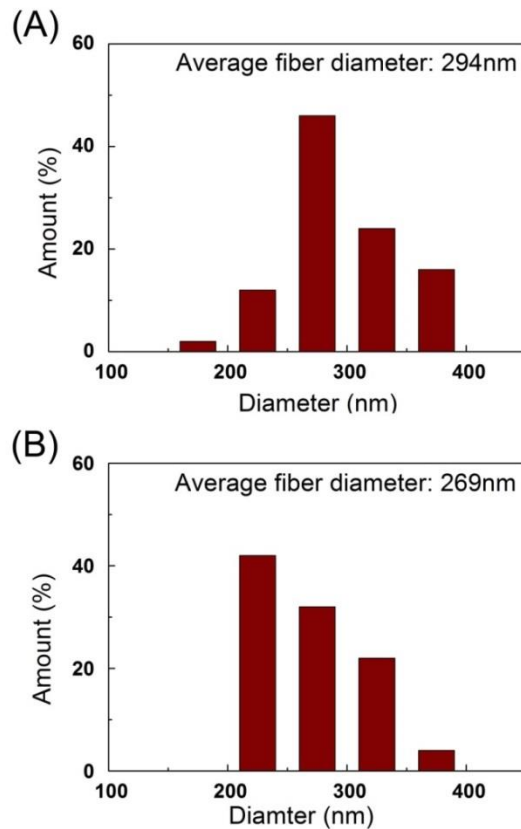


**Figure 6.3. Fiber diameter distributions of  $\text{Co}_3\text{O}_4/\text{C}$  composite nanofibers.  $\text{Co}_3\text{O}_4$  particle size: (A) 10 - 30 nm, and (B) 30 - 50 nm.**

Figure 6.4 illustrates the XRD pattern of  $\text{Co}_3\text{O}_4/\text{C}$  composite nanofibers with 30 - 50 nm  $\text{Co}_3\text{O}_4$  nanoparticles. Peaks at  $2\theta = 19.00, 31.28, 36.86,$  and  $65.25^\circ$  can be indexed to the pure cubic phase of  $\text{Co}_3\text{O}_4$  (JCPDS File No. 43-1003)<sup>237</sup>.  $\text{Co}_3\text{O}_4$  peaks are small because of the very fine grain size of  $\text{Co}_3\text{O}_4$  particles. From Figure 6.4, a broad carbon peak is also found at near  $2\theta = 25^\circ$ , corresponding to the (002) graphite layers; however, this peak is also weak, indicating low crystallinity of the carbon matrix<sup>72</sup>.

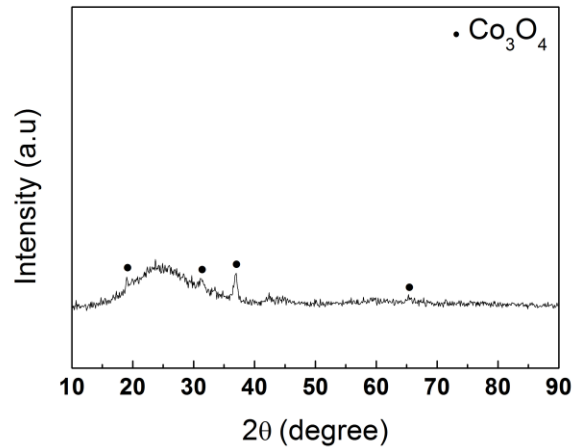


**Figure 6.4. XRD pattern of  $\text{Co}_3\text{O}_4/\text{C}$  composite nanofibers.  $\text{Co}_3\text{O}_4$  particle size: 30 - 50 nm.**

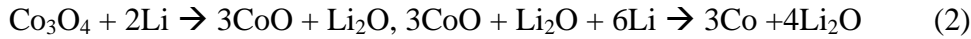
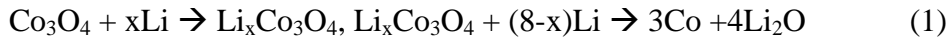
### 3.2 Electrochemical performance

Galvanostatic charge-discharge experiments were carried out at a current density of  $50 \text{ mA g}^{-1}$  within a voltage window of 0.01 - 2.50 V to evaluate the electrochemical performance of  $\text{Co}_3\text{O}_4/\text{C}$  composite nanofibers without using any binder or conductive additive.

Figure 6.5 exhibits the Galvanostatic charge-discharge profiles of  $\text{Co}_3\text{O}_4/\text{C}$  composite nanofibers at the first, second and twentieth cycles. It is seen in Figure 6.5A that, during the first discharge process,  $\text{Co}_3\text{O}_4/\text{C}$  composite nanofibers containing 10 - 30 nm  $\text{Co}_3\text{O}_4$  particles present a small voltage plateau at 0.90 V and then a sloping voltage profile from 0.90 V to the cut-off voltage of 0.01 V. For  $\text{Co}_3\text{O}_4/\text{C}$  composite nanofibers containing 30 - 50 nm  $\text{Co}_3\text{O}_4$  particles, the voltage plateau slightly increases to around 1.00 V. The voltage plateau can be attributed to the decomposition of the electrolyte and the formation of solid electrolyte interface (SEI)<sup>238</sup>.  $\text{Co}_3\text{O}_4/\text{C}$  composite nanofibers containing 10 - 30 nm  $\text{Co}_3\text{O}_4$  particles show an initial discharge capacity of  $1030 \text{ mAh g}^{-1}$  and charge capacity of  $450 \text{ mAh g}^{-1}$ , respectively.  $\text{Co}_3\text{O}_4/\text{C}$  composite nanofibers containing 30 - 50 nm  $\text{Co}_3\text{O}_4$  particles have an initial discharge capacity of  $1020 \text{ mAh g}^{-1}$  and charge capacity of  $480 \text{ mAh g}^{-1}$ , respectively. The first-cycle discharge capacities are greater than the theoretical capacity of pure  $\text{Co}_3\text{O}_4$  ( $890 \text{ mAh g}^{-1}$ ), which further confirms the formation of SEI film<sup>231</sup>. However, the first-cycle reversible capacities of  $\text{Co}_3\text{O}_4/\text{C}$  composite nanofibers are low due to a phase transition during the initial lithiation process, which have been examined by Larcher and others<sup>147, 153, 229-231, 237, 239</sup>. It has been reported that the large initial irreversible capacity is caused by the phase transition of  $\text{Li}_{1.47}\text{Co}_3\text{O}_4$  from an intermediate lithiated phase to an amorphous

phase<sup>147</sup>.  $\text{Li}_{1.47}\text{Co}_3\text{O}_4$  is produced by one of the two competing mechanisms to reach the full decomposition of the  $\text{Co}_3\text{O}_4$  electrode into Co nanograins during lithium insertion process.

The two competing mechanisms are<sup>147</sup>:



In their research, Larcher and coworkers have exemplified the  $\text{Co}_3\text{O}_4$  obtained at 500°C or higher would mainly go through the first mechanism during lithiation process, which has caused the consequences of the phase transition and reduced the initial reversible capacity<sup>147, 232</sup>. However, other researchers have argued that the low initial reversible capacity is related to the formation/decomposition of  $\text{Li}_2\text{O}$  produced by the second mechanism as well as SEI film formation<sup>240, 241</sup>. They have concluded that  $\text{Li}_2\text{O}$  is known to be electrochemically inactive and the incomplete decomposition of  $\text{Li}_2\text{O}$  is responsible for the large irreversible capacity loss of  $\text{Co}_3\text{O}_4$  anode during cycling<sup>153, 232, 237, 239</sup>.

From Figures 6.5B and C, which exhibit the Galvanostatic charge-discharge curves of the second and twentieth cycles of  $\text{Co}_3\text{O}_4/\text{C}$  composite nanofibers, it is seen that the reversible capacities of nanofibers containing 30 - 50 nm  $\text{Co}_3\text{O}_4$  nanoparticles increase while those containing 10 - 30 nm  $\text{Co}_3\text{O}_4$  nanoparticles decrease. The reversible capacities of  $\text{Co}_3\text{O}_4/\text{C}$  composite nanofibers containing 10 - 30 nm  $\text{Co}_3\text{O}_4$  particles are 378 and 337 mAh g<sup>-1</sup>, respectively, at the second and twentieth cycles, while the reversible capacities of  $\text{Co}_3\text{O}_4/\text{C}$

composite nanofibers containing 30 - 50 nm  $\text{Co}_3\text{O}_4$  particles are much larger: 677 and 545  $\text{mAh g}^{-1}$ , respectively.

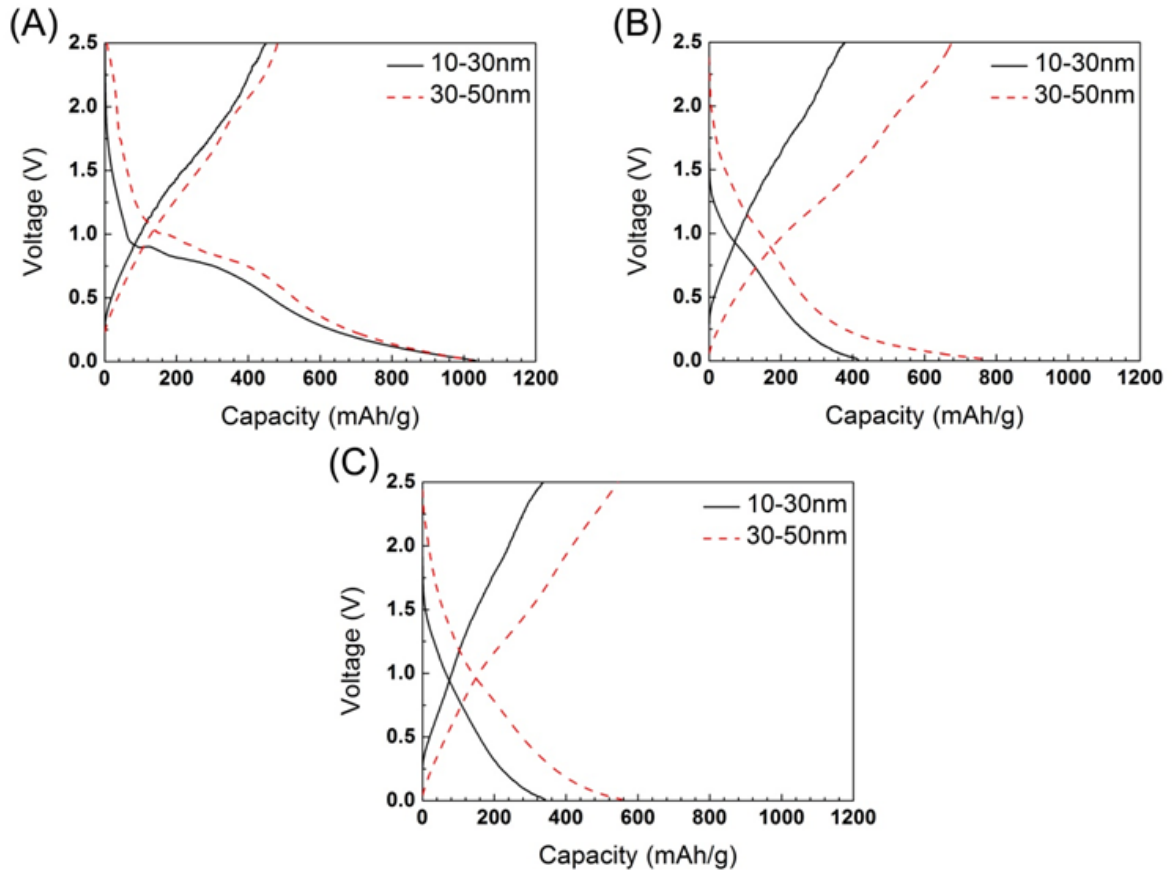


**Figure 6.5.** Galvanostatic charge-discharge curves of  $\text{Co}_3\text{O}_4/\text{C}$  composite nanofibers with different  $\text{Co}_3\text{O}_4$  particle sizes. (A) The first cycle, (B) the second cycle, and (C) the twentieth cycle.

Figure 6.6 shows the cycling performance of  $\text{Co}_3\text{O}_4/\text{C}$  composite anodes with 10 - 30 nm and 30 - 50 nm  $\text{Co}_3\text{O}_4$  nanoparticles, respectively. The reversible capacities of the  $\text{Co}_3\text{O}_4/\text{C}$  anode with 10 - 30 nm  $\text{Co}_3\text{O}_4$  nanoparticles decline drastically with increase in cycle number. While the  $\text{Co}_3\text{O}_4/\text{C}$  anode with 30 - 50 nm  $\text{Co}_3\text{O}_4$  nanoparticles shows relatively good cycling stability with a high reversible capacity of  $545 \text{ mAh g}^{-1}$  at twentieth cycle, compared to commercial  $\text{Co}_3\text{O}_4$  anodes (less than  $200 \text{ mAh g}^{-1}$ ) performed by others<sup>230</sup>. This result indicates that the carbon nanofiber matrix, which buffers the volume change of  $\text{Co}_3\text{O}_4$  nanoparticles in the composite, plays an important role in the improvement of the cycling performance of  $\text{Co}_3\text{O}_4/\text{C}$  anode.

For the  $\text{Co}_3\text{O}_4/\text{C}$  composite anodes with 10 - 30 nm  $\text{Co}_3\text{O}_4$  nanoparticles, the fast fading of charge-discharge capacities may be caused by two reasons. One reason is that 10 - 30 nm  $\text{Co}_3\text{O}_4$  nanoparticles possess large surface area and the surface layer participates in the progressive cycling and loses the electrochemical reactivity gradually during cycling<sup>232</sup>. Another reason is that too much agglomeration of the  $\text{Co}_3\text{O}_4$  nanoparticles results in pulverization, loss of active material, and electrical isolation during the charge and discharge processes. Similar results are shown in other work<sup>238</sup>.

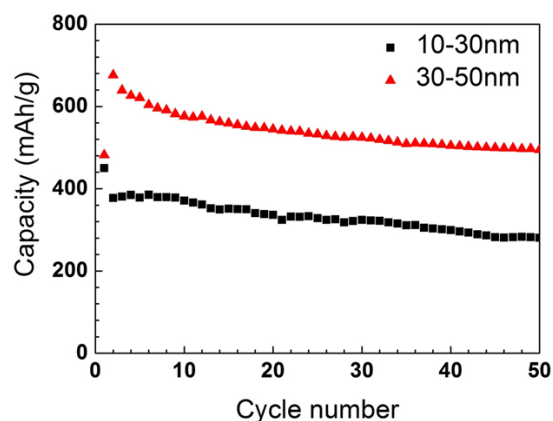


**Figure 6.6. Cycling performance of  $\text{Co}_3\text{O}_4/\text{C}$  composite nanofibers with different  $\text{Co}_3\text{O}_4$  particle sizes.**

The comparison of the Coulombic efficiencies of  $\text{Co}_3\text{O}_4/\text{C}$  composite nanofiber anodes containing 10 - 30 nm and 30 - 50 nm  $\text{Co}_3\text{O}_4$  nanoparticles is shown in Figure 6.7. The Coulombic efficiencies of the first cycle of  $\text{Co}_3\text{O}_4/\text{C}$  composite nanofiber anodes with 10 - 30 nm and 30 - 50 nm  $\text{Co}_3\text{O}_4$  nanoparticles are 44% and 48%, respectively. The Coulombic efficiencies of the second cycle are 92% and 87%, as well as 99% and 99% for twentieth cycle. As discussed, the relatively low Coulombic efficiencies of the first cycle are mainly due to: i) the decomposition of the electrolyte and formation of the SEI film which hinders the ability of delithiation of the electrode, and ii) a phase transition during the reduction of  $\text{Co}_3\text{O}_4$  to nanograin Co, amorphous  $\text{Li}_{1.47}\text{Co}_3\text{O}_4$  and  $\text{Li}_2\text{O}$ . However, during the second discharge, the delithiation process releases Li ions and oxidizes nanograin Co to  $\text{Co}_3\text{O}_4$ , which increases the second reversible capacities and therefore, the Coulombic efficiencies. In

addition, it is possible that amorphous  $\text{Li}_{1.47}\text{Co}_3\text{O}_4$  confines the volume change of  $\text{Co}_3\text{O}_4$  nanoparticles and raises the conductivity of the composite nanofibers by connecting the active materials. After five cycles, the Coulombic efficiencies reach almost 100% for both  $\text{Co}_3\text{O}_4/\text{C}$  composite nanofiber anodes containing 10 - 30 nm and 30 - 50 nm  $\text{Co}_3\text{O}_4$  nanoparticles.

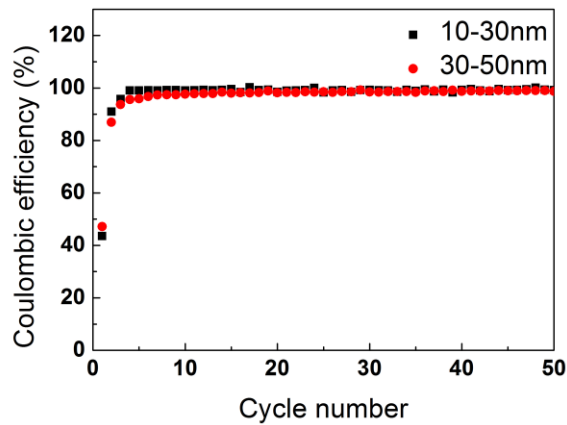


**Figure 6.7. Coulombic efficiencies of  $\text{Co}_3\text{O}_4/\text{C}$  composite nanofibers with different  $\text{Co}_3\text{O}_4$  particle sizes.**

#### 4. Conclusion

$\text{Co}_3\text{O}_4/\text{C}$  composite nanofibers containing 10 - 30 nm and 30 - 50 nm  $\text{Co}_3\text{O}_4$  nanoparticles were fabricated through electrospinning and thermal treatment processes. Compared with  $\text{Co}_3\text{O}_4/\text{C}$  nanofibers containing 10 - 30 nm  $\text{Co}_3\text{O}_4$  nanoparticles,  $\text{Co}_3\text{O}_4/\text{C}$  anodes with 30 -

50 nm  $\text{Co}_3\text{O}_4$  nanoparticles exhibited high reversible capacity, improved Coulombic efficiencies, and good cycling stability when used as binder-free anode material for lithium-ion batteries. In contrast, the  $\text{Co}_3\text{O}_4/\text{C}$  composite nanofibers with 10 - 30 nm  $\text{Co}_3\text{O}_4$  nanoparticles showed low charge-discharge capacities due to the pulverization of the electrode and the degradation of the electrochemical activity resulting from severe nanoparticle aggregation and large surface area. However, after the second cycle, both  $\text{Co}_3\text{O}_4/\text{C}$  nanofibers displayed Coulombic efficiencies of almost 100%. The relatively good cycling performance of  $\text{Co}_3\text{O}_4/\text{C}$  composite nanofibers derived from  $\text{Co}_3\text{O}_4/\text{PAN}$  nanofibers could be attributed to their unique composite structure with an improved dispersion of  $\text{Co}_3\text{O}_4$  nanoparticles, the unique one-dimensional fiber structure, and the shorter lithium ion diffusion distance in the nanofibers.

CHAPTER 7 NANOSIZED Ge@CNF, Ge@C@CNF AND Ge@CNF@C COMPOSITES  
VIA CVD METHOD FOR USE IN ADVANCED LITHIUM-ION BATTERIES

Abstract: Three distinct Ge nanoparticle-filled carbon nanofiber (CNF) composites, Ge@CNF, Ge@C@CNF and Ge@CNF@C, were fabricated by using chemical vapor deposition (CVD) and electrospinning techniques for use as binder-free electrodes were synthesized and studied for rechargeable lithium-ion batteries. These new Ge@CNF, Ge@C@CNF and Ge@CNF@C structures were prepared by: 1) dispersing Ge nanoparticles into carbon nanofibers (CNF), 2) dispersing carbon-coated Ge nanoparticles (Ge@C) prepared by chemical vapor deposition (CVD) into CNF, and 3) depositing CVD carbon onto Ge@CNF, respectively. In Ge@C@CNF and Ge@CNF@C, the Ge nanoparticles and CNFs were coated by CVD carbon coating, respectively. In general, Ge anode materials suffered from serious volume changes and nanoparticle aggregations during lithium insertion and extraction, resulting in pulverization and capacity loss. Carbon nanofiber and the additional CVD carbon layer could help to preserve the alloy anode materials during repeated cycling, and consequently maintained the cycling stability. In this work, it was found that among the three composites, Ge@CNF@C exhibited the highest capacity retention (~89%) at 50<sup>th</sup> cycle and a continuously increasing tendency of reversible capacities from 544 to 553 mAh g<sup>-1</sup> between 25<sup>th</sup> and 50<sup>th</sup> cycles, due to structurally durable thorn-like Ge structure and the additional carbon confinement fabricated by the CVD method. However, Ge@C@CNF encountered rapid capacity loss because large Ge clusters were formed in the carbon matrix.

Results demonstrated that Ge@CNF@C is the most promising anode candidate among the three composites.

Keywords: Germanium, chemical vapor deposition, electrospinning, lithium-ion battery.

## 1. Introduction

Rechargeable lithium-ion batteries have long been considered as an attractive power source for portable electronics, electric vehicles, and emerging smart grids<sup>146</sup>. One of the main challenges in the design of high-performance lithium-ion batteries is to maintain the structural stability of the electrodes during repeated lithium insertion and extraction<sup>73, 74, 99</sup>. For example, alloying anodes, such as Si, Ge, Sn, Pb, Al, Au and Mg, possess high lithium storage ability but suffer from large volume change during cycling. To address this issue, alloying anodes have been modified by downsizing the bulk materials to the nanoscale, dispersing the elements into carbon matrices, or preparing intermetallic alloying materials<sup>69, 70, 242</sup>. Recently, Li *et al.* fabricated a nano-Si anode material by laser-induced silane gas reaction and obtained a high reversible capacity of 1700 mAh g<sup>-1</sup> even after the tenth cycle<sup>243</sup>. Ji *et al.* also reported the preparation and cyclic profiles of Si/C composite nanofibers by embedding Si nanoparticles in electrospun carbon nanofibers. The Si/C composite anode exhibited a reversible capacity of around 800 mAh g<sup>-1</sup> and a capacity retention of 85% after 20 cycles<sup>1, 72-74</sup>. Moreover, Li *et al.* prepared FeSi<sub>6</sub>/graphite composite by mechanical ball milling method. The composite anode offered a large reversible capacity (800 mAh g<sup>-1</sup>) and good cycleability, due to the buffering effect of the inactive FeSi<sub>2</sub> phase and graphite layers on the volumetric changes of Si phase during alloying reaction<sup>93</sup>.

Among the various alloying anodes, Si has been the focus of recent research, while Ge, another high-capacity material, has received less attention. Compared to Si, Ge has smaller volume change and higher lithium diffusion coefficient, and is also a promising anode

material candidate<sup>96</sup>. Cui *et al.* prepared Ge/carbon composite nanospheres and Ge/carbon nanotubes through a pyrolysis technique and obtained good structural morphology and electrochemical performance<sup>100, 244</sup>. Recently, Woo *et al.* fabricated Ge nanowire/graphite nanofiber composites prepared by chemical vapor deposition (CVD). The composite anodes showed high rate capability due to the entangled structure and the resultant high contact area between the Ge nanowires and graphite nanofibers<sup>245</sup>. Although promising electrode systems have recently been proposed, the cycling performance of most Ge-based anodes is still limited by the relatively large volume change, which cannot be prevented by only one carbon layer confinement on Ge nanoparticles.

In this work, we prepared new Ge@CNF, Ge@C@CNF and Ge@CNF@C structures by: 1) dispersing Ge nanoparticles into carbon nanofibers (CNF), 2) dispersing carbon-coated Ge nanoparticles (Ge@C) prepared by chemical vapor deposition (CVD) into CNF, and 3) depositing CVD carbon onto Ge@CNF, respectively. The schematic of the three structures and their fabrication processes are illustrated in Figure 7.1. In Ge@C@CNF and Ge@CNF@C structures, two carbon confinement structures were formed on the Ge active material, including the amorphous carbon coating fabricated by the CVD method and carbon nanofiber matrix by electrospinning. The amorphous carbon coating deposited by CVD can prevent the cracking of the Ge nanoparticles in the Ge@C@CNF and the pulverization of the integral Ge@CNF structure in the Ge@CNF@C.

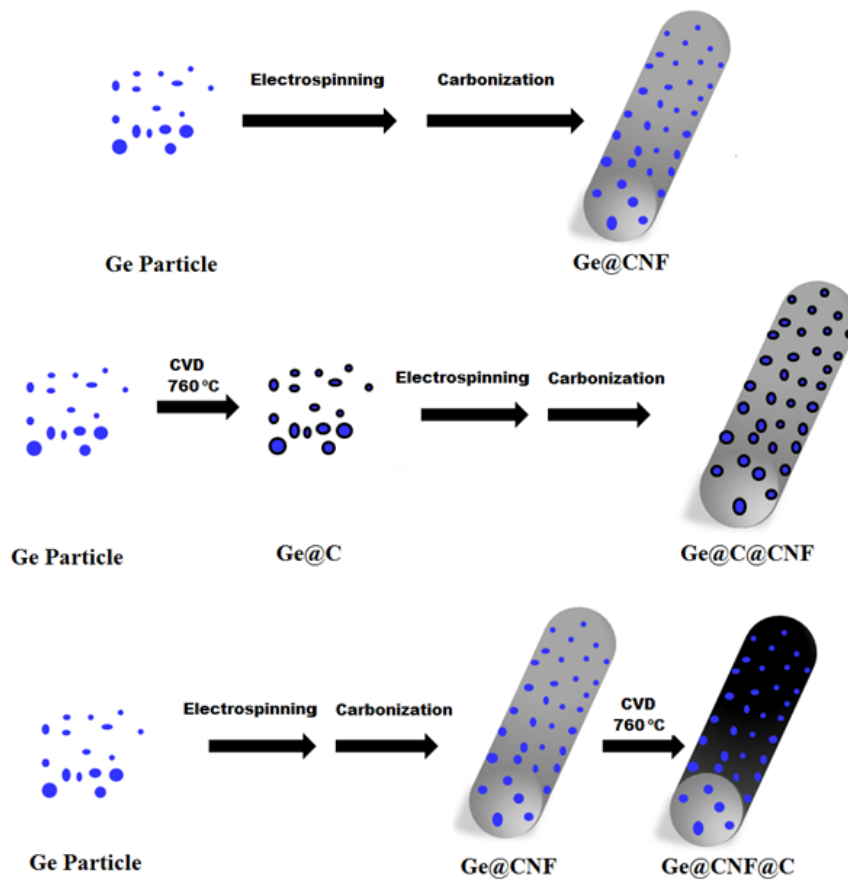


**Figure 7.1. Schematics illustrating the fabrication processes of (A) Ge@CNF, (B) Ge@C@CNF, and (C) Ge@CNF@C.**

## 2. Experimental

Ge nanoparticles were purchased from SkySpring Nanomaterials, and the particle size was 70 - 120 nm. Polyacrylonitrile (PAN, Mw = 150,000) and solvent *N,N*-Dimethylformamide (DMF) were purchased from Sigma Aldrich.

For Ge@CNF (Figure 7.1A), Ge nanoparticles were added into an 8% PAN solution in DMF. Dispersions of 30 wt% Ge particles (compared to PAN) in PAN solutions were prepared at 60 °C. Mechanical stirring was applied for at least 24 h in order to ensure that the dispersions were homogeneous. To obtain composite nanofibers, a high-voltage power supply (Gamma ES40P-20W/DAM) was used to provide a voltage at around 15 kV during the electrospinning. Dry fibers were accumulated on the collector and formed fibrous mats. The electrospun Ge@PAN nanofibers were firstly stabilized in air environment at 280 °C for 5.3 h (heating rate: 5 °C min<sup>-1</sup>), and then carbonized at 700 °C for 1 h in an argon atmosphere (heating rate: 2 °C min<sup>-1</sup>) to form Ge@CNF.

For Ge@C@CNF (Figure 7.1B), Ge particles were first coated by CVD amorphous carbon using an ASM 6" LPCVD with an operating temperature of 760 °C and an operating pressure of 10 Torr. Pure CH<sub>4</sub> gas was used as the carbon precursor with a flow rate of 200 sccm. The deposition time used was 60 min. The resultant Ge@C nanoparticles (30 wt%) were added into an 8% PAN solution in DMF to obtain Ge@C@PAN electrospun nanofibers. The final product Ge@C@CNF was obtained by stabilizing and carbonizing Ge@C@PAN under the same conditions as used for Ge@CNF.

For Ge@CNF@C (Figure 7.1C), 30 wt% Ge nanoparticles (compared to PAN) were added into an 8% PAN solution in DMF, which was then electrospun into Ge@PAN nanofibers. The electrospun Ge@PAN nanofibers were carbonized to form Ge@CNF. The final product Ge@CNF@C was obtained by depositing CVD carbon on Ge@CNF. The electrospinning,

carbonization and CVD processing conditions of Ge@CNF@C used were the same as those used for Ge@C@CNF.

The morphology of the resultant Ge@CNF, Ge@C@CNF, and Ge@CNF@C was observed with scanning electron microscope (SEM) (JEOL 6400F Field Emission SEM at 5 kV) and transmission electron microscopy (Hitachi HF-2000 TEM at 200 kV). In order to investigate the composition of the resultant Ge@CNF@C material, atomic resolution elemental mapping in FEI Titan STEM was used.

Electrochemical experiments were performed using coin-type half cells containing Ge@CNF, Ge@C@CNF, and Ge@CNF@C as the working electrodes and Li foil as the counter electrode. The as-prepared Ge@CNF, Ge@C@CNF, and Ge@CNF@C fiber mats were attached onto copper foil (Aldrich, 0.025 mm thick) to form the working electrodes. The separator used was Separator 2400 (Celgard). The electrolyte used was a 1 M LiPF<sub>6</sub> solution in ethylene carbonate (EC)/dimethyl carbonate (DMC) (1:1 v/v). The electrochemical performance was evaluated by carrying out galvanostatic charge-discharge experiments at 50 mA g<sup>-1</sup> between 0.01 and 2.00 V.

### 3. Results and discussion

#### 3.1 Morphology

The SEM images of Ge@CNF, Ge@C@CNF, and Ge@CNF@C are represented in Figure 7.2. Large particle clusters can be observed in Ge@CNF and Ge@C@CNF, indicating non-

uniform dispersion of Ge and Ge@C nanoparticles in the CNF matrix. However, no obvious Ge clusters are shown in Ge@CNF@C, suggesting a homogenous dispersion of Ge particles. From Figure 7.2, it is also seen that Ge@C@CNF and Ge@CNF@C have smaller fiber diameters than Ge@CNF. The smaller diameter of Ge@C@CNF is probably related to the altered particle-fiber interaction caused by the CVD carbon coating on the Ge particle surface. The smaller diameter of Ge@CNF@C is caused by high-temperature CVD treatment applied to the fibers. For Ge@CNF@C, the Ge particles were first dispersed in the CNF matrix and the subsequent CVD coating process at 760 °C reduced the fiber diameter by further thermal deformation and removal of residual non-carbon element from the fiber matrix. As shown in Figure 7.2C, this thermal deformation also leads to some irregular and bent fibers.

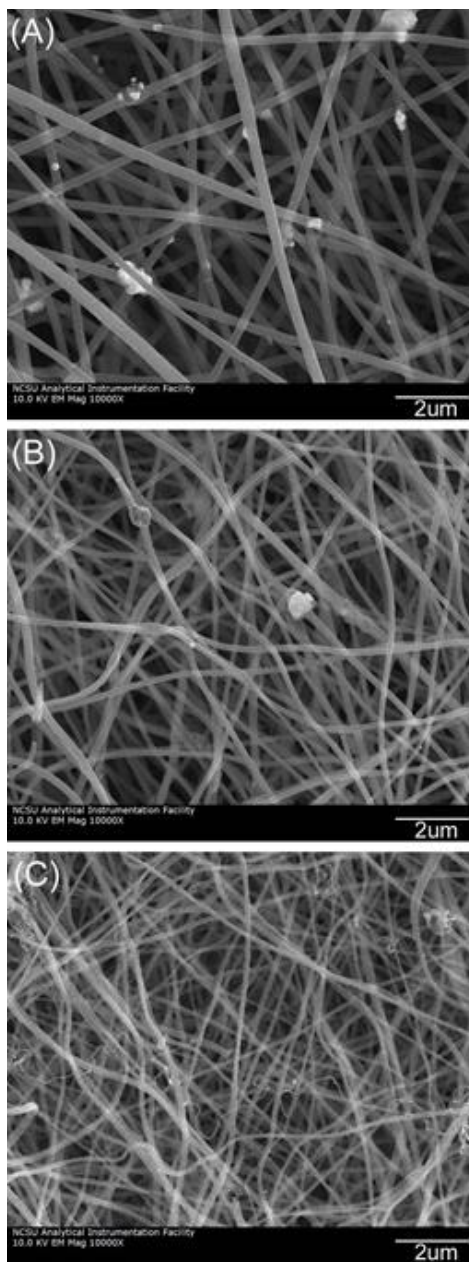


**Figure 7.2. SEM images of (A) Ge@CNF, (B) Ge@C@CNF, and (C) Ge@CNF@C.**

The TEM images of Ge@CNF, Ge@C@CNF and Ge@CNF@C are shown in Figure 7.3. These composite nanofibers were grounded and ultrasonically treated prior to TEM

observation. As shown in Figure 7.3A, large Ge nanoparticle clusters (around 250 - 300 nm) are formed and dispersed in the carbon matrix. Compared to Ge@CNF, the Ge clusters in Ge@C@CNF are smaller (Figure 7.3B). However, a void around 700 nm × 200 nm was formed after ultrasonic treatment. Figure 7.3B is a representative image of Ge@C@CNF, and such defects (*i.e.*, voids) can be commonly seen in Ge@CNF@C samples. This indicates serious aggregation of Ge@C nanoparticles in the fiber matrix, which may exacerbate the pulverization of the particles and result in rapid capacity loss during cycling if this material is used as a lithium-ion battery anode. However, from Figure 7.3C, it is seen that Ge@CNF@C shows homogeneously distributed Ge thorns of 50 - 100 nm embedded in or attached on the surface of the CNF matrix.

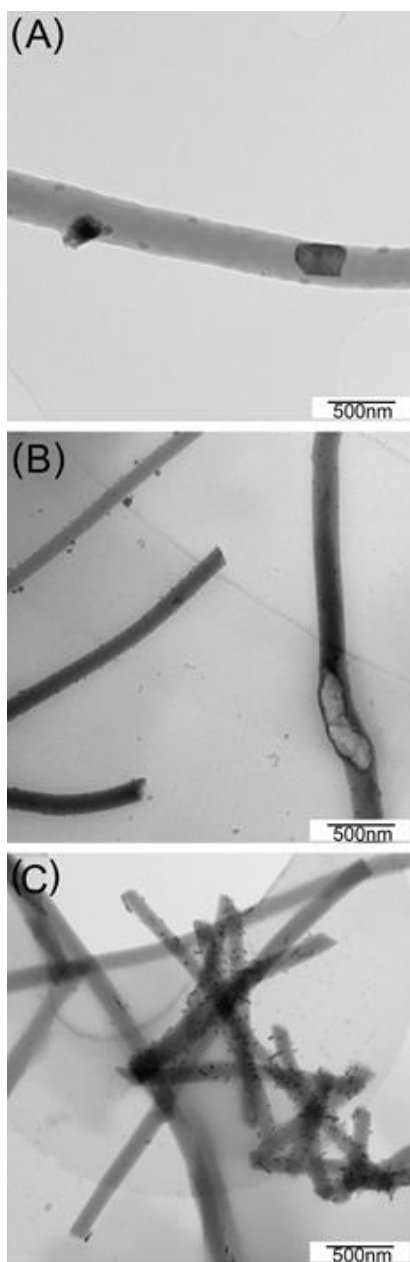


**Figure 7.3. TEM images of (A) Ge@CNF, (B) Ge@C@CNF, and (C) Ge@CNF@C.**

To further investigate the unique structure of Ge@CNF@C, high-resolution SEM image, atomic resolution elemental mapping and Energy-dispersive X-ray spectroscopy (EDX)

spectrum were obtained (Figure 7.4). Figure 7.4A shows a Ge@CNF@C nanofiber with thorn-like structures of around 10nm in width and 30 - 80 nm in length. The composition of the nanofiber and the thorn-like structure were investigated by elemental mapping technique. As indicated in Figure 7.4B, the nanofiber and the thorn-like structures are composed of carbon and Ge, which are colored in red and light green, respectively. The EDX spectrum presents two characteristic peaks at 1 and 10 keV, which are typical for Ge element, as well as a 0.5 keV peak for carbon (Figure 7.4C). Sn impurities are also detected in the spectrum. These results indicate that the thorn-structures are formed by Ge during the CVD treatment at 760 °C. It is likely that the formation Ge thorns is facilitated by the Sn impurities, which function as catalyst particles. There are literature reports on the formation of Ge thorns facilitated by metal catalysts, such as Sn, Au, Ni, Cu, Co. For example, Wu *et al.* obtained similar Ge thorns or nanorods by using Er-doped SnO<sub>2</sub> nanofibers with the CVD method<sup>246</sup>. Meng's group has substantially discussed on the yield and quality of Ge nanorods by using different catalytic metals (Au, Ni, Cu, Co) during the CVD process<sup>247</sup>. In our work, the Sn impurities might have served as the catalyst that facilitated the formation of Ge thorns during CVD treatment.

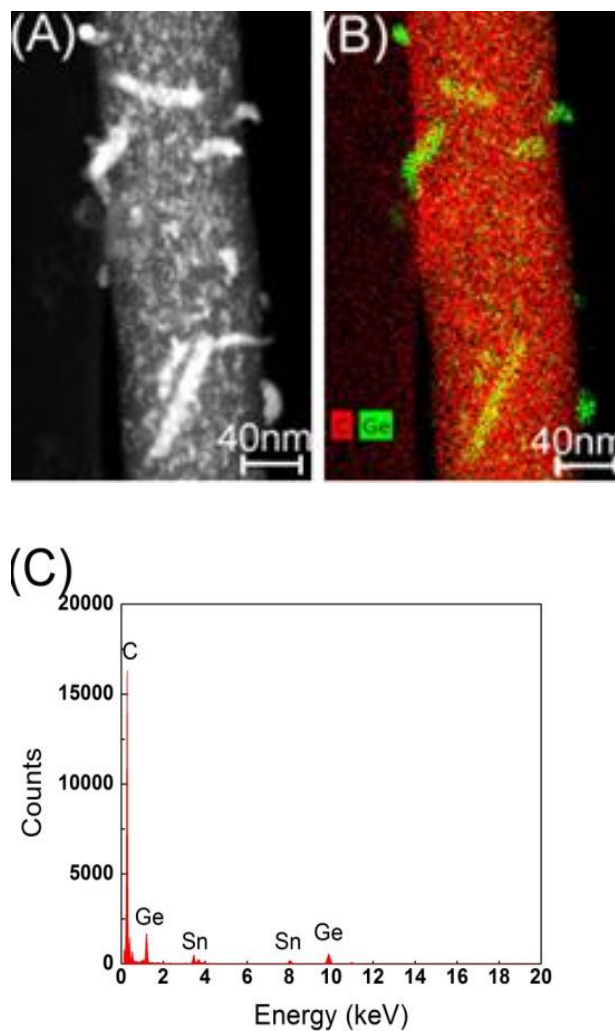


**Figure 7.4. (A) High-resolution STEM image, (B) atomic resolution elemental map and (C) EDX spectrum of Ge@CNF@C. In the atomic resolution elemental map, Ge and carbon elements are colored with light green and red, respectively.**

Figure 7.5 shows the Raman spectra of Ge@CNF, Ge@C@CNF, and Ge@CNF@C. For comparison, the Raman spectrum of Ge@C particles is also shown. For all four samples, a strong D-band at around  $1350\text{ cm}^{-1}$  and a relatively small G-band at  $1600\text{ cm}^{-1}$  are observed.

The D-band can be explained as structure defect- and disorder-induced features in the graphene layers of carbon materials, while the G-band is indicative of the high-frequency  $E_{2g}$  first-order graphitic crystallites of the carbon. The presence of the strong D band suggests that the carbon component has typical disordered graphitic structure with low crystallinity and graphitization<sup>228</sup>. The intensity ratio of D peak to G peak, denoted by  $R_I = I_D/I_G$ , is a good indication of the carbon structure, and a higher  $R_I$  value typically indicates a more disordered carbon structure. As shown in Figure 7.5, the  $R_I$  values of Ge@C, Ge@CNF, Ge@C@CNF, and Ge@CNF@C are 1.358, 1.074, 1.106 and 1.103 respectively. The higher  $R_I$  value of Ge@C than that of Ge@CNF suggests that the carbon coating created by CVD is more amorphous or disordered than the CNF matrix.

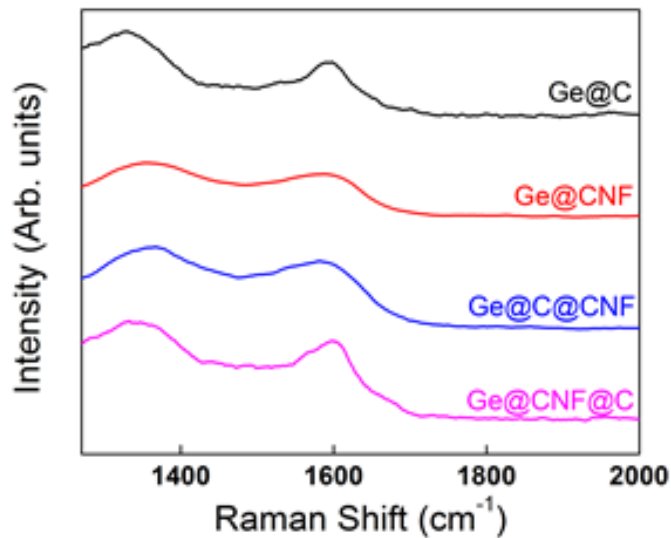


**Figure 7.5. Raman spectra of Ge@C, Ge@CNF, Ge@C@CNF, and Ge@CNF@C.**

### 3.2 Electrochemical performance

Galvanostatic charge-discharge experiments were carried out at a current density of  $50 \text{ mA g}^{-1}$  within a voltage window of 0.01 - 2.00 V to evaluate the electrochemical performance. Figure 7.6 shows galvanostatic charge-discharge curves of the first, second and twentieth cycles of Ge@CNF, Ge@C@CNF and Ge@CNF@C. In the first cycle, the voltage of all three electrodes drops rapidly during the discharge process from 2.00 V to about 0.7, 0.4 and 1.2 V, respectively, followed by a small plateau and a sloping line smoothly downshifting to 0.01 V. This small plateau is known as the result of the decomposition of electrolyte solution and the formation of the solid electrolyte interface (SEI), which covers the electrode surface and hinders the electrolyte from further decomposition<sup>72, 86</sup>. In the second cycle, the plateau disappears, indicating a stable SEI has formed. From Figure 7.6, it is also seen that Ge@CNF and Ge@CNF@C exhibit smaller initial capacity losses than Ge@C@CNF. For example, in the first cycle, Ge@CNF, Ge@C@CNF, and Ge@CNF@C show specific discharge capacities of 1385, 1070, and 1466  $\text{mAh g}^{-1}$ , and charge capacities of 808, 252, and 626  $\text{mAh g}^{-1}$ , respectively. The initial irreversible capacities of 577, 818, and 840  $\text{mAh g}^{-1}$  can be mainly ascribed to the formation of the SEI film during the first cycle. In the second cycle, the discharge capacities of Ge@CNF, Ge@C@CNF, and Ge@CNF@C are 781, 278, and 747  $\text{mAh g}^{-1}$ , and their charge capacities are 741, 229, and 639  $\text{mAh g}^{-1}$ , respectively. Ge@CNF and Ge@CNF@C exhibit higher Li storage abilities and capacity retentions than Ge@C@CNF. It is believed that the huge capacity loss of Ge@C@CNF is the consequence of the large volume expansion of aggregated Ge@C nanoparticles during the formation of  $\text{Li}_x\text{Ge}$  and subsequent detachment of the nanoparticles from the CNF matrix. This agrees

with the TEM result shown in Figure 7.3B. On the other hand, the homogenous dispersion of Ge nanoparticles and good confinement of carbon material in Ge@CNF@C (Figure 7.3C) result in a stable cycleability.

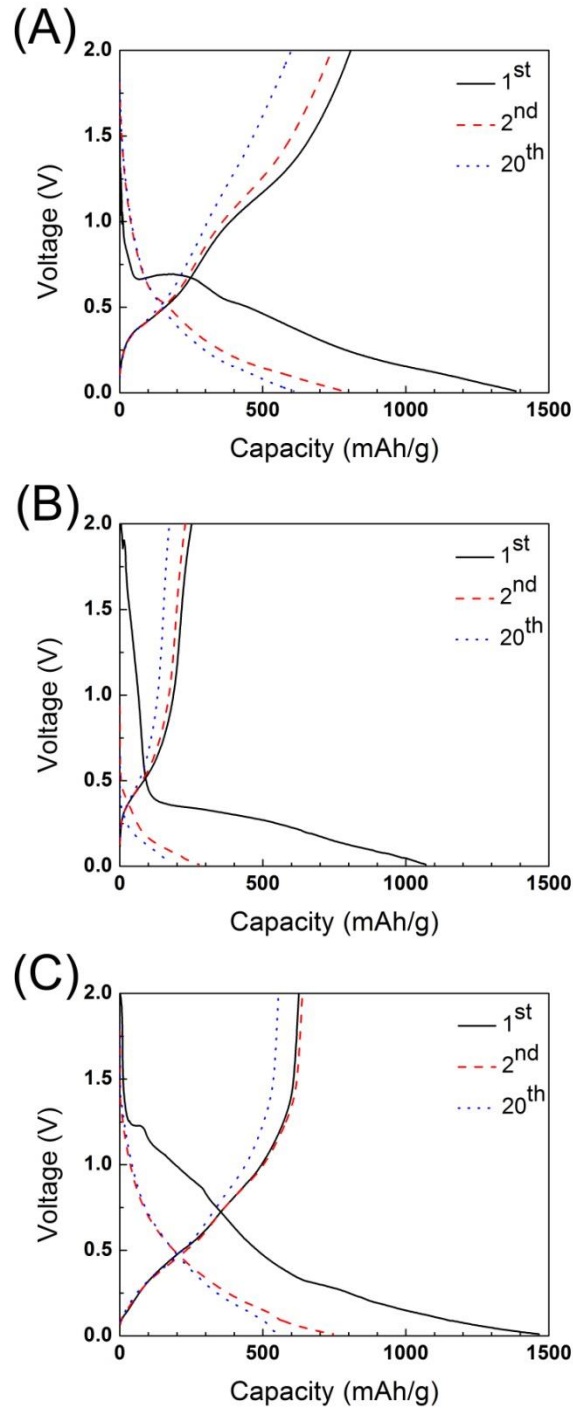


**Figure 7.6.** Galvanostatic charge-discharge curves of the first, second and twentieth cycles of (A) Ge@CNF, (B) Ge@C@CNF, and (C) Ge@CNF@C.

Differential capacity curves of the first and second cycles of Ge@CNF, Ge@C@CNF, and Ge@CNF@C are plotted in Figure 7.7. In the lithium alloying process, peaks indicate the lithium insertion into equipotential sites, and the presence of multiple sharp peaks at the first cycle suggests the formation of a number of different  $\text{Li}_x\text{Ge}_y$  phases during electrochemical lithiation<sup>98</sup>. In Figure 7.7, the voltage values (0.50 - 1.10, 0.30 - 0.50, 0.15 - 0.30, and 0 - 0.15 V) are consistent with those reported for  $\text{Li}_9\text{Ge}_4$ ,  $\text{Li}_7\text{Ge}_2$ ,  $\text{Li}_{15}\text{Ge}_4$ , and  $\text{Li}_{22}\text{Ge}_5$  during lithium insertion<sup>96, 98, 248, 249</sup>. However, peaks at 0.69 (Figure 7.7A), 0.35 (Figure 7.7B) and 1.26 V (Figure 7.7C) during lithium alloy process are mainly ascribed to the SEI formation, which confirms the results shown in Figure 7.6. At the second cycle, the broad peaks during lithium alloy process indicated that Ge has turned into amorphous. In the lithium dealloying process, the typical dealloying reactions of Ge with lithium are observed at around 0.4 and 1.0 V.

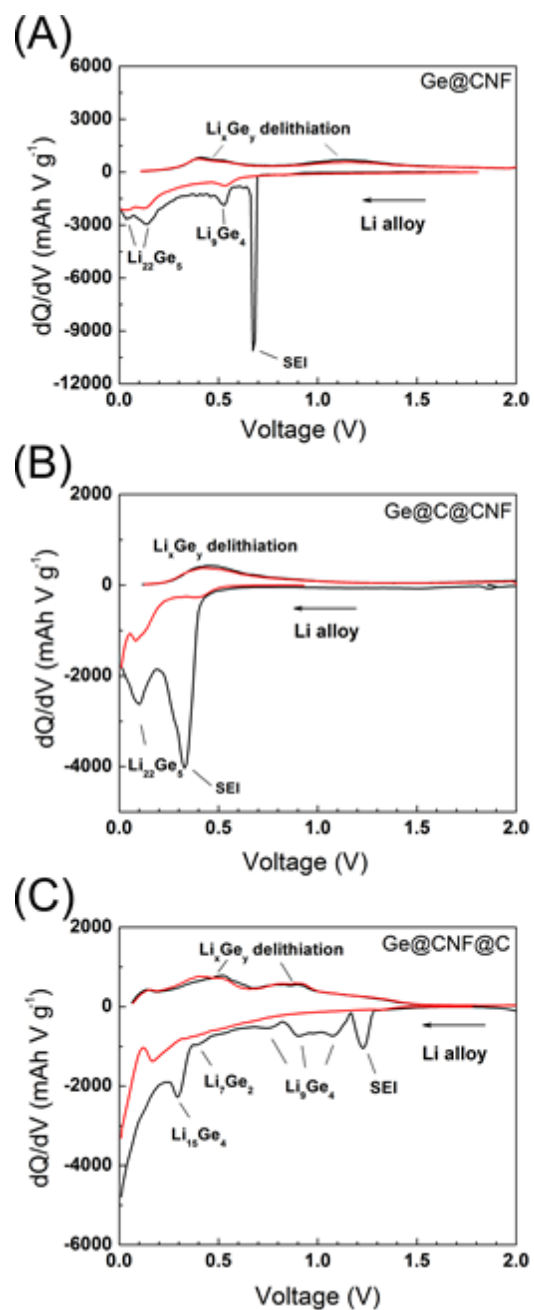


**Figure 7.7. Differential capacity plots of the first and second cycles of (A) Ge@CNF, (B) Ge@C@CNF, and (C) Ge@CNF@C.**

Figure 7.8 shows the cycling performance of Ge@CNF, Ge@C@CNF, and Ge@CNF@C. It is observed that during cycling, Ge@CNF@C exhibits more stable capacities than Ge@CNF and Ge@C@CNF. The significant capacity loss of Ge@C@CNF is mainly caused by the severe volume change of Ge clusters during lithium insertion and extraction. The enormous agglomeration and volume change of the Ge clusters lead to severe particle separation and pulverization of the anode structure. On the other hand, both Ge@CNF and Ge@CNF@C have more stable structures and can better tolerate the volume change upon repeating lithium insertion and extraction, and hence exhibit better cycling performance. Among three electrodes, Ge@CNF@C shows the highest capacity retention of 89% and a continuously increasing tendency of reversible capacities from 25<sup>th</sup> to 50<sup>th</sup> cycles. The reversible capacities increase from 544 to 553 mAh g<sup>-1</sup>. In Ge@CNF@C, the thorn-like structure of Ge possesses high aspect ratio, which is more structurally durable during the processes of Li insertion and extraction. Moreover, the CVD carbon coating on the Ge@CNF surface further constrains the volume change of the Ge nanoparticles and consequently contributes to the good electrode integrity structure. As a result, among the three electrode materials studied, Ge@CNF@C is the most promising anode material for high-energy lithium-ion batteries.

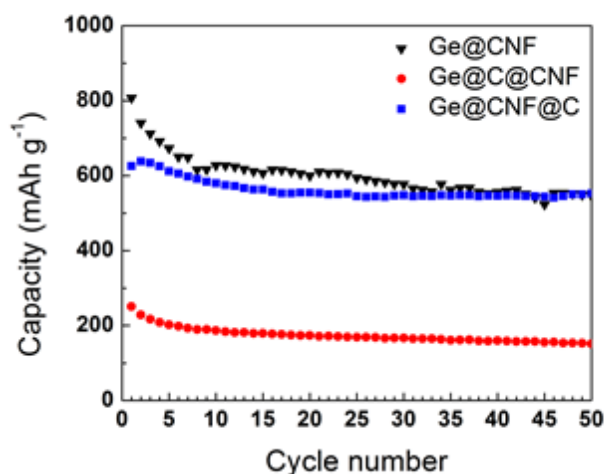


**Figure 7.8.** Cycling performances of Ge@CNF, Ge@C@CNF, and Ge@CNF@C.

#### 4. Conclusion

Ge@CNF, Ge@C@CNF, and Ge@CNF@C were prepared by using two different carbon materials, amorphous carbon coating by CVD and carbon nanofiber matrix by electrospinning technique, to mitigate the large volume change of Ge nanoparticles and preserve the integrity of the anode structure during cycling. These three electrode materials showed different characteristics in terms of structural morphology and electrochemical performance, which were demonstrated by SEM, TEM, Raman Spectroscopy, and galvanostatic charge-discharge experiments. Ge@C@CNF showed significant capacity loss due to enormous agglomeration and volume change of Ge particles and the subsequent pulverization of the anode structure. While Ge@CNF@C exhibits the highest capacity retention of 89% and largest reversible capacities of more than 550 mAh g<sup>-1</sup> because of two carbon confinement structures and Ge thorns. In this structure, the CVD carbon coating and

CNF matrix effectively constrain the volume change of the Ge nanoparticles and consequently preserve the electrode integrity. In addition, Ge thorns possessed high aspect ratio, possibly high mechanical stability and short lithium diffusion length, which facilitated the relatively high reversible capacities and excellent cycling performance.

## CHAPTER 8 CONCLUSIONS

To overcome worldwide critical energy demand and environmental pollution issues, the development of sustainable, clean, and renewable energy technologies is of significant importance. Among all energy storage devices, rechargeable batteries such as lithium-ion, nickel-metal hydride (Ni-MH), lead acid, redox flow, and sodium–sulfur (Na-S) batteries are reversible and highly durable that can repeatedly store eco-friendly electricity and deliver stored chemical energy back into electrical energy. High-performance rechargeable lithium-ion batteries, which have high energy density, long cycle life, and flexible design, appear as one of the most promising energy storage devices.

Recently, particular attention has been given to the design and synthesis of high-capacity alternative nanostructured electrode materials, especially anode materials. What deserves to be mentioned the most is carbon materials with different structures as anodic materials for lithium-ion batteries. Nanostructured carbon materials with varieties of forms, such as carbon nanotubes, carbon nanocomposites, and carbon nanofibers have been employed to construct anodes for lithium-ion batteries through a large number of synthetic and fabrication methods. Among them, the judicious combination of electrospinning and carbonization is potentially an efficient, simple and inexpensive way to fabricate carbon nanofiber anodes for lithium-ion batteries. Carbon nanofibers fabricated by electrospinning are promising materials for energy storage systems because of their large specific surface area, high aspect ratio, and unique structure.

In Chapter 4, Sn/C composite nanofibers were prepared by electrospinning and the subsequent carbonization process with 6, 10, 20 and 30% Sn(II) acetate/PAN precursors. With increase in Sn concentration, the surface morphology of the nanofibers becomes rougher due to increasing Sn aggregation in the fiber. The resultant Sn/C composite nanofibers exhibit relatively large reversible capacity and improved capacity retention. In addition, Si/C nanofiber anode prepared from 20% Sn(II) acetate/PAN nanofiber precursor provides the largest Coulombic efficiency (~99.3%) and charge-discharge capacities after nine cycles due to relatively high Sn content and moderate volume change during lithium insertion and extraction process. The results demonstrate that Sn/C anodes show relatively high reversible capacities and good capacity retention under the cooperative effects of active homogeneously-distributed Sn material and the carbon matrix, as well as the unique one-dimensional nanofiber structure with large surface area and high length/diameter ratio.

In Chapter 5, Si/C, Ge/C and Sn/C composite nanofibers with different nanoparticle contents were synthesized and investigated. Homogeneously dispersed Ge/C and Sn/C composite nanofibers show less reversible capacities due to lower theoretical capacities but better cycle performance than Si/C composite nanofibers. This is likely because Ge and Sn nanoparticles uniformly embedded in the confinement material, carbon nanofibers, inhibiting severe volume change and mechanical failure during lithiation and delithiation processes. The resultant Si/C, Ge/C and Sn/C composite anodes provide large charge/discharge capacities and good cycling performance and demonstrate that electrospinning is a promising approach to prepare

high performance inorganic nanoparticle/carbon composite fibers that have the potential to replace commercial anodes for lithium-ion batteries.

In Chapter 6,  $\text{Co}_3\text{O}_4/\text{C}$  composite nanofibers containing 10 - 30 nm and 30 - 50 nm  $\text{Co}_3\text{O}_4$  nanoparticles were fabricated through electrospinning and thermal treatment processes. Compared with  $\text{Co}_3\text{O}_4/\text{C}$  nanofibers containing 10 - 30 nm  $\text{Co}_3\text{O}_4$  nanoparticles,  $\text{Co}_3\text{O}_4/\text{C}$  anodes with 30 - 50 nm  $\text{Co}_3\text{O}_4$  nanoparticles exhibited high reversible capacity, improved Coulombic efficiencies, and good cycling stability when used as binder-free anode material for lithium-ion batteries. However, the  $\text{Co}_3\text{O}_4/\text{C}$  composite nanofibers with 10 - 30 nm  $\text{Co}_3\text{O}_4$  nanoparticles demonstrate low charge-discharge capacities due to the pulverization of the electrode and the degradation of the electrochemical activity resulting from severe nanoparticle aggregation and large surface area. The relatively good cycling performances of  $\text{Co}_3\text{O}_4/\text{C}$  composite nanofibers derived from  $\text{Co}_3\text{O}_4/\text{PAN}$  nanofibers containing 30 - 50 nm  $\text{Co}_3\text{O}_4$  nanoparticles can be attributed to their unique precursor structure with a better dispersion of  $\text{Co}_3\text{O}_4$  nanoparticles and the shorter lithium ion diffusion distance in the nanofibers.

In Chapter 7, in order to mitigate the large volume change of Ge nanoparticles and preserve the integrity of the anode structure during cycling, new  $\text{Ge}@\text{C}@\text{CNF}$ , and  $\text{Ge}@\text{CNF}@\text{C}$  structures were prepared by using two different carbon materials, amorphous carbon coating by CVD and carbon nanofiber matrix by electrospinning technique. As a comparison,  $\text{Ge}@\text{CNF}$  was also prepared. These three electrode materials showed different characteristics

in terms of structural morphology and electrochemical performance. Compared to Ge@CNF, Ge@C@CNF showed larger Ge@C clusters and consequently more significant capacity loss, while Ge@CNF@C exhibited much higher capacity retention of 89% and larger reversible capacities of 553 mAh g<sup>-1</sup> at fiftieth cycle. The results suggested that two carbon coatings in Ge@CNF@C effectively minimized the Ge agglomeration, constrained the volume change of the Ge nanoparticles and preserved the electrode integrity. It is worth to note that Ge thorns were formed in Ge@CNF@C and played an important role in the structural stability due to their high aspect ratio and possibly high mechanical stability.

## CHAPTER 9 RECOMMENDATION WORK

Results described in Chapters 4-7 show that the combination of electrospinning and carbonization leads to the production of inorganic particle-loaded carbon composite nanofibers that have large capacities, and good cycling stability, owing to their large surface area for fast reaction, and short distance for mass and charge diffusion. The focus of future work should be on the establishment of the processing-structure-performance relationships, which can guide us to design and fabricate high-performance anodes for next-generation lithium-ion batteries. The proposed future work includes but not limited to:

1. Carry out Cyclic Voltammetry (CV) measurements to identify the microstructure changes and the reactions on the electrode surfaces.

CV is one of the most versatile electroanalytical techniques for the research of electroactive species. The electrochemical properties of the electrospun composite carbon nanofibers as anodes in rechargeable lithium-ion batteries can be investigated by CV. From the information of the peaks in CV curves in anodic and cathodic processes, we can induce the reduction and oxidation reactions and the irreversible reactions of the electrodes with the electrolyte. Through a detailed exploration of these phenomena, we can eventually identify approaches to delete or decrease undesired by-reactions among the electrodes and the electrolyte, and improve the overall electrochemical performance of the batteries.

2. Prepare  $\text{Ge}_x\text{Sn}_{1-x}/\text{C}$  anodes and evaluate their electrochemical performance in lithium-ion batteries.

As mentioned in Chapter 7, Sn impurities acted as a catalyst metal and facilitated the growing of Ge thorns on the anode structure. Ge thorns possessed high aspect ratio, possibly high mechanical stability and short lithium diffusion length, which could improve the cycling performance. By simply electrospinning Sn and Ge nanoparticles into carbon nanofibers with a certain weight ratio,  $\text{Ge}_x\text{Sn}_{1-x}/\text{C}$  composite nanofibers with  $\text{Ge}_x\text{Sn}_{1-x}$  thorns or nanorods can be formed during the carbonization process. The resultant  $\text{Ge}_x\text{Sn}_{1-x}/\text{C}$  may offer excellent structural stability during Li insertion and extraction processes due to both the high mechanical stability of  $\text{Ge}_x\text{Sn}_{1-x}$  composite thorns or nanorods and the confinement of carbon nanofiber matrix.

3. Prepare  $\text{Si}@\text{SiO}_2/\text{C}$  anodes and evaluate their electrochemical performance in lithium-ion batteries.

Si is the most charming anode material for high-performance lithium-ion batteries because Si can deliver the highest known theoretical capacity of about  $4200 \text{ mAh g}^{-1}$ , which is much higher than that of graphite. However, the practical use of pure Si anodes is hindered by the severe volume expansion and shrinkage among Li uptake and release processes, leading to poor cycleability. Recent literature results show that  $\text{Si}@\text{SiO}_2$  particles can be fabricated by ball milling technique. I suggest to embed  $\text{Si}@\text{SiO}_2$  particles into carbon nanofibers. In the

resultant Si@SiO<sub>2</sub>/C anodes, the carbon nanofiber matrix can play the role of buffering or absorbing the large volume changes of anodes during charge and discharge processes, and preserve the integrities of the electrodes, thereby improving the overall electrochemical performance, especially the cycle life.

## REFERENCES

1. Ji, L. W.; Lin, Z.; Alcoutlabi, M.; Zhang, X. W. *Energy & Environmental Science* **2011**, 4, (8), 2682-2699.
2. Winter, M.; Brodd, R. J. *Chemical Reviews* **2004**, 104, (10), 4245-4269.
3. Cavaliere, S.; Subianto, S.; Savych, I.; Jones, D. J.; Roziere, J. *Energy & Environmental Science* **2011**, 4, (12), 4761-4785.
4. Cheng, F. Y.; Liang, J.; Tao, Z. L.; Chen, J. *Advanced Materials* **2011**, 23, (15), 1695-1715.
5. Cairns, E. J.; Albertus, P. *Annual Review of Chemical and Biomolecular Engineering, Vol 1* **2010**, 1, 299-320.
6. Yang, Z. G.; Liu, J.; Baskaran, S.; Imhoff, C. H.; Holladay, J. D. *Jom* **2010**, 62, (9), 14-23.
7. Tarascon, J. M.; Armand, M. *Nature* **2001**, 414, (6861), 359-367.
8. Arico, A. S.; Bruce, P.; Scrosati, B.; Tarascon, J. M.; Van Schalkwijk, W. *Nat. Mater.* **2005**, 4, (5), 366-377.
9. Alcantara, R.; Lavela, P.; Tirado, J. L.; Zhecheva, E.; Stoyaneva, R. *Journal of Solid State Electrochemistry* **1999**, 3, (3), 121-134.
10. Zhang, W. J. *Journal of Power Sources* **2011**, 196, (3), 877-885.
11. Li, Y.; Yang, X. Y.; Feng, Y.; Yuan, Z. Y.; Su, B. L. *Critical Reviews in Solid State and Materials Sciences* **2012**, 37, (1), 1-74.
12. Stura, E.; Nicolini, C. *Analytica Chimica Acta* **2006**, 568, (1-2), 57-64.
13. Su, D. S.; Schlogl, R. *Chemsuschem* **2010**, 3, (2), 136-168.

14. de las Casas, C.; Li, W. Z. *Journal of Power Sources* **2012**, 208, 74-85.
15. Aravindan, V.; Gnanaraj, J.; Madhavi, S.; Liu, H. K. *Chem-Eur J* **2011**, 17, (51), 14326-14346.
16. Winter, M.; Besenhard, J. O. *Electrochim Acta* **1999**, 45, (1-2), 31-50.
17. Huang, X. S. *Journal of Solid State Electrochemistry* **2011**, 15, (4), 649-662.
18. Ellis, B. L.; Lee, K. T.; Nazar, L. F. *Chem Mater* **2010**, 22, (3), 691-714.
19. Broussely, M.; Biensan, P.; Simon, B. *Electrochim Acta* **1999**, 45, (1-2), 3-22.
20. Manthiram, A.; Kim, J. *Chem Mater* **1998**, 10, (10), 2895-2909.
21. Luo, W. B.; Dahn, J. R. *Electrochim Acta* **2009**, 54, (20), 4655-4661.
22. Jung, Y. S.; Cavanagh, A. S.; Dillon, A. C.; Groner, M. D.; George, S. M.; Lee, S. H. *J Electrochem Soc* **2010**, 157, (1), A75-A81.
23. Kim, J.; Noh, M.; Cho, J.; Kim, H.; Kim, K. B. *J Electrochem Soc* **2005**, 152, (6), A1142-A1148.
24. Miyashiro, H.; Yamanaka, A.; Tabuchi, M.; Seki, S.; Nakayama, M.; Ohno, Y.; Kobayashi, Y.; Mita, Y.; Usami, A.; Wakihara, M. *J Electrochem Soc* **2006**, 153, (2), A348-A353.
25. Shukla, A. K.; Kumar, T. P. *Current Science* **2008**, 94, (3), 314-331.
26. Winter, M.; Besenhard, J. O.; Spahr, M. E.; Novak, P. *Advanced Materials* **1998**, 10, (10), 725-763.
27. Tarascon, J. M.; Mckinnon, W. R.; Coowar, F.; Bowmer, T. N.; Amatucci, G.; Guyomard, D. *J Electrochem Soc* **1994**, 141, (6), 1421-1431.

28. Jiao, F.; Bao, J. L.; Hill, A. H.; Bruce, P. G. *Angew Chem Int Edit* **2008**, 47, (50), 9711-9716.
29. Bittihn, R.; Herr, R.; Hoge, D. *Journal of Power Sources* **1993**, 43, (1-3), 223-231.
30. Tarascon, J. M.; Wang, E.; Shokoohi, F. K.; Mckinnon, W. R.; Colson, S. *J Electrochem Soc* **1991**, 138, (10), 2859-2864.
31. Pistoia, G.; Wang, G.; Wang, C. *Solid State Ionics* **1992**, 58, (3-4), 285-292.
32. Li, G. H.; Ikuta, H.; Uchida, T.; Wakihara, M. *J Electrochem Soc* **1996**, 143, (1), 178-182.
33. Amine, K.; Tukamoto, H.; Yasuda, H.; Fujita, Y. *J Electrochem Soc* **1996**, 143, (5), 1607-1613.
34. Kim, D. K.; Muralidharan, P.; Lee, H. W.; Ruffo, R.; Yang, Y.; Chan, C. K.; Peng, H.; Huggins, R. A.; Cui, Y. *Nano Letters* **2008**, 8, (11), 3948-3952.
35. Hosono, E.; Kudo, T.; Honma, I.; Matsuda, H.; Zhou, H. S. *Nano Letters* **2009**, 9, (3), 1045-1051.
36. Bruce, P. G.; Scrosati, B.; Tarascon, J. M. *Angew Chem Int Edit* **2008**, 47, (16), 2930-2946.
37. Wagemaker, M.; Borghols, W. J. H.; Mulder, F. M. *J Am Chem Soc* **2007**, 129, (14), 4323-4327.
38. Okubo, M.; Hosono, E.; Kim, J.; Enomoto, M.; Kojima, N.; Kudo, T.; Zhou, H. S.; Honma, I. *J Am Chem Soc* **2007**, 129, (23), 7444-7452.
39. Okubo, M.; Mizuno, Y.; Yamada, H.; Kim, J.; Hosono, E.; Zhou, H. S.; Kudo, T.; Honma, I. *Acs Nano* **2010**, 4, (2), 741-752.

40. Padhi, A. K.; Nanjundaswamy, K. S.; Goodenough, J. B. *J Electrochem Soc* **1997**, 144, (4), 1188-1194.
41. Li, J. Y.; Yao, W. L.; Martin, S.; Vaknin, D. *Solid State Ionics* **2008**, 179, (35-36), 2016-2019.
42. Arora, P.; White, R. E.; Doyle, M. *J Electrochem Soc* **1998**, 145, (10), 3647-3667.
43. Kang, B.; Ceder, G. *Nature* **2009**, 458, (7235), 190-193.
44. Delmas, C.; Maccario, M.; Croguennec, L.; Le Cras, F.; Weill, F. *Nat. Mater.* **2008**, 7, (8), 665-671.
45. Wang, Y. G.; Wang, Y. R.; Hosono, E. J.; Wang, K. X.; Zhou, H. S. *Angew Chem Int Edit* **2008**, 47, (39), 7461-7465.
46. Wu, X. L.; Jiang, L. Y.; Cao, F. F.; Guo, Y. G.; Wan, L. J. *Advanced Materials* **2009**, 21, (25-26), 2710-+.
47. Gwon, H.; Seo, D. H.; Kim, S. W.; Kim, J.; Kang, K. *Adv Funct Mater* **2009**, 19, (20), 3285-3292.
48. Bramnik, N. N.; Nikolowski, K.; Baetz, C.; Bramnik, K. G.; Ehrenberg, H. *Chem Mater* **2007**, 19, (4), 908-915.
49. Martha, S. K.; Grinblat, J.; Haik, O.; Zinigrad, E.; Drezen, T.; Miners, J. H.; Exnar, I.; Kay, A.; Markovsky, B.; Aurbach, D. *Angew Chem Int Edit* **2009**, 48, (45), 8559-8563.
50. Ellis, B. L.; Makahnouk, W. R. M.; Makimura, Y.; Toghiani, K.; Nazar, L. F. *Nat. Mater.* **2007**, 6, (10), 749-753.
51. Reham, N.; Chotard, J. N.; Dupont, L.; Delacourt, C.; Walker, W.; Armand, M.; Tarascon, J. M. *Nat. Mater.* **2010**, 9, (1), 68-74.

52. Arroyo-DeDompablo, M. E.; Dominko, R.; Gallardo-Amores, J. M.; Dupont, L.; Mali, G.; Ehrenberg, H.; Jamnik, J.; Moran, E. *Chem Mater* **2008**, 20, (17), 5574-5584.
53. Nishimura, S. I.; Hayase, S.; Kanno, R.; Yashima, M.; Nakayama, N.; Yamada, A. *J Am Chem Soc* **2008**, 130, (40), 13212-13213.
54. Ellis, B. L.; Makahnouk, W. R. M.; Rowan-Weetaluktuk, W. N.; Ryan, D. H.; Nazar, L. F. *Chem Mater* **2010**, 22, (3), 1059-1070.
55. Simonet, J.; Raultberthelot, J. *Progress in Solid State Chemistry* **1991**, 21, (1), 1-48.
56. Cheng, F. Y.; Tang, W.; Li, C. S.; Chen, J.; Liu, H. K.; Shen, P. W.; Dou, S. X. *Chem-Eur J* **2006**, 12, (11), 3082-3088.
57. Han, X. Y.; Chang, C. X.; Yuan, L. J.; Sun, T. L.; Sun, J. T. *Advanced Materials* **2007**, 19, (12), 1616-+.
58. Noked, M.; Soffer, A.; Aurbach, D. *Journal of Solid State Electrochemistry* **2011**, 15, (7-8), 1563-1578.
59. Huggins, R. A. *Solid State Ionics* **1998**, 113, 57-67.
60. Park, C. M.; Sohn, H. J. *Advanced Materials* **2010**, 22, (1), 47-+.
61. Kamali, A. R.; Fray, D. J. *Reviews on Advanced Materials Science* **2011**, 27, (1), 14-24.
62. Todd, A. D. W.; Ferguson, P. P.; Fleischauer, M. D.; Dahn, J. R. *International Journal of Energy Research* **2010**, 34, (6), 535-555.
63. Teki, R.; Datta, M. K.; Krishnan, R.; Parker, T. C.; Lu, T. M.; Kumta, P. N.; Koratkar, N. *Small* **2009**, 5, (20), 2236-2242.

64. Li, H.; Wang, Z. X.; Chen, L. Q.; Huang, X. J. *Advanced Materials* **2009**, 21, (45), 4593-4607.
65. Kasavajjula, U.; Wang, C. S.; Appleby, A. J. *Journal of Power Sources* **2007**, 163, (2), 1003-1039.
66. Kim, M. G.; Cho, J. *Adv Funct Mater* **2009**, 19, (10), 1497-1514.
67. Kaskhedikar, N. A.; Maier, J. *Advanced Materials* **2009**, 21, (25-26), 2664-2680.
68. Liu, C.; Li, F.; Ma, L. P.; Cheng, H. M. *Advanced Materials* **2010**, 22, (8), E28-+.
69. Holzapfel, M.; Buqa, H.; Scheifele, W.; Novak, P.; Petrat, F. M. *Chemical Communications* **2005**, (12), 1566-1568.
70. Park, C. M.; Kim, J. H.; Kim, H.; Sohn, H. J. *Chemical Society Reviews* **2010**, 39, (8), 3115-3141.
71. Li, H.; Huang, X. J.; Chen, L. Q.; Zhou, G. W.; Zhang, Z.; Yu, D. P.; Mo, Y. J.; Pei, N. *Solid State Ionics* **2000**, 135, (1-4), 181-191.
72. Ji, L. W.; Jung, K. H.; Medford, A. J.; Zhang, X. W. *Journal of Materials Chemistry* **2009**, 19, (28), 4992-4997.
73. Ji, L. W.; Zhang, X. W. *Electrochem Commun* **2009**, 11, (6), 1146-1149.
74. Ji, L. W.; Zhang, X. W. *Energy & Environmental Science* **2010**, 3, (1), 124-129.
75. Wilson, A. M.; Dahn, J. R. *J Electrochem Soc* **1995**, 142, (2), 326-332.
76. Guo, Z. P.; Jia, D. Z.; Yuan, L.; Liu, H. K. *Journal of Power Sources* **2006**, 159, (1), 332-335.
77. Ng, S. H.; Wang, J. Z.; Wexler, D.; Konstantinov, K.; Guo, Z. P.; Liu, H. K. *Angew Chem Int Edit* **2006**, 45, (41), 6896-6899.

78. Zhou, H. S.; Zhu, S. M.; Hibino, M.; Honma, I.; Ichihara, M. *Advanced Materials* **2003**, 15, (24), 2107-+.
79. Jiao, F.; Bruce, P. G. *Advanced Materials* **2007**, 19, (5), 657-+.
80. Mancini, M.; Kubiak, P.; Wohlfahrt-Mehrens, M.; Marassi, R. *J Electrochem Soc* **2010**, 157, (2), A164-A170.
81. Szczech, J. R.; Jin, S. *Energy & Environmental Science* **2011**, 4, (1), 56-72.
82. Kim, H.; Han, B.; Choo, J.; Cho, J. *Angew Chem Int Edit* **2008**, 47, (52), 10151-10154.
83. Y. S. Hu, P. A., B. M. Smarsly, J. Maier. *ChemSusChem* **2009**.
84. Kim, H.; Cho, J. *Nano Letters* **2008**, 8, (11), 3688-3691.
85. Liu, X.; Zheng, M. C.; Xie, K. *Journal of Power Sources* **2011**, 196, (24), 10667-10672.
86. Hu, Y. S.; Demir-Cakan, R.; Titirici, M. M.; Muller, J. O.; Schlogl, R.; Antonietti, M.; Maier, J. *Angew Chem Int Edit* **2008**, 47, (9), 1645-1649.
87. Park, C. M.; Sohn, H. J. *Chem Mater* **2008**, 20, (9), 3169-3173.
88. Shin, H. C.; Liu, M. L. *Adv Funct Mater* **2005**, 15, (4), 582-586.
89. Ehinon, K. K. D.; Naille, S.; Dedryvere, R.; Lippens, P. E.; Jumas, J. C.; Gonbeau, D. *Chem Mater* **2008**, 20, (16), 5388-5398.
90. Hassoun, J.; Panero, S.; Simon, P.; Taberna, P. L.; Scrosati, B. *Advanced Materials* **2007**, 19, (12), 1632-+.
91. Mosby, J. M.; Prieto, A. L. *J Am Chem Soc* **2008**, 130, (32), 10656-10661.
92. Wolfenstine, J. *Journal of Power Sources* **2003**, 124, (1), 241-245.

93. Li, T.; Cao, Y. L.; Ai, X. P.; Yang, H. X. *Journal of Power Sources* **2008**, 184, (2), 473-476.
94. Lee, K. M.; Lee, Y. S.; Kim, Y. W.; Sun, Y. K.; Lee, S. M. *Journal of Alloys and Compounds* **2009**, 472, (1-2), 461-465.
95. Kim, H.; Choi, J.; Sohn, H. J.; Kang, T. *J Electrochem Soc* **1999**, 146, (12), 4401-4405.
96. Graetz, J.; Ahn, C. C.; Yazami, R.; Fultz, B. *J Electrochem Soc* **2004**, 151, (5), A698-A702.
97. Chan, C. K.; Zhang, X. F.; Cui, Y. *Nano Letters* **2008**, 8, (1), 307-309.
98. Yoon, S.; Park, C. M.; Sohn, H. J. *Electrochem Solid St* **2008**, 11, (4), A42-A45.
99. Lee, H.; Kim, H.; Doo, S. G.; Cho, J. *J Electrochem Soc* **2007**, 154, (4), A343-A346.
100. Cui, G. L.; Gu, L.; Zhi, L. J.; Kaskhedikar, N.; van Aken, P. A.; Mullen, K.; Maier, J. *Advanced Materials* **2008**, 20, (16), 3079-3083.
101. Seo, M. H.; Park, M.; Lee, K. T.; Kim, K.; Kim, J.; Cho, J. *Energy & Environmental Science* **2011**, 4, (2), 425-428.
102. Tan, L. P.; Lu, Z. Y.; Tan, H. T.; Zhu, J. X.; Rui, X. H.; Yan, Q. Y.; Hng, H. H. *Journal of Power Sources* **2012**, 206, 253-258.
103. Chae, O. B.; Park, S.; Ku, J. H.; Ryu, J. H.; Oh, S. M. *Electrochim Acta* **2010**, 55, (8), 2894-2900.
104. Hwa, Y.; Park, C. M.; Yoon, S.; Sohn, H. J. *Electrochim Acta* **2010**, 55, (9), 3324-3329.
105. Esaka, T.; Iida, Y. *Electrochemistry* **78**, (8), 666-670.

106. Iida, T.; Hirono, T.; Shibamura, N.; Sakaguchi, H. *Electrochemistry* **2008**, 76, (9), 644-648.
107. Wang, J. Z.; Du, N.; Zhang, H.; Yu, J. X.; Yang, D. R. *Journal of Power Sources* **2012**, 208, 434-439.
108. Kim, M. G.; Cho, J. *J Electrochem Soc* **2009**, 156, (4), A277-A282.
109. Ui, K.; Kikuchi, S.; Kadoma, Y.; Kumagai, N.; Ito, S. *Journal of Power Sources* **2009**, 189, (1), 224-229.
110. Beaulieu, L. Y.; Dahn, J. R. *J Electrochem Soc* **2000**, 147, (9), 3237-3241.
111. Yang, J.; Winter, M.; Besenhard, J. O. *Solid State Ionics* **1996**, 90, (1-4), 281-287.
112. Courtney, I. A.; Dahn, J. R. *J Electrochem Soc* **1997**, 144, (9), 2943-2948.
113. Mao, O.; Dunlap, R. A.; Dahn, J. R. *J Electrochem Soc* **1999**, 146, (2), 405-413.
114. Liu, Y.; Xie, J. Y.; Takeda, Y.; Yang, J. *J Appl Electrochem* **2002**, 32, (6), 687-692.
115. Lin, K. Z.; Wang, X. L.; Xu, Y. H.; Luo, G. H. *J Wuhan Univ Technol* **2006**, 21, (4), 60-63.
116. Derrien, G.; Hassoun, J.; Panero, S.; Scrosati, B. *Advanced Materials* **2007**, 19, (17), 2336-+.
117. Morishita, T.; Hirabayashi, T.; Okuni, T.; Ota, N.; Inagaki, M. *Journal of Power Sources* **2006**, 160, (1), 638-644.
118. Li, R. Y.; Sun, X. C.; Zhou, X. R.; Cai, M.; Sun, X. L. *J Phys Chem C* **2007**, 111, (26), 9130-9135.
119. Zhang, W. M.; Hu, J. S.; Guo, Y. G.; Zheng, S. F.; Zhong, L. S.; Song, W. G.; Wan, L. J. *Advanced Materials* **2008**, 20, (6), 1160-+.

120. Lee, K. T.; Jung, Y. S.; Oh, S. M. *J Am Chem Soc* **2003**, 125, (19), 5652-5653.
121. Nobili, F.; Mancini, M.; Dsoke, S.; Tossici, R.; Marassi, R. *Journal of Power Sources* **2010**, 195, (20), 7090-7097.
122. Yu, Y. H.; Yang, Q.; Teng, D. H.; Yang, X. P.; Ryu, S. *Electrochem Commun* **2010**, 12, (9), 1187-1190.
123. Deng, D.; Lee, J. Y. *Angew Chem Int Edit* **2009**, 48, (9), 1660-1663.
124. Lee, S. H.; Mathews, M.; Toghiani, H.; Wipf, D. O.; Pittman, C. U. *Chem Mater* **2009**, 21, (11), 2306-2314.
125. Hassoun, J.; Derrien, G.; Panero, S.; Scrosati, B. *Advanced Materials* **2008**, 20, (16), 3169-3175.
126. Kim, I. S.; Blomgren, G. E.; Kumta, P. N. *Electrochem Solid St* **2004**, 7, (3), A44-A48.
127. Grigoriant, I.; Soffer, A.; Salitra, G.; Aurbach, D. *Journal of Power Sources* **2005**, 146, (1-2), 185-189.
128. Balan, L.; Schneider, R.; Ghanbaja, J.; Willmann, P.; Billaud, D. *Electrochim Acta* **2006**, 51, (17), 3385-3390.
129. Veeraraghavan, B.; Durairajan, A.; Haran, B.; Popov, B.; Guidotti, R. *J Electrochem Soc* **2002**, 149, (6), A675-A681.
130. Egashira, M.; Takatsuji, H.; Okada, S.; Yamaki, J. *Journal of Power Sources* **2002**, 107, (1), 56-60.
131. Park, J. W.; Eom, J. Y.; Kwon, H. S. *International Journal of Electrochemical Science* **2011**, 6, (8), 3093-3104.

132. Yan, H. W.; Sokolov, S.; Lytle, J. C.; Stein, A.; Zhang, F.; Smyrl, W. H. *J Electrochem Soc* **2003**, 150, (8), A1102-A1107.
133. Yu, Y.; Gu, L.; Zhu, C. B.; van Aken, P. A.; Maier, J. *J Am Chem Soc* **2009**, 131, (44), 15984-+.
134. Grigoriants, I.; Sominski, L.; Li, H. L.; Ifargan, I.; Aurbach, D.; Gedanken, A. *Chemical Communications* **2005**, (7), 921-923.
135. Yu, Y.; Gu, L.; Wang, C. L.; Dhanabalan, A.; van Aken, P. A.; Maier, J. *Angew Chem Int Edit* **2009**, 48, (35), 6485-6489.
136. Tamura, N.; Fujimoto, A.; Kamino, M.; Fujitani, S. *Electrochim Acta* **2004**, 49, (12), 1949-1956.
137. Zhang, J. J.; Xia, Y. Y. *J Electrochem Soc* **2006**, 153, (8), A1466-A1471.
138. Mukaibo, H.; Sumi, T.; Yokoshima, T.; Momma, T.; Osaka, T. *Electrochem Solid St* **2003**, 6, (10), A218-A220.
139. Ke, F. S.; Huang, L.; Jiang, H. H.; Wei, H. B.; Yang, F. Z.; Sun, S. G. *Electrochem Commun* **2007**, 9, (2), 228-232.
140. Yang, J.; Takeda, Y.; Imanishi, N.; Yamamoto, O. *J Electrochem Soc* **1999**, 146, (11), 4009-4013.
141. Tamura, N.; Ohshita, R.; Fujimoto, M.; Fujitani, S.; Kamino, M.; Yonezu, I. *Journal of Power Sources* **2002**, 107, (1), 48-55.
142. Beattie, S. D.; Dahn, J. R. *J Electrochem Soc* **2003**, 150, (7), A894-A898.
143. Pu, W. H.; He, X. M.; Ren, J. G.; Wan, C. R.; Jiang, C. Y. *Electrochim Acta* **2005**, 50, (20), 4140-4145.

144. Ke, F. S.; Huang, L.; Cai, J. S.; Sun, S. G. *Electrochim Acta* **2007**, *52*, (24), 6741-6747.
145. Cabana, J.; Monconduit, L.; Larcher, D.; Palacin, M. R. *Advanced Materials* **2010**, *22*, (35), E170-E192.
146. Poizot, P.; Laruelle, S.; Grugeon, S.; Dupont, L.; Tarascon, J. M. *Nature* **2000**, *407*, (6803), 496-499.
147. Larcher, D.; Sudant, G.; Leriche, J. B.; Chabre, Y.; Tarascon, J. M. *J Electrochem Soc* **2002**, *149*, (3), A234-A241.
148. Adelhelm, P.; Hu, Y. S.; Antonietti, M.; Maier, J.; Smarsly, B. M. *Journal of Materials Chemistry* **2009**, *19*, (11), 1616-1620.
149. Flandrois, S.; Simon, B. *Carbon* **1999**, *37*, (2), 165-180.
150. Shaju, K. M.; Jiao, F.; Debart, A.; Bruce, P. G. *Phys. Chem. Chem. Phys.* **2007**, *9*, (15), 1837-1842.
151. Zhi, L. J.; Hu, Y. S.; El Hamaoui, B.; Wang, X.; Lieberwirth, I.; Kolb, U.; Maier, J.; Mullen, K. *Advanced Materials* **2008**, *20*, (9), 1727-+.
152. Needham, S. A.; Wang, G. X.; Konstantinov, K.; Tournayre, Y.; Lao, Z.; Liu, H. K. *Electrochem Solid St* **2006**, *9*, (7), A315-A319.
153. Liu, Y.; Mi, C. H.; Su, L. H.; Zhang, X. G. *Electrochim Acta* **2008**, *53*, (5), 2507-2513.
154. Chen, J. S.; Zhu, T.; Hu, Q. H.; Gao, J. J.; Su, F. B.; Qiao, S. Z.; Lou, X. W. *Acs Applied Materials & Interfaces* **2**, (12), 3628-3635.
155. Li, Y. G.; Tan, B.; Wu, Y. Y. *Nano Letters* **2008**, *8*, (1), 265-270.

156. X. W. Lou, D. D., J. Y. Lee, J. Feng, L.A. Archer. *Advanced Materials* **2008**, 20, (2), 258-262.
157. Yang, R. Z.; Wang, Z. X.; Liu, J. Y.; Chen, L. Q. *Electrochem Solid St* **2004**, 7, (12), A496-A499.
158. Kerr, R. L.; Miller, S. A.; Shoemaker, R. K.; Elliott, B. J.; Gin, D. L. *J Am Chem Soc* **2009**, 131, (44), 15972-+.
159. Goodenough, J. B.; Kim, Y. *Journal of Power Sources* 196, (16), 6688-6694.
160. Lewandowski, A.; Swiderska-Mocek, A. *Journal of Power Sources* **2009**, 194, (2), 601-609.
161. Seki, S.; Ohno, Y.; Kobayashi, Y.; Miyashiro, H.; Usami, A.; Mita, Y.; Tokuda, H.; Watanabe, M.; Hayamizu, K.; Tsuzuki, S.; Hattori, M.; Terada, N. *J Electrochem Soc* **2007**, 154, (3), A173-A177.
162. Christie, A. M.; Lilley, S. J.; Staunton, E.; Andreev, Y. G.; Bruce, P. G. *Nature* **2005**, 433, (7021), 50-53.
163. Choi, S. W.; Kim, J. R.; Ahn, Y. R.; Jo, S. M.; Cairns, E. J. *Chem Mater* **2007**, 19, (1), 104-115.
164. Hassoun, J.; Panero, S.; Reale, P.; Scrosati, B. *Advanced Materials* **2009**, 21, (47), 4807-+.
165. Dong, Z. X.; Kennedy, S. J.; Wu, Y. Q. *Journal of Power Sources* **2011**, 196, (11), 4886-4904.
166. Doshi, J.; Reneker, D. H. *Journal of Electrostatics* **1995**, 35, (2-3), 151-160.
167. Reneker, D. H.; Chun, I. *Nanotechnology* **1996**, 7, (3), 216-223.

168. Huang, Z. M.; Zhang, Y. Z.; Kotaki, M.; Ramakrishna, S. *Composites Science and Technology* **2003**, 63, (15), 2223-2253.
169. Li, D.; Xia, Y. N. *Advanced Materials* **2004**, 16, (14), 1151-1170.
170. Greiner, A.; Wendorff, J. H. *Angew Chem Int Edit* **2007**, 46, (30), 5670-5703.
171. Lu, X. F.; Wang, C.; Wei, Y. *Small* **2009**, 5, (21), 2349-2370.
172. Yarin, A. L. *Polymers for Advanced Technologies* **2011**, 22, (3), 310-317.
173. Zhang, H.; Zhao, C. G.; Zhao, Y. H.; Tang, G. W.; Yuan, X. Y. *Science China-Chemistry* **2010**, 53, (6), 1246-1254.
174. Yarin, A. L.; Koombhongse, S.; Reneker, D. H. *Journal of Applied Physics* **2001**, 89, (5), 3018-3026.
175. Teo, W. E.; Inai, R.; Ramakrishna, S. *Science and Technology of Advanced Materials* **2011**, 12, (1).
176. Bhardwaj, N.; Kundu, S. C. *Biotechnology Advances* **2010**, 28, (3), 325-347.
177. Feng, C.; Khulbe, K. C.; Matsuura, T. *Journal of Applied Polymer Science* **2010**, 115, (2), 756-776.
178. Liu, C. K.; Lai, K.; Liu, W.; Yao, M.; Sun, R. J. *Polymer International* **2009**, 58, (12), 1341-1349.
179. Bellan, L. M.; Craighead, H. G. *Journal of Manufacturing Science and Engineering-Transactions of the Asme* **2009**, 131, (3).
180. Fang, J.; Niu, H. T.; Lin, T.; Wang, X. G. *Chinese Science Bulletin* **2008**, 53, (15), 2265-2286.
181. Fong, H.; Chun, I.; Reneker, D. H. *Polymer* **1999**, 40, (16), 4585-4592.

182. Huang, L.; McMillan, R. A.; Apkarian, R. P.; Pourdeyhimi, B.; Conticello, V. P.; Chaikof, E. L. *Macromolecules* **2000**, 33, (8), 2989-2997.
183. Fong, H.; Liu, W. D.; Wang, C. S.; Vaia, R. A. *Polymer* **2002**, 43, (3), 775-780.
184. Casper, C. L.; Stephens, J. S.; Tassi, N. G.; Chase, D. B.; Rabolt, J. F. *Macromolecules* **2004**, 37, (2), 573-578.
185. McCann, J. T.; Li, D.; Xia, Y. N. *Journal of Materials Chemistry* **2005**, 15, (7), 735-738.
186. Li, D.; Wang, Y. L.; Xia, Y. N. *Nano Letters* **2003**, 3, (8), 1167-1171.
187. Thavasi, V.; Singh, G.; Ramakrishna, S. *Energy & Environmental Science* **2008**, 1, (2), 205-221.
188. Li, W. J.; Laurencin, C. T.; Catterson, E. J.; Tuan, R. S.; Ko, F. K. *Journal of Biomedical Materials Research* **2002**, 60, (4), 613-621.
189. Matthews, J. A.; Wnek, G. E.; Simpson, D. G.; Bowlin, G. L. *Biomacromolecules* **2002**, 3, (2), 232-238.
190. Yoshimoto, H.; Shin, Y. M.; Terai, H.; Vacanti, J. P. *Biomaterials* **2003**, 24, (12), 2077-2082.
191. Kenawy, E. R.; Bowlin, G. L.; Mansfield, K.; Layman, J.; Simpson, D. G.; Sanders, E. H.; Wnek, G. E. *Journal of Controlled Release* **2002**, 81, (1-2), 57-64.
192. Katti, D. S.; Robinson, K. W.; Ko, F. K.; Laurencin, C. T. *Journal of Biomedical Materials Research Part B-Applied Biomaterials* **2004**, 70B, (2), 286-296.
193. Kim, K.; Luu, Y. K.; Chang, C.; Fang, D. F.; Hsiao, B. S.; Chu, B.; Hadjiargyrou, M. *Journal of Controlled Release* **2004**, 98, (1), 47-56.

194. Khil, M. S.; Cha, D. I.; Kim, H. Y.; Kim, I. S.; Bhattarai, N. *Journal of Biomedical Materials Research Part B-Applied Biomaterials* **2003**, 67B, (2), 675-679.
195. Rho, K. S.; Jeong, L.; Lee, G.; Seo, B. M.; Park, Y. J.; Hong, S. D.; Roh, S.; Cho, J. J.; Park, W. H.; Min, B. M. *Biomaterials* **2006**, 27, (8), 1452-1461.
196. Kim, I. D.; Rothschild, A.; Lee, B. H.; Kim, D. Y.; Jo, S. M.; Tuller, H. L. *Nano Letters* **2006**, 6, (9), 2009-2013.
197. Yoon, J.; Chae, S. K.; Kim, J. M. *J Am Chem Soc* **2007**, 129, (11), 3038-+.
198. Li, Z. Y.; Zhang, H. N.; Zheng, W.; Wang, W.; Huang, H. M.; Wang, C.; MacDiarmid, A. G.; Wei, Y. *J Am Chem Soc* **2008**, 130, (15), 5036-+.
199. Gryta, M. *Journal of Membrane Science* **2005**, 265, (1-2), 153-159.
200. Gopal, R.; Kaur, S.; Ma, Z. W.; Chan, C.; Ramakrishna, S.; Matsuura, T. *Journal of Membrane Science* **2006**, 281, (1-2), 581-586.
201. Inagaki, M.; Yang, Y.; Kang, F. Y. *Advanced Materials* 24, (19), 2547-2566.
202. Su, X.; Wu, Q. L.; Zhan, X.; Wu, J.; Wei, S. Y.; Guo, Z. H. *Journal of Materials Science* **2012**, 47, (6), 2519-2534.
203. Liang, S. Z.; Zhu, X. F.; Lian, P. C.; Yang, W. S.; Wang, H. H. *J Solid State Chem* **2011**, 184, (6), 1400-1404.
204. Noh, M.; Kwon, Y.; Lee, H.; Cho, J.; Kim, Y.; Kim, M. G. *Chem Mater* **2005**, 17, (8), 1926-1929.
205. Wang, Z.; Tian, W. H.; Liu, X. H.; Yang, R.; Li, X. G. *J Solid State Chem* **2007**, 180, (12), 3360-3365.

206. Liu, S.; Li, Q.; Chen, Y. X.; Zhang, F. J. *Journal of Alloys and Compounds* **2009**, 478, (1-2), 694-698.
207. Xue, L. G.; Fu, Z. H.; Yao, Y.; Huang, T.; Yu, A. S. *Electrochim Acta* **2010**, 55, (24), 7310-7314.
208. Wang, G. X.; Yao, J.; Liu, H. K.; Dou, S. X.; Ahn, J. H. *Electrochim Acta* **2004**, 50, (2-3), 517-522.
209. Yang, S. B.; Song, H. H.; Chen, X. H. *Journal of Power Sources* **2007**, 173, (1), 487-494.
210. Wang, Y.; Wu, M.; Jiao, Z.; Lee, J. Y. *Chem Mater* **2009**, 21, (14), 3210-3215.
211. Yang, S. B.; Song, H. H.; Yi, H. X.; Liu, W. X.; Zhang, H. J.; Chen, X. H. *Electrochim Acta* **2009**, 55, (2), 521-527.
212. Paek, S. M.; Yoo, E.; Honma, I. *Nano Letters* **2009**, 9, (1), 72-75.
213. Zou, L.; Gan, L.; Kang, F. Y.; Wang, M. X.; Shen, W. C.; Huang, Z. H. *Journal of Power Sources* **2010**, 195, (4), 1216-1220.
214. Bonino, C. A.; Ji, L. W.; Lin, Z.; Toprakci, O.; Zhang, X. W.; Khan, S. A. *Acs Applied Materials & Interfaces* **2011**, 3, (7), 2534-2542.
215. Ji, L. W.; Lin, Z.; Alcoutlabi, M.; Toprakci, O.; Yao, Y. F.; Xu, G. J.; Li, S. L.; Zhang, X. W. *Rsc Advances* **2012**, 2, (1), 192-198.
216. Huggins, R. A. *Journal of Power Sources* **1999**, 81, 13-19.
217. Collins, G.; Federici, J.; Imura, Y.; Catalani, L. H. *Journal of Applied Physics* **2012**, 111, (4).
218. Wang, T.; Kumar, S. *Journal of Applied Polymer Science* **2006**, 102, (2), 1023-1029.

219. Ji, L. W.; Zhang, X. W. *Nanotechnology* **2009**, 20, (15).
220. Ji, L. W.; Zhang, X. W. *Electrochem Commun* **2009**, 11, (3), 684-687.
221. Zou, G. F.; Zhang, D. W.; Dong, C.; Li, H.; Xiong, K.; Fei, L. F.; Qian, Y. T. *Carbon* **2006**, 44, (5), 828-832.
222. Kim, C.; Yang, K. S.; Kojima, M.; Yoshida, K.; Kim, Y. J.; Kim, Y. A.; Endo, M. *Adv Funct Mater* **2006**, 16, (18), 2393-2397.
223. Ji, L. W.; Lin, Z.; Medford, A. J.; Zhang, X. W. *Chem-Eur J* **2009**, 15, (41), 10718-10722.
224. Wang, W.; Datta, M. K.; Kumta, P. N. *Journal of Materials Chemistry* **2007**, 17, (30), 3229-3237.
225. Wang, Q.; Liu, L. J.; Chen, L. Q.; Huang, X. J. *J Electrochem Soc* **2004**, 151, (9), A1333-A1337.
226. Maurin, G.; Bousquet, C.; Henn, F.; Bernier, P.; Almairac, R.; Simon, B. *Chemical Physics Letters* **1999**, 312, (1), 14-18.
227. Lin, Z.; Ji, L. W.; Woodroof, M. D.; Zhang, X. W. *Journal of Power Sources* **2010**, 195, (15), 5025-5031.
228. Ji, L. W.; Zhang, X. W. *Carbon* **2009**, 47, (14), 3219-3226.
229. Wen, W.; Wu, J. M.; Tu, J. P. *Journal of Alloys and Compounds* **2012**, 513, 592-596.
230. Yao, W. L.; Wang, J. L.; Yang, J.; Du, G. D. *Journal of Power Sources* **2008**, 176, (1), 369-372.
231. Zhang, P.; Guo, Z. P.; Huang, Y. D.; Jia, D. Z.; Liu, H. K. *Journal of Power Sources* **2011**, 196, (16), 6987-6991.

232. Yao, W. L.; Yang, J.; Wang, J. L.; Tao, L. A. *Electrochim Acta* **2008**, 53, (24), 7326-7330.
233. Yao, W. L.; Chen, J. Q.; Li, A. Y.; Chen, X. B., Novel Co(3)O(4)/carbon nanofiber composite electrode with high Li-storage capacity for lithium ion batteries. In *New and Advanced Materials, Pts 1 and 2*, Zhou, H. Y.; Gu, T. L.; Yang, D. G.; Jiang, Z. Y.; Zeng, J. M., Eds. Trans Tech Publications Ltd: Stafa-Zurich, Vol. 197-198, pp 1113-1116.
234. Mao, J.; Dai, K. H.; Zhai, Y. C. *Electrochim Acta* **2012**, 63, 381-390.
235. Ishizaki, C.; Raharjo, P.; Sato, K.; Ishizaki, K. *J. Ceram. Soc. Jpn.* **2001**, 109, (1), 16-22.
236. Zarzycki, J.; Prassas, M.; Phalippou, J. *Journal of Materials Science* **1982**, 17, (11), 3371-3379.
237. Rahman, M. M.; Wang, J. Z.; Deng, X. L.; Li, Y.; Liu, H. K. *Electrochim Acta* **2009**, 55, (2), 504-510.
238. Yuan, Z. Y.; Huang, F.; Feng, C. Q.; Sun, J. T.; Zhou, Y. H. *Materials Chemistry and Physics* **2003**, 79, (1), 1-4.
239. Lei, X. F.; Ma, J. X.; Sun, Y. Y. *International Journal of Electrochemical Science* **2011**, 6, (3), 573-580.
240. Fu, L. J.; Liu, H.; Li, C.; Wu, Y. P.; Rahm, E.; Holze, R.; Wu, H. Q. *Solid State Sciences* **2006**, 8, (2), 113-128.
241. Guo, H. J.; Sun, Q. M.; Li, X. H.; Wang, Z. X.; Peng, W. J. *Transactions of Nonferrous Metals Society of China* **2009**, 19, (2), 372-376.
242. Zhang, W. J. *Journal of Power Sources* **2011**, 196, (1), 13-24.

243. Li, H.; Huang, X. J.; Chen, L. Q.; Wu, Z. G.; Liang, Y. *Electrochem Solid St* **1999**, 2, (11), 547-549.
244. Cui, G. L.; Gu, L.; Kaskhedikar, N.; van Aken, P. A.; Maier, J. *Electrochim Acta* **2010**, 55, (3), 985-988.
245. Woo, S. H.; Choi, S. J.; Park, J. H.; Yoon, W. S.; Hwang, S. W.; Whang, D. *J Electrochem Soc* **2013**, 160, (1), A112-A116.
246. Wu, J.; Coffey, J. L.; Wang, Y. J.; Schulze, R. *J Phys Chem C* **2009**, 113, (1), 12-16.
247. Li, X. D.; Meng, G. W.; Xu, Q. L.; Kong, M. G.; Zhu, X. G.; Chu, Z. Q.; Li, A. P. *Nano Letters* **2011**, 11, (4), 1704-1709.
248. Laforge, B.; Levan-Jodin, L.; Salot, R.; Billard, A. *J Electrochem Soc* **2008**, 155, (2), A181-A188.
249. Chockla, A. M.; Panthani, M. G.; Holmberg, V. C.; Hessel, C. M.; Reid, D. K.; Bogart, T. D.; Harris, J. T.; Mullins, C. B.; Korgel, B. A. *J Phys Chem C* **2012**, 116, (22), 11917-11923.